Fusion-Based Impairment Modelling for an Intelligent Radar Sensor Architecture

Darren Lee James Radford, B.Sc (Hons)

Communication Research Centre
Cardiff University

Thesis submitted for the degree of Doctor of Philosophy

16th March 2009

ProQuest LLC
789 East Eisenhower Parkway
P.O. Box 1346
Ann Arbor, MI 48106-1346

DECLARATION

This work has not previously been accepted in substance for any degree and is not concurrently submitted in candidature for any degree.

Signed ..... (candidate) Date 15/6/09
.....

STATEMENT 1

This thesis is being submitted in partial fulfillment of the requirements for the degree of .....(insert MCh, MD, MPhil, PhD etc, as appropriate)

Signed ..... (candidate) 15/6/09 Date
.....

STATEMENT 2

This thesis is the result of my own independent work/investigation, except where otherwise stated.
Other sources are acknowledged by explicit references.

Signed ..... (candidate) 15/6/09 Date
.....

STATEMENT 3

I hereby give consent for my thesis, if accepted, to be available for photocopying and for inter-library loan, and for the title and summary to be made available to outside organisations.

Signed ..... (candidate) 15/6/09 Date
.....

STATEMENT 4: PREVIOUSLY APPROVED BAR ON ACCESS

I hereby give consent for my thesis, if accepted, to be available for photocopying and for inter-library loans **after expiry of a bar on access previously approved by the Graduate Development Committee.**

Signed ..... (candidate) 15/6/09 Date
.....

Abstract

An intelligent radar sensor concept has been developed using a modelling approach for prediction of sensor performance, based on application of sensor and environment models. Land clutter significantly impacts on the operation of radar sensors operating at low-grazing angles. The clutter modelling technique developed in this thesis for the prediction of land clutter forms the clutter model for the intelligent radar sensor. Fusion of remote sensing data is integral to the clutter modelling approach and is addressed by considering fusion of radar remote sensing data, and mitigation of speckle noise and data transmission impairments. The advantages of the intelligent sensor approach for predicting radar performance are demonstrated for several applications using measured data.

The problem of predicting site-specific land radar performance is an important task which is complicated by the peculiarities and characteristics of the radar sensor, electromagnetic wave propagation, and the environment in which the radar is deployed. Airborne remote sensing data can provide information about the environment and terrain, which can be used to more accurately predict land radar performance.

This thesis investigates how fusion of remote sensing data can be used in conjunction with a sensor modelling approach to enable site-specific prediction of land radar performance. The application of a radar sensor model and *a priori* information about the environment, gives rise to the notion of an *intelligent radar sensor* which can adapt to dynamically changing environments through intelligent processing of this *a priori* knowledge.

This thesis advances the field of intelligent radar sensor design, through an approach based on fusion of *a priori* knowledge provided by remote sensing data, and application of a modelling approach to enable prediction of radar sensor performance. Original contributions are made in the areas of intelligent radar sensor development, improved estimation of land surface clutter intensity for site-specific low-grazing angle radar, and fusion and mitigation of sensor and data transmission impairments in radar remote sensing data.

Acknowledgements

I am especially thankful to my supervisor Professor Ken Lever, for all his guidance, support, and whose mastery of the English language, rigour and attention to detail has encouraged me to strive for perfection.

I would like to express my sincere gratitude to Dr Andrey Kurekin who has been not only a friend, but a source of constant support and encouragement, whose knowledge and guidance has been a true inspiration.

I am grateful to my supervisor Dr Dave Marshall for support throughout my studies and whose suggestions and comments were always helpful and appreciated.

It is difficult to overstate my gratitude to my parents Susan and Neil Radford, for always guiding me in the right direction, without whom I would not be in the position I am, and for their love and continual encouragement to achieve to the best of my ability. To them I dedicate this thesis.

I am indebted to my loving partner Michelle for her patience and support during my studies, and the encouragement to follow my dreams.

I thank my amazing children Corey and Kyla, for understanding that Daddy could not always play with them and give them the attention they so rightly deserve.

I would like to thank the Data and Information Fusion Defence Technology Centre, United Kingdom for supporting my research.

I would also like to thank the Kalmykov Centre for Radiophysical Sensing of Earth, Kharkov, Ukraine for providing radar data for experimental study.

List of Contents

List of Figures

List of Tables

List of Acronyms

AI	Artificial Intelligence
AIRS	Airborne Intelligent Radar Sensor
AVI	Audio Video Interleave
AWGN	Additive White Gaussian Noise
CFAR	Constant False Alarm Rate
CNR	Clutter-to-Noise Ratio
CUT	Cell Under Test
DARPA	Defense Advanced Research Projects Agency
DEM	Digital Elevation Model
DFAD	Digital Feature Analysis Data
DIF DTC	Data and Information Fusion Defence Technology Centre
DoD	Department of Defense
DSP	Digital Signal Processor
DTCWT	Dual Tree Complex Wavelet
DTED	Digital Terrain Elevation Data
DVD	Digital Versatile Disc
DWT	Discrete Wavelet Transform
ES	Expert System
FFT	Fast Fourier Transform
FIR	Finite Impulse Response
FPGA	Field Programmable Gate Array
GCP	Ground Control Point
GIG	Global Information Grid
GIS	Geographic Information System
GLRT	Generalised Likelihood Ratio Test
GMTI	Ground Moving Target Indicator
GO	Geometric Optics
GPU	Graphics Processing Unit
IID	Independent and Identically Distributed
IRS	Intelligent Radar Sensor
KA	Knowledge-Aided
KASSPER	Knowledge-Aided Sensor Signal Processing Expert Reasoning
KASTAP	Knowledge Aided Space Time Adaptive Processing
KB	Knowledge Base
KBC	Knowledge Base Controller
KBMapSTAP	Knowledge Base Map Space Time Adaptive Processing
KBSTAP	Knowledge Base Space Time Adaptive Processing
LCLU	Land Cover Land Use
ML	Maximum Likelihood
MoD	Ministry of Defence
MR	Multiresolution
MRDCT	Multiresolution Discrete Cosine Transform
MS	Maximum Selection
MTI	Moving Target Indicator
NCW	Network-Centric Warfare
NEC	Network Enabled Capability

NLCD	National Land Cover Data
NN	Neural Network
PDE	Partial Differential Equation
PDF	Probability Density Function
PE	Parabolic Equation
PO	Physical Optics
PSD	Power Spectral Density
Q-Shift	Quarter Sample Shift Orthogonal filter
RCS	Radar Cross Section
RBFC	Radial Basis Function Classifier
RBNN	Radial Basis Neural Network
SAR	Synthetic Aperture Radar
SCNR	Signal-to-Clutter-plus-Noise Ratio
SIR	Signal-to-Interference Ration
SIR-C	Spaceborne Imaging Radar C band
SLAR	Side Looking Aperture Radar
SNR	Signal-to-Noise Ratio
SOA	Service Oriented Architecture
SSS	Split Step Solution
STAP	Space Time Adaptive Processing
SVM	Support Vector Machine
USGS	United States Geological Survey
WA	Weighted Average
WBV	Window Based Verification
WMV	Windows Media Video

List of Symbols

α	parameter alpha trim
α	phase difference between the direct and reflected waves
γ	parameter describing the scattering effectiveness
γ_c	calibration channel attenuation
$\Delta\psi$	reduction in grazing angle for spherical Earth model
ΔR	range resolution
ΔR_g	ground projection of ΔR
δ_0	pathlength difference for the reflected wave
ε_c	complex dielectric constant
ε_r	relative dielectric constant
θ_A	antenna 3-dB elevation beamwidth
θ_E	antenna 3-dB azimuth beamwidth
θ_t	target elevation angle
θ_r	clutter region depression angle
θ_r	reflection point depression angle
λ	radar wavelength
ρ	magnitude of the surface reflection coefficient
ρ_0	Fresnel reflection coefficient
ρ_s	specular scattering coefficient to account for surface roughness
ρ_v	vegetation absorption coefficient
σ^0	backscattering coefficient
σ^0_{cm}	site-specific backscattering coefficients
σ^0_{cross}	cross-polarised component of the normalised Radar Cross Section (RCS)
σ^0_{HH}	backscattering coefficient horizontally transmitted and received polarisation
σ^0_{LB}	backscattering coefficient for the land-based radar
σ^0_{RS}	backscattering coefficient from the remote sensing radar
σ^0_{VV}	backscattering coefficient vertically transmitted and received polarisation

σ_c clutter cross section

σ_e conductivity of the surface material

σ_h surface roughness

σ_n coefficient of variation of speckle

σ_t target Radar Cross Section (RCS)

υ aperture efficiency

$\hat{x}$ unit vector along the Cartesian coordinates

$\hat{y}$ unit vector along the Cartesian coordinates

$\hat{z}$ unit vector along the Cartesian coordinates

ξ_x the local slope along the x coordinates

ξ_y the local slopes along the y coordinates

ϕ phase angle of the reflection coefficient

$\varphi(t)$ phase

ψ grazing angle

ψ_r radar grazing angle

ψ_t target grazing angle

ψ_B Brewster angle

ψ_{LB} local grazing angle for the position of the land-based radar

ψ_{RS} grazing angle for the remote sensing radar

Ψ^2 variance of noise

Γ_h reflection coefficient for horizontal polarisation

Γ_v reflection coefficient for vertical polarisation

A amplitude of sine wave

A_0 illuminated area

A_1 the Coefficient A_1 for the Land Clutter Model

A_2 the Coefficient A_2 for the Land Clutter Model

A_3 the Coefficient A_3 for the Land Clutter Model

A_c clutter patch illuminated area

A_e antenna effective aperture

A_{MBc} area for mainbeam clutter

A_{SLc} area for sidelobe clutter

B receiver bandwidth

c constant

D divergence factor to account for a spherical Earth

$\mathbf{D}^{(m,n)}$ DCT coefficients of the l^{th} decomposition level of Laplacian pyramid

$D_{ij}^{(m,n)}$ ij^{th} spectral coefficient of the signal in the window

E electric field intensity of the received signal

E_0 free-space field intensity

E_E effective Earth's radius

E_R the Earth's radius

erfc(·) complementary error function

F propagation factor to account for tropospheric propagation

F^4 fourth-power propagation factor

F_i interference propagation factor

F_n noise figure

$\hat{\mathbf{F}}$ the vector version of Equation (5.16)

$f(\cdot)$ voltage pattern of the antenna

f radar frequency

f_0 radar operating frequency

f_i original signal

$\tilde{f}_i$ logarithmic transform of the original signal

f_{LB} land-based radar operation frequency

f_{RS} remote sensing radar operating frequency

f_0 radar operating frequency

$\hat{\mathbf{f}}$ denoised estimate of the noisy signal $\mathbf{g}$

$f(r,n)$ point target response function

G antenna gain

$\mathbf{G}$ Laplacian transform coefficients

$\mathbf{G}$ wavelet transform coefficients

$\mathbf{G}^{(m,n)}$ Laplacian transform coefficients

$\mathbf{g}$ noisy signal to be analysed

g_i the observed noisy signal

$\tilde{g}_i$ logarithmically transformed signal

$\hat{H}_{ij}^{(m,n)}$ denoised estimate

$\hat{\mathbf{h}}^{(m,n)}$ denoised estimate of the Laplacian pyramid transform coefficients

h height of the radar platform

$h(r,c)$ complex samples from the SAR hologram

h_e effective decrease in terrain height with range

h_r radar height

h_r' radar height with respect to the tangent specular point

h_t target height

h_t' target height with respect to the tangent

I_0 modified Bessel function of order

$\hat{I}$ marginal L-estimate algorithm

I SAR image samples

J complex amplitude estimate of the reflected signal

k Boltzmann's constant

k_α attenuation coefficient

L loss factor

$\mathbf{L}^l$ l-stage Laplacian transform

$\left(\mathbf{L}^l\right)^{-1}$ inverse Laplacian pyramid transform

L_α atmospheric loss

L_p antenna pattern beamshape loss

L_t transmission loss

L_x signal processing loss

M sample of $m(t)$

$m(t)$ the envelope of $v(t)$

N length of the synthetic aperture in samples

$\tilde{n}_i$ signal-independent noise component

n_i noise with unity mean and variance

$\hat{n}$ surface normal

$\hat{n}_r$ unit vector from the surface position pointing towards the radar

P_e power of the transmitted signal

P_k power of the recorded calibration signal

P_r received signal power

P_t peak transmitted power

P_{imp} probability of impulse noise

p_x x axis point coordinates for the ground range

p_y y axis point coordinates for the ground range

Q Marcum's Q-Function

q_x x axis point coordinates for the slant range

q_y y axis point coordinates for the slant range

R range to the target

R_1 multipath reflected pathlength 1

R_2 multipath reflected pathlength 2

R_g ground range

$R_{\min}$ minimum slant range

$R_{\min}$ minimum detection range

$R_{\max}$ maximum detection range

r ground range

S terrain visibility map

T global threshold for soft thresholding

$\mathbf{T}$ the DCT transform

T_e effective noise temperature

t_{int} radar integration time

$v(t)$ output of the bandpass IF filter

v_I in-phase component

v_Q quadrature component

V_T voltage threshold

$\mathbf{W}^l$ l-stage wavelet transform

$\left(\mathbf{W}^l\right)^{-1}$ the inverse wavelet transform

w_{ij} weighting coefficients

$w(n)$ weighting function

Publications

The following publications originate from the work undertaken during this Ph.D. program. The fourth publication describes research which is only loosely related with the main focus of the research and therefore is not referenced in the main body of the thesis.

Published

1. Kurekin A., Marshall D., Radford D., Lever K., Lukin V., "Robust Processing of SAR Hologram Data to Mitigate Impulse Noise Impairments", ISIF and IEEE Information Fusion 2005 Conference, Philadelphia, USA, July 2005.

2. Kurekin A., Marshall D., Radford D., Lever K., Dolia A., "Mitigation of Sensor and Communication System Impairments for Multichannel Image Fusion and Classification", ISIF and IEEE Information Fusion 2005 Conference, Philadelphia, USA, July 2005.

3. Radford D., Kurekin A., Marshall D., Lever K., "A New DCT-based Multiresolution Method for Simultaneous Denoising and Fusion of SAR Images", ISIF and IEEE Information Fusion 2006 Conference, Florence, Italy, July, 2006.

4. Kurekin A., Marshall D., Radford D., Lever K., Kulemin G., "Assessment of Soil Parameter Estimation Errors for Fusion of Multichannel Radar Measurements", ISIF and IEEE Information Fusion 2006 Conference, Florence, Italy, July, 2006.

Submitted for publication, currently responding to referees comments

5. Kurekin A., Radford D., Kulemin G., Lever K., Marshall D., "Site-Specific Land Clutter Modelling by Fusion of Radar Remote Sensing and Terrain Data", Journal on Information Fusion, Elsevier.

Personal Contributions to each Publication

1. 40%
2. 20%
3. 85%
4. 5%
5. 65%

Chapter 1

Introduction

This introductory chapter starts with a discussion on the motivating factors for the development of a *fusion-based intelligent radar sensor*. Impairments which have a negative influence on radar performance are then discussed. A historical survey of intelligent radar systems follows, in which a number of unsolved problems are identified; and several are selected to form the basis of the research reported in this thesis.

1.1 Motivation

This Doctoral research program was part of a larger research project funded by the Data and Information Fusion Defence Technology Centre (DIF DTC) [1]. The objective of this research programme was to investigate impairments caused by sensors, radio channels, communication equipment and the environment. The aim of the project is to improve the reliability and effectiveness of data and information fusion algorithms by means of modelling, evaluating and mitigating errors appearing in sensors and their associated data communication systems. Therefore, the scope of this thesis is restricted only to problems that can be solved using a data fusion approach.

Data fusion can be applied for fusion of many different sources of information including but not limited to sensor outputs, sensor models, environment models and other data such as human observations, databases and knowledge-based data. Data fusion provides a method for combining information from multiple sources to produce an observation of a particular event with higher accuracy than that obtained from any individual source. In remote sensing applications data fusion is commonly used for fusing information from various modalities and sources [2, 3]. Within the data fusion

community the commonly accepted model for data fusion systems is the JDL-User model [4], although, this model has not been adopted in this thesis.

This thesis focuses on data fusion for radar applications. Radar sensor measurements are affected by impairments produced by the sensor itself, the environment and other sources such as data transmission errors when the radar sensor is networked over communication links. These impairments degrade the quality of the data which will be used as data sources for the fusion process. Therefore, to provide accurate information for data fusion it is necessary to mitigate these impairments prior to fusion. Modelling techniques provide the opportunity for efficient mitigation by modelling sensors, the environment and other sources of impairments, allowing suitable mitigation techniques to be applied.

Radar sensors that are deployed in hostile environments experience degradation of performance in detection of targets caused by the peculiarities of the environment itself. The major factors which influence radar performance under these hostile conditions are signal returns from land clutter, multipath propagation effects, and the characteristics of the radar sensor. The influence of land clutter and multipath propagation are dependent upon the type of environment in which that radar is deployed. Therefore, we require information about the terrain in order to predict radar performance within the environment. This information can be provided by other sensor modalities such as multi/hyperspectral, remote sensing radar, or obtained from geographical databases.

The idea of using additional information to predict radar performance gives rise to the notion of an Intelligent Radar Sensor (IRS) which is aware of its surroundings. Through intelligent processing of this *a priori* information the radar can more accurately predict its own performance based on this site-specific knowledge of the terrain. The prediction of site-specific radar performance is an important task which has many potential applications such as radar sensor deployment, radar network coverage optimisation, and mission planning of aircraft flight paths to avoid detection by hostile radar. The core idea of the IRS presented in this thesis is based on fusion of remote sensing data about the environment to improve prediction of radar sensor performance for site-specific applications.

Remote sensing of a geographical region by application of different sensors for the monitoring of the same area presents the opportunity to fuse the information obtained by the sensors, providing a more information-rich view of the area. Sensors operating in the radiowave band are particularly suitable for this type of application; because they utilise different frequency sub-bands, polarisations, incidence angles and different observation times to provide additional information and improve the reliability of the data. In addition, the use of data fusion permits a degree of robustness in the system, and may also be used to resolve any discrepancies between the sensors. Synthetic Aperture Radar (SAR) can provide information complementary to optical and multi/hyperspectral images, all of which are widely used for joint monitoring of a region of the Earth's surface. Additionally, Digital Terrain Elevation Data (DTED) can be utilised to construct 3D models of the terrain profile. Remote sensing data therefore, provides a wealth of information about the land surface and fusion of this data presents the opportunity for improved understanding of the environment.

The IRS approach presented in this thesis fuses information about the environment obtained from various remote sensing modalities to assist in prediction of site-specific radar performance. Therefore, an important component of this IRS approach is the ability to share information between heterogeneous sensors, which requires reliable communication channels and a suitable framework for the transmission and sharing of data. In Section 1.1.1 we discuss the recent technological advancements that enable sensor communication and data sharing between sensors. All of these play an important role in the intelligent radar sensor concept presented in this thesis and enable the acquisition of up-to-date information about the environment in which the radar is deployed.

1.1.1 Sensor Communication and Data Sharing

Technologies and frameworks are being developed to allow communication and data sharing for heterogeneous sensors in a structured and meaningful fashion. By 'meaningful' it is meant that: data produced by sensors can be stored along with contextual information which will allow other sensors to use the data in a more

efficient manner. One such approach characterised as *net-centric* [5], is based on semantic webs and ontologies. Semantic webs give meaning and context to data and information so that they can be understood by computers and used in a more efficient way. Ontologies provide an agreement on the vocabulary for more efficient communication between devices. This allows heterogeneous sensors to communicate, understand each other and share information. The US Department of Defense (DoD) adopted the net-centric model for the architectural design of the Global Information Grid (GIG) in order to support Network-Centric Warfare (NCW) [6]. The GIG is defined by the US DoD [7] as

> "... *a globally interconnected, end-to-end set of information capabilities, associated processes, and personnel for collecting, processing, storing, disseminating, and managing information on demand to warfighters, policy makers, and support personnel.*"

A similar initiative by the UK Ministry of Defence (MoD) related to the net-centric approach is known as *Network Enabled Capability* (NEC) [8]. This uses a Service-Oriented Architecture (SOA). NEC focuses on networking people and assets to enable information sharing in order to fulfil mission objectives. A new tactical communication system known as Bowman [9] has been developed to replace the current British Armed Forces communication system. Bowman is a fundamental component of NEC providing the capability for data transmission and communication. Current research in NEC focuses on development of metrics and measures for enhancing system dependability [10].

The GIG and NEC methodologies provide a structured approach for sharing data and information between heterogeneous sensors. These give rise to the opportunity for many new intelligent radar sensor applications that can benefit from the availability of high-quality information on-demand and in real-time. This combined with reliable transmission channels such as Bowman permits the acquisition of data from disparate sensors to provide up-to-date information about the terrain. The infrastructure is therefore already in place to support the IRS approach.

We have discussed the emerging technologies that will enable the development of intelligent sensor systems which rely on information from other sensors. Section 1.2

discusses the relevant background material associated with radar performance and how the environment affects radar sensor performance.

1.2 Background

Firstly, it is important to identify the impairments produced by sensors, communication equipment, and the environment. For radars, environmental factors such as precipitation and illumination (low lighting conditions or night time operation) pose no problem due to the operating characteristics of radar, such as the ability to obtain measurements in complicated environment conditions due to the properties of electromagnetic wave propagation. However, land clutter and multipath propagation effects are major problems which limit the operation and performance of radar.

For surface-sited radar used for detection and tracking, one of the major sources of impairment is *land clutter* which severely impairs the sensor's ability to detect signals of interest. Clutter refers to the unwanted radiowave echoes reflected by the Earth's surface and other objects in the environment such as birds, fog and rain. Clutter falls under two broad categories, *volume clutter* and *surface clutter*. Volume clutter refers to unwanted signal returns caused by precipitation, birds and insects. Surface clutter arises from reflections from the sea and land. Although volume and sea clutter are important factors it was decided to restrict attention to land-based radars and only consider land clutter. Land clutter modelling is considered in detail in Chapter 5. Signals produced by clutter can often be much stronger than the signal reflected by the object of interest. Ground clutter in particular, can severely degrade the performance of ground-based low-grazing radar for tasks such as tracking and detection of low altitude aircraft or missiles [11]. Strong clutter can mask signal returns from weak targets and as a result can severely impair radar performance.

Atmospheric refraction and ducting caused by radiowave propagation through the atmosphere can lead to bias in the target elevation angle resulting in inaccurate measurement of target position [12]. Atmospheric refraction and ducting can be efficiently modelled using parabolic equations with suitable boundary conditions [12],

however this is beyond the scope of this thesis. Instead, a simplification for atmospheric refraction is implemented in this thesis. This is based on the assumption of a linear change in the refractive index with altitude, and leads to the four-thirds Earth radius model [13, 14].

Multipath interference is one of the most important non-free-space effects, resulting in constructive and destructive interference at the receiver. Multipath effects due to radiowave reflections from the Earth's surface result in interference lobes in radar coverage [12], with the shape and position of the lobes dependent on characteristics of the surface reflecting the radiowave. This leads to an increase or decrease in radar detection range.

Signal returns from land surface clutter and multipath propagation are major sources of impairment for surface-sited radar operating at low-grazing angles. The presence of such impairments can significantly reduce the performance of the radar in detecting and tracking targets at low altitude due to signal returns from the land surface which can mask the signal returned from targets. Remote sensing data can provide valuable information about the environment and therefore can be used for prediction of land surface clutter for radar and multipath radiowave propagation. Modelling the radar and the environment provides the opportunity to improve radar sensor performance through application of *a priori* information about both the environment and the radar sensor to predict radar sensor performance with higher accuracy. The *a priori* information required depends solely on the phenomena to be modelled; for example, if we wish to predict strong discrete scatterers from the clutter returns then we may use data derived from a Geographic Information System (GIS) to identify the spatial location of problematic sources such as radio masts, power masts, and roads with moving traffic. Incorporating this *a priori* information directly within the radar sensor leads to the concept of an Intelligent Radar Sensor (IRS) that is capable of adapting to changes within the environment to improve overall radar performance.

The idea of an IRS is to predict radar sensor performance by modelling the characteristics of the sensor, its environment and interferences; then incorporating this *a priori* knowledge within the sensor system to improve sensor performance. The sensor model will provide a mechanism for predicting the performance of the sensor,

providing the opportunity to tune operating parameters for better performance. The system should contain information about factors which affect the performance of the sensor, such as, terrain elevation data and land surface type.

From this discussion it is apparent that the accuracy of sensor measurements are not only affected by the characteristics of the sensor itself but are also influenced by environmental factors. Therefore, accurate modelling of sensors, the environment and other impairments is necessary to improve the accuracy of the sensor measurements. Data fusion plays a central role in the IRS system presented in this thesis by combining data from the sensor models, remote sensing data, and internal models (of clutter and the environment) to improve prediction of radar sensor performance.

There are four inter-related main topics for research within this thesis:

- Modelling radar performance
- Modelling impairments due to the environment
- Improving the efficiency of data fusion and modelling
- Developing an intelligent radar sensor concept

Specific innovations in these areas are discussed in Section 1.4. The issues surrounding these topics have been discussed in this section and we will now focus on the advancement of intelligent radar sensors within the radar research community. Section 1.3 assesses the current state of intelligent radar systems design and development.

1.3 A Historical Survey of Intelligent Radar System Development

The following historical survey on intelligent radar systems begins with innovations made during the late 1980s and concludes with the most recent contributions made up until the date of this thesis. The radar systems discussed in this section can be regarded as intelligent because they use additional information provided by other sources to augment radar operation and improve radar system performance.

In order to develop intelligent systems it is necessary to draw from the Artificial Intelligence (AI) domain of which two areas are most applicable: robotics and expert systems (ES) [15]. The aim of robotics is to develop autonomous systems that are able to adapt to dynamic environments in order to meet pre-determined goals without human intervention. Expert systems, on the other hand, try to embed the behaviour of an expert within the system to allow autonomous behaviour of the system in an expert fashion. Knowledge-Based (KB) systems [16] are a particular form of ES, in which heuristics and rules are developed to allow the system to react in an intelligent manner. The following discussion identifies recent developments in the area of intelligent radar sensor design and describes how AI techniques are currently being employed to promote intelligent behaviour in radar systems.

1.3.1 Knowledge-Based Systems

The task of improving radar performance through the use of *a priori* information has been the subject of substantial attention in the radar research and development community [16-23]. KB systems aim to modify the radar signal processing chain in response to changes in the environment and operation conditions, by using additional information about the environment provided by other sensors, prior knowledge and prediction techniques.

Pioneering research into the use of AI for enhancing radar signal processing considered the KB approach for improved surveillance radar performance in tracking and identification of targets [16]. A knowledge base consisting of constraints on target dynamics was implemented to improve target tracking, and KB target feature matching to facilitate in target identification. In [15] an ES was proposed for intelligent allocation of radar sensor resources using a KB resource allocator to assess environmental conditions to determine zones (critical locations representing threat conditions) and prioritise radar resources accordingly. Data from previous scans provided information about the electromagnetic interference, which was used by the knowledge-base to assign radar parameters, modes and processors based on constraints set by the user. The idea of an intelligent radar sensor capable of learning and developing cognition of the environment through continuous interaction with the

environment over time (i.e. normal radar operation of obtaining measurements) was proposed in [17]. The proposed architecture employed a knowledge processor to incorporate prior knowledge into the system and a Neural Network (NN) classifier to enable learning and modelling of sea clutter for improved detection of weak targets in sea clutter.

Initial research [18] conducted by the US Air Force Research Laboratory's Sensors Directorate demonstrated how the Constant False Alarm Rate (CFAR) process (an adaptive detection algorithm in which the threshold is varied to maintain a constant false alarm rate) can be modified to improve probability of detection and lower false alarm rates by performing cell averaging only on cells with the same type of clutter as the test cell. This is achieved by using direct measurements obtained by the sensor to categorise each cell based on the statistical nature of the clutter. Further work led to a patent for an Expert System (ES) CFAR processor consisting of both rule-based and data-based approaches: using direct measurements obtained by the radar to assess the interference environment and then rule-based selection of an appropriate CFAR algorithm from the internal database of CFAR algorithms [19].

The idea of using additional data sources to improve the detection process as in [18] was extended to include the filtering and tracking processes of surveillance radar. This approach is known as Knowledge-Based Space Time Adaptive Processing (KBSTAP). The initial concept of KBSTAP was proposed for airborne early warning radar to deal with non-homogeneous environments [20] demonstrating the use of map data to place antenna nulls at the position of interference. Here the KB is responsible for selection of STAP configuration, algorithms, parameters, and utilising map data to select secondary data cells not containing interference. Further research [21] considered the use of terrain data from the United States Geological Survey (USGS) to improve the performance of STAP by intelligent selection of range rings surrounding the test range ring. This approach is known as Knowledge-Based Map Space Time Adaptive Processing (KBMapSTAP).

The US Air Force developed the initial KBSTAP architecture for knowledge-based control of the radar signal processing chain [22] as shown in Figure 1.1.

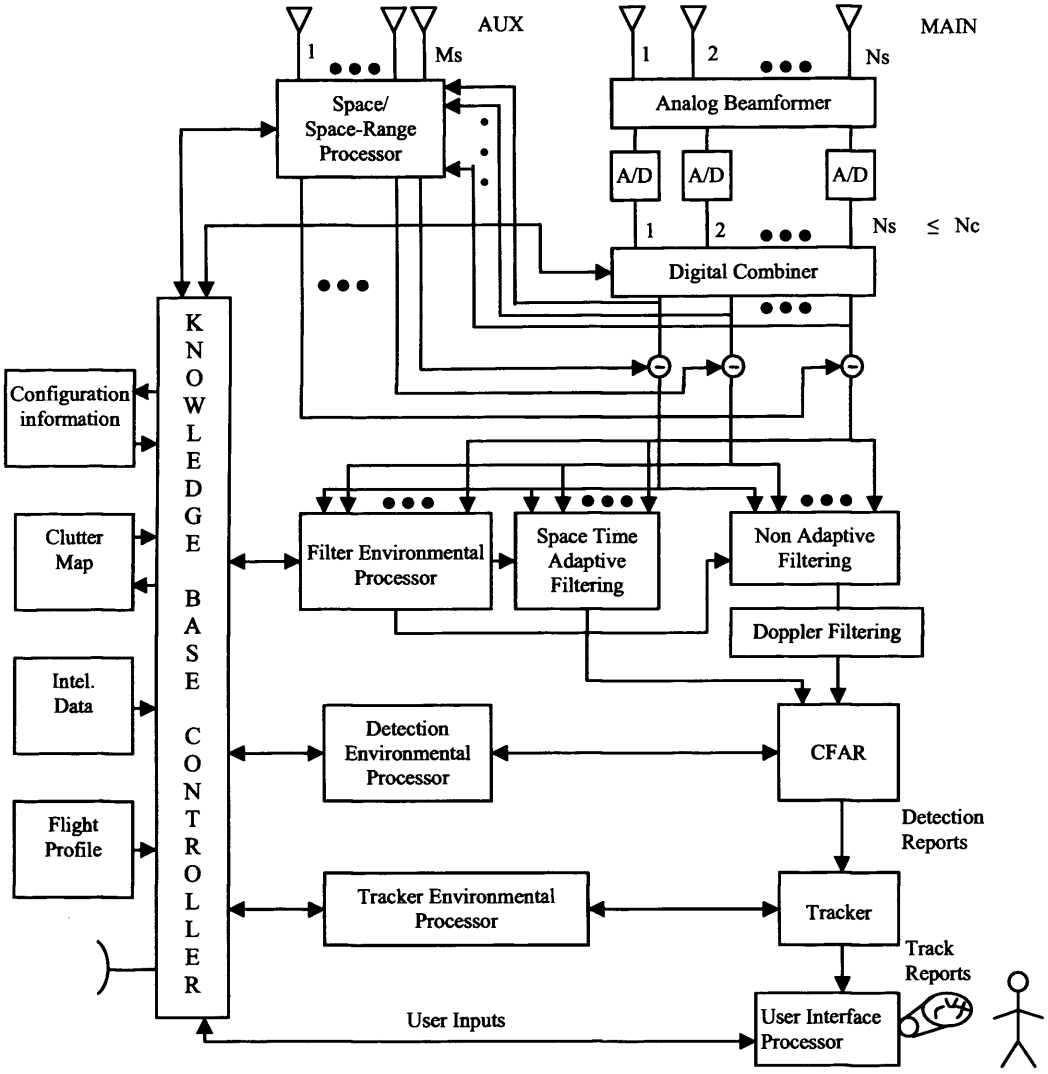

Figure 1.1 Initial KBSTAP Architecture (taken from [23])

The system can be considered as four main processes: the Knowledge Base Controller (KBC), filter processor, detection processor, and track processor. The KBC controls the entire signal processing chain, using terrain information from various sources such as Digital Terrain Elevation Data (DTED), Land Clutter Land Use (LCLU) maps, and multi/hyperspectral data to modify the processing chain by selection of appropriate algorithms and parameters. KBC consists of a knowledge base containing information about the specific problem domain and an inference engine to reason, draw conclusions and learn. The next section discusses how this KB approach has been applied for autonomous sensor operation identifying which processes of the radar signal processing chain are modified and the various sources of *a priori* data used for each approach.

1.3.2 Autonomous Systems Applications

This early research in KB systems [18-21] prompted the US Defense Advanced Research Projects Agency (DARPA) to launch the Knowledge-Aided Sensor Signal Processing Expert Reasoning (KASSPER) program to investigate how Ground Moving Target Indicator (GMTI) radar performance can be improved by using additional data sources and *a priori* information to minimise the impact of heterogeneous clutter [24, 25]. A real-time Knowledge-Aided (KA) STAP (KASTAP) architecture was proposed using *a priori* information and look-ahead scheduling. In the context of intelligent sensors KA and KB essentially refer to the same concept of using prior information to improve sensor performance. However, they have different architectures. A KA detection architecture for GMTI is presented in [26] for modification of STAP to improve target detection by mitigating the effects of non-homogeneous clutter. A three-stage approach was adopted. Firstly, a partially adaptive KA pre-filter used metrology measurements to anticipate and remove predictable components of the clutter response. Then the data was pre-whitened by using Synthetic Aperture Radar (SAR) data to identify and predict large clutter returns, and filtered using a discrete matched filter. Finally, map data was used to identify road networks to remove target-like signals such as moving traffic from the training data. In [27] National Land Cover Data (NLCD) was used to support selection of homogeneous secondary cells for STAP demonstrating improved performance over standard STAP.

Design and analysis of a knowledge-based radar detector is considered in [28] using Geographic Information System (GIS) data to deal with non-homogeneous clutter and strong outliers. This approach demonstrated improved detection using topographic data first to eliminate static outliers from the secondary data, then a data adaptive secondary data selector which employs a statistical Maximum Likelihood (ML) criterion to select the most suitable homogenous training data. In [23] the authors adopted the KBSTAP architecture for an airborne Autonomous Intelligent Radar Sensor (AIRS), in which preloaded map data is used to estimate clutter statistics. They also extended the initial KBSTAP architecture shown in Figure 1.1 to include other sources of information as input to the KBC. Also in [23] the net-centric approach is applied for an AIRS system as shown in Figure 1.2 to allow data sharing.

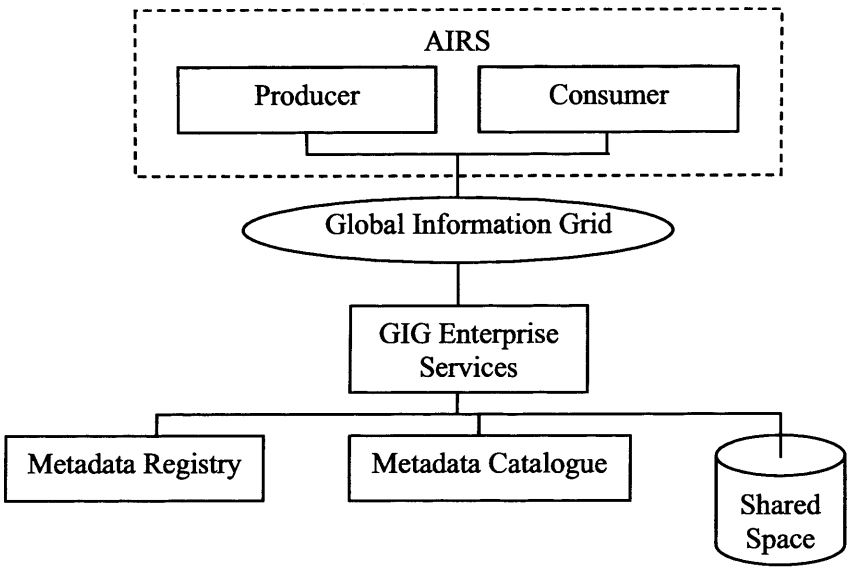

Figure 1.2 AIRS and the net-centric approach (taken from [23])

A KB detector for STAP in airborne radar is considered in [29]. This exploited knowledge of the clutter ridge (the locus in the Doppler-angle domain where the clutter Power Spectral Density (PSD) is different from zero). It is demonstrated that knowledge about the characteristics of the clutter ridge and a Generalised Likelihood Ratio Test (GLRT) can provide a capability for rejection of interference close to that of the optimum detector, based on perfect knowledge of the clutter covariance matrix. Another knowledge-based approach proposed in [30] explored the concept of cognitive radar, where the architecture was inspired by the echo-location system of a bat. In this approach prior knowledge of geographic and target kinematics data was used to improve radar performance for target detection in sea clutter. Learning was enabled through feedback from the receiver to the transmitter. A Bayesian approach was employed to detect and track targets in sea clutter, then through intelligent control, the radar illumination of the environment was adjusted to account for target size and range to improve the tracking and detection performance of the radar.

A full discussion on the advantages of KB approaches for improved radar performance can be found in [31, 32]. An overview of the KASSPER program can be found in [33], where the benefits of KA adaptive radar and a new radar scheduling approach are discussed. Attention is also paid to prior knowledge methods of space-time adaptive beamforming for GMTI radar. The potential of KB approaches for

solving the problems associated with STAP can be found in [34]. An overview of KASTAP applications is presented in [35], identifying the advantages of using SAR data for predicting clutter interference for airborne radar. A real-time architecture for KA adaptive radar is presented in [36]. This architecture extends the KASSPER architecture to include modification to both transmit (adaptive waveform optimisation) and receive (STAP processing) functions of the radar signal processing chain. A real-time environmental dynamic database provided sensor situation awareness, combined with a look-ahead scheduling scheme to determine an optimal transmit and receive strategy.

In this discussion we have identified recent progress in the development of intelligent radar sensors. Particular attention has been devoted to the architecture for an intelligent radar sensor, focusing on KB and KA approaches, and to the identification of the parts of the radar signal processing chain which have been modified to improve sensor performance. Current research in the radar community addresses the development of KB rules and heuristics, concentrating on modification of several processes of the radar processing chain including detection, tracking, and filtering. Most noteworthy in the context of this thesis is the AIRS approach [23] in which preloaded map data is used to estimate clutter statistics. However, it is desirable to predict clutter with high accuracy for optimal radar performance. Using map data and statistical estimations is not the optimal solution for predicting clutter because it does not account for site-specific factors which influence clutter intensity such as local grazing angle and multipath fading. Instead, backscattering intensity measurements and land backscattering models can be applied to predict clutter with higher accuracy and improve selection of platform trajectory. In [32] the authors state that

> "*In the future, a truly intelligent sensor system may even optimize its flight path based on analysis of real time and archival data.*"

KB approaches have been the subject of considerable research and it can be seen that, generally, the radar research and development community has embraced the KB approach and that research is under way in the development of rules and heuristics for the KB. Additionally, considerable effort has been devoted to modification of the

various processes of the radar signal processing chain to improve radar sensor operation.

Recent research has demonstrated the advantages of using *a priori* information to model the environment for mitigation of natural and man-made interference to improve radar sensor performance. In [17], an intelligent radar is proposed which developed cognition of the environment (in this case sea clutter) through direct sensing by the radar sensor itself. Other approaches considered application of map data [20, 26] and terrain data [21, 27] to augment modelling of the environment. Although these approaches employ *a priori* information to provide a model of the environment the advantages of fusing information about the environment provided by remote sensing data has not been considered. Therefore, the opportunity exists to improve environment modelling through fusion of remote sensing terrain data.

In response to the literature survey, the following problems have been identified and will be addressed in this thesis:

- How can we predict radar performance using a fusion and modelling approach?
- How can we improve the prediction of land clutter by fusing various sources of data about the environment?
- How can we improve the quality of remote sensing radar data through a modelling and data fusion approach?

In Section 1.4 we will now summarise the novel contributions made in each of these areas.

1.4 Summary of Novel Contributions

The major contribution presented in this thesis is an intelligent radar sensor which employs fusion of remote sensing data to more accurately predict impairments which influence radar performance. Combining this with a radar sensor model permits

higher accuracy of site-specific radar performance prediction. With respect to the problem of how to improve the prediction of radar performance, the approach presented in this thesis proposes fusion of remote sensing data acquired by different sensors to combine information about the terrain, then using this information for more accurate prediction of land clutter and multipath modelling. By fusing terrain information obtained from multiple sources we can provide a more detailed description of the environment or terrain, which can then be used to predict site-specific radar sensor performance. The application of a fusion-based approach for an intelligent radar sensor has not been considered in the literature and therefore it is novel.

This approach to an intelligent radar sensor has the following advantages:

- Clutter prediction when direct radar measurements are not available (eg. before deployment).
- Knowledge of the environment through fusion of remote sensing data to improve the prediction of land clutter and multipath effects, hence, improving the prediction of radar sensor performance
- The ability to adapt to dynamic environments by real-time acquisition of up-to-date remote sensing data (using a net-centric approach as discussed in Section 1.3.2 and reliable data transmission channels such as Bowman)
- Improved site-specific prediction of radar sensor performance which can benefit the tasks of sensor placement, optimising radar parameters, and calculation of aircraft flight paths to avoid detection by hostile radar

When predicting site-specific radar sensor performance it is important to consider land clutter as it has a negative influence on radar performance. Land surface clutter is dependent on radar frequency, grazing angle, terrain type, and terrain elevation. Remote sensing data can provide terrain information such as terrain height and land surface type to estimate grazing angle and account for changes in clutter intensity due to changes in grazing angle. Additionally, radar remote sensing data such as SAR or Side Looking Aperture Radar (SLAR), describe electromagnetic wave backscattering from the Earth's surface but for alternative radar positions, grazing angles, and

possibly radar frequency and polarisation. Land backscattering models [37] can be applied to account for these differences between the surface-sited radar and the remote sensing radar. Therefore, through fusion of remote sensing terrain data, radar remote sensing data, and application of land backscattering models we can improve land clutter modelling and prediction of site-specific radar performance.

The novelty in this thesis is contained in Chapters 2, 5, and 6. Chapters 3 and 4 have been included to explain how standard modelling techniques can be applied to developing an intelligent radar sensor. The novel contributions are summarised as follows.

In Chapter 2 the concept of an intelligent radar sensor is developed and an architecture is proposed for an autonomous radar sensor which is capable of adapting to a dynamically changing environment. All aspects of the intelligent radar sensor are discussed, highlighting the importance of each component in the realisation of a radar sensor that can intelligently change some aspect of its operation to improve performance.

Chapter 5 contains three novel contributions:

- A new method for predicting ground clutter using radar remote sensing data
- A new method for mitigating impulse noise and fusing of SAR data
- A new multiresolution DCT-based method for fusing and denoising SAR data

In Chapter 5, a new method is proposed for predicting site-specific land clutter for low-grazing angle radar, with the advantage of fusing radar remote sensing data and application of empirical land backscattering models to improve the accuracy of clutter prediction. A journal paper [38] using remote sensing radar images has been submitted for this research to the Elsevier Journal on Information Fusion. In particular, radar remote sensing data is critical in the new clutter prediction technique, and mitigation of any impairment present in this data prior to further processing will improve the quality of the data and therefore improve the accuracy of clutter prediction.

Modelling and fusion of SAR data with impairments is also considered in Chapter 5. There are comparisons between the Discrete Wavelet Transform (DWT) [39] and the Dual-Tree Complex Wavelet Transform (DTCWT) [40] in the literature, but none of them address fusion of SAR data. The novelty of this research lies in the improvement in fusion results when impairments in SAR data are mitigated prior to fusion. These results have been published in a conference paper [41] and a more complete analysis has been conducted in Appendix 1. All of the material pertaining to fusion of SAR data is both new, and as yet unpublished.

A new multiresolution Discrete Cosine Transform (MRDCT) based method [42] is also proposed in Chapter 5 for the task of simultaneously denoising and fusing SAR remote sensing images. Here sensor impairments, of which speckle noise is predominant, are considered and mitigated at the stage of fusion. The idea behind combining a DCT (which is not a multiresolution technique) and a Laplacian pyramid to form a hybrid multiresolution method is based on exploiting the strengths and advantages of each technique. The efficient noise suppression capabilities and good frequency localisation properties of the DCT combined with the good spatial localisation of the Laplacian pyramid result in the combination of these advantages to achieve good time adaptation and frequency flexibility simultaneously, coupled with the additional benefit of highly efficient noise suppression. This is achieved by incorporating the Laplacian pyramid [43] multiresolution analysis technique and a sliding window DCT for simultaneous denoising and fusion of the multiresolution coefficients. These results have also been published in a conference paper [42] and a more complete analysis has been conducted in Appendix 2. Most of this material is both new, and as yet unpublished.

Chapter 6 demonstrates how the intelligent radar sensor can be applied to several applications. Sensor placement for a single radar sensor, deployment of a radar sensor network, and a mobile radar scenario are considered. The advantages of the intelligent radar sensor for these applications are discussed. The applications in themselves are not novel, but direct application of the intelligent radar sensor to solve these problems is.

1.5 Assumptions Made in this Thesis

The following assumptions have been made in this thesis. When fusing data it is important to note that there are uncertainties associated with each data source, such as the precision and confidence of the observed measurements. However, this thesis neglects the issue of uncertainty for all considered data fusion activities for the sake of tractability and due to time limiting restrictions.

Due to the computational complexity, modelling of multipath effects is restricted to a two-path model. Here, only the direct backscattered signals from the target are considered; therefore, ignoring multipath signals which would arrive at the radar from signals scattering in directions other than the direct backwards path.

For the sake of tractability, a simplified model for atmospheric propagation modelling has been assumed which neglects the effects of changes in the refractivity profile of the atmosphere and ducting effects.

The modelling of clutter is restricted to land clutter, therefore, ignoring volume clutter such as weather for the sake of tractability. However, it is noted that an environment model could be implemented to assist in modelling atmospheric propagation and volume clutter but time restrictions exclude this from consideration in this thesis.

The structure of the thesis is now discussed in Section 1.6.

1.6 Structure of Thesis

In Chapter 2, a new intelligent radar sensor architecture is proposed, which uses terrain data and sensor models to predict and improve radar sensor performance.

In Chapter 3, the radar model is developed and described in the context of an intelligent radar sensor. The limitations and impairments which affect the operation and performance of radar sensor are discussed, highlighting the need for mitigation of impairments prior to further processing.

Chapter 4 addresses the issue of multipath effects for radiowave propagation.

A new fusion-based technique for predicting site-specific ground clutter with high accuracy is described in Chapter 5.

Chapter 6 considers several scenarios for the application of an intelligent radar sensor. Here the advantages of employing an intelligent radar sensor to solve the problems in the chosen scenarios are demonstrated. Thus the novel intelligent radar sensor architecture described in Chapter 2 is evaluated in Chapter 6.

Conclusions are drawn in Chapter 7 and several novel suggestions for future work are proposed.

An extensive reference list of relevant publications follows the main body of text.

Finally, five appendices are presented which discuss topics that are not appropriate for detailed discussion within the main chapters, but are none the less still important topics.

Chapter 2

An Intelligent Radar Sensor Architecture

This chapter starts with a discussion on the concept of intelligence. Then a new architecture is proposed for an intelligent radar sensor based on fusion of remote sensing data and combination of modelling techniques. Critical components of the design are identified and the importance of each component within the proposed architecture is highlighted.

2.1 Discussion on Intelligent Radar Sensor Design

When designing an intelligent system it is important to clearly define what is meant by the term "intelligence" so that models can be developed to achieve the desired specification. The notion of "intelligence" is complex and often has various definitions depending on the context in which it is being defined. The US DoD define intelligence as [44]

> *"The product resulting from the collection, processing, integration, evaluation, analysis, and interpretation of available information..."*

From the viewpoint of intelligent sensor design the following description is appropriate. It is generally accepted that the ability to learn is taken to be a sign of intelligence; however, if learning is not possible then intelligence will be limited by what is currently known. Based on this assumption intelligence can be described as a combination of the following three characteristics:

- Ability to learn from training and past experience
- Ability to pose and recognise problems
- Ability to solve problems by application of knowledge

In summary, intelligence allows application of prior knowledge gained from learning to be applied for recognising, understanding and solving problems.

The rest of this chapter addresses the idea of an intelligent radar sensor (IRS) capable of intelligently adapting to the environment or autonomously reacting to new goals and objectives. In this sense the IRS can minimise the impact of impairments due to ground clutter and multipath propagation by appropriate modification of radar operation or location within the environment. For detection and tracking radar one of the parameters to be optimised is probability of detection. This depends on the radar system characteristics, the nature of the environment in which it is deployed, land clutter, and multipath propagation effects, all of which have complex negative influences on radar performance. In the next section we will discuss the architecture and design of the intelligent radar sensor considered in this thesis.

2.2 Intelligent Radar Sensor Architecture and Design

The architecture for KBSTAP shown in Figure 1.1 has been proposed for KB systems. The initial architecture proposed in this thesis is shown in Figure 2.1, which differs from the KBSTAP architecture in the following ways:

- The KBSTAP approach is specifically for STAP radar and identifies sources of interference using *a priori* information in order to modify the radar signal processing chain to improve radar performance.

- The approach adopted in this thesis is more general and can be applied for a wide range of radar systems. The main idea of this approach is using radar and environmental interference models to predict radar performance in advance in order to optimise radar operation, such as probability of detection.

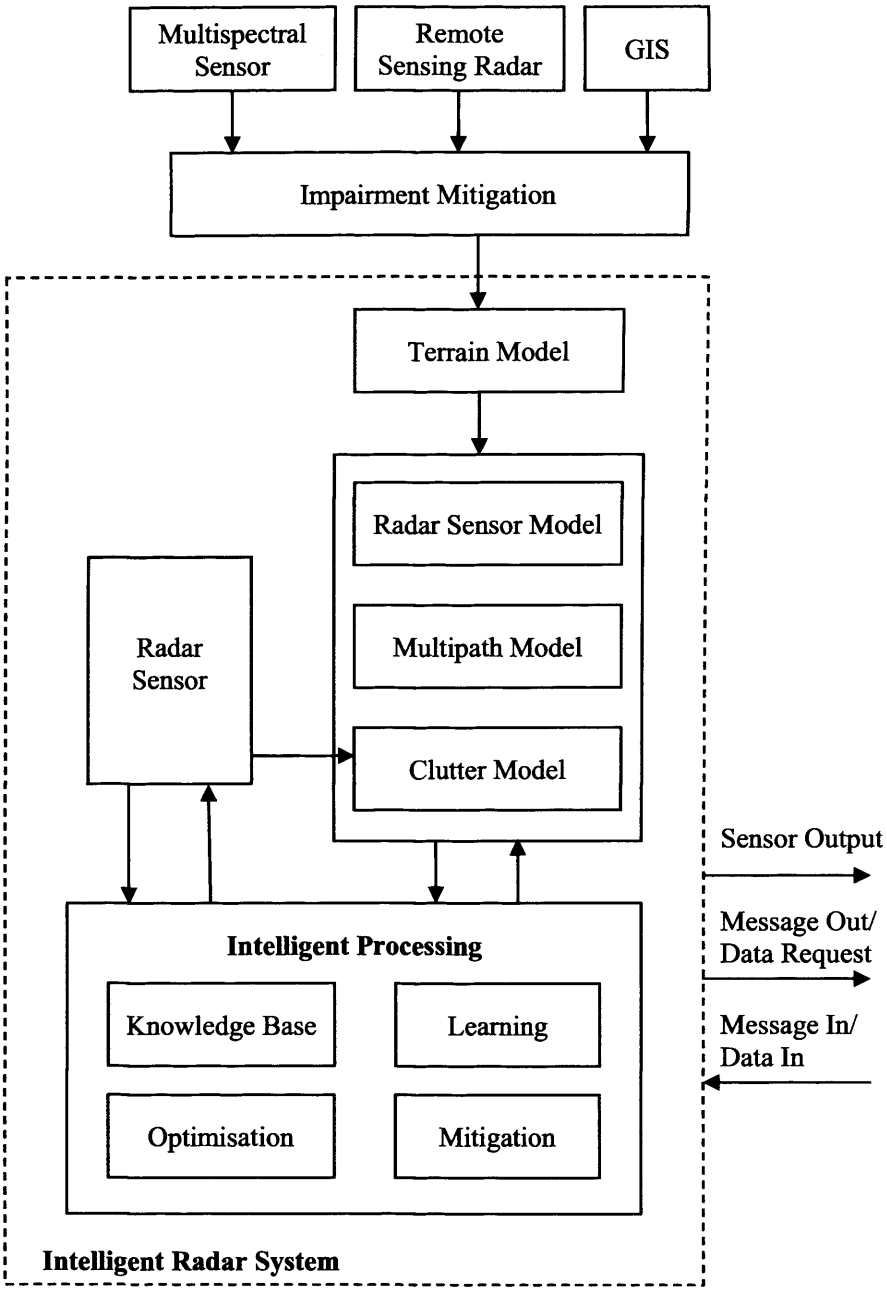

Figure 2.1 Initial Intelligent Radar Sensor Architecture

Here the radar sensor is represented as a block which encompasses all aspects of the radar system. The links between the intelligent processing and individual radar signal processes are not shown as they are unnecessary for the purpose of this thesis. The knowledge base controller is expanded under the intelligent processing block to identify the individual processes of KB, learning and optimisation involved in the intelligent processing chain. All of these are implied under the KBC (shown in Figure 1.1 on page 10), but it is necessary to separate these concepts to identify the necessary components for the intelligent radar sensor in this thesis.

The radar sensor, once deployed, can obtain a clutter map for its current location directly by scanning the region; however, the intelligent radar sensor approach is based on the assumption of predicting radar performance in advance and before deployment of a radar sensor to a new location. Therefore, obtaining clutter maps by direct measurements is not applicable for this situation. The clutter model provides the ability to predict a clutter map for any position within the environment using the clutter prediction technique proposed in Chapter 5. The clutter model here is analogous with the 'clutter map' process in the KBSTAP architecture in which clutter statistics are predicted using preloaded map data [23].

The terrain model contains information about the environment represented by Digital Elevation Model (DEM), topographic data, optical data, radar remote sensing data and terrain classification data. The terrain model provides information to aid in prediction of clutter map data and multipath propagation effects to allow the intelligent radar sensor to adapt to the dynamically changing environment. Other factors that can influence the performance of the radar, such as atmospheric conditions, weather state and volume clutter (birds, insects, etc) can be accounted for by application of an environment model. However, these aspects are not considered in this thesis and are a topic for future research.

The radar model can be compared with the 'configuration information' in the KBSTAP architecture which contains the radar specifications, but it is much more in following sense. The major aspects of the radar are considered including a model of the antenna pattern, allowing for prediction of radar performance such as probability of detection by applying the radar model to the predicted clutter map data. This provides the opportunity for assessment and optimisation of radar sensor operation. Additionally, if the radar sensor has more than one mode of operation such as alternative waveforms (whereby, the sensor has a number of transmit waveforms at its disposal) then all operating modes can be simulated to permit optimal configuration of radar parameters to meet pre-determined objectives. The multipath model predicts the variation of signal strength at the receiver due to multipath propagation of radiowaves reflected by the target. Multipath propagation of radiowaves is considered in detail in Chapter 4.

Learning is a specific topic within the domain of AI. It is beyond the scope of this thesis but the learning component is included in the architecture as a reminder of the importance of learning to increase intelligence. The topic of learning could form the basis for future research.

Optimisation is essential in a fully autonomous sensor, to enable the sensor to react in the most appropriate manner. For the IRS optimisation is required to decide on the best solution out of all possible solutions generated by the IRS itself. However, optimisation is a very specific field in its own right, and it is not considered in this thesis. Nevertheless it is a critical component in the IRS design.

The IRS can acquire new data and information about the terrain or environment as and when it becomes available. Inevitably, this data will be corrupted by impairments caused by various sources including sensors, the environment, storage devices, communication channels and equipment. A truly intelligent sensor should be able to analyse the data to identify the presence of any impairments and apply mitigation strategies to improve the quality of the data for further processing. The IRS should contain a knowledge base of all relevant types of impairments and appropriate techniques for mitigating each of them. Accurate prediction of clutter map data relies on up-to-date remote sensing data about the current state of the environment and is necessary for the sensor to adapt to changes occurring within the environment. The environment is dynamic in that trees are cut down, buildings are erected, and land surface and crops change with seasonal variations. All these factors influence the accuracy of clutter map prediction, requiring up-to-date data about the environment. With the recent advances in web technologies and net-centric approaches which permit sensor communication and data sharing, this approach for clutter modelling which relies on up-to-date information is now feasible.

For the purpose of this thesis it is necessary to focus on certain aspects of the IRS with the most important components of this model being the radar model, terrain model, multipath model and clutter model. The architecture can then be further simplified as shown in Figure 2.2.

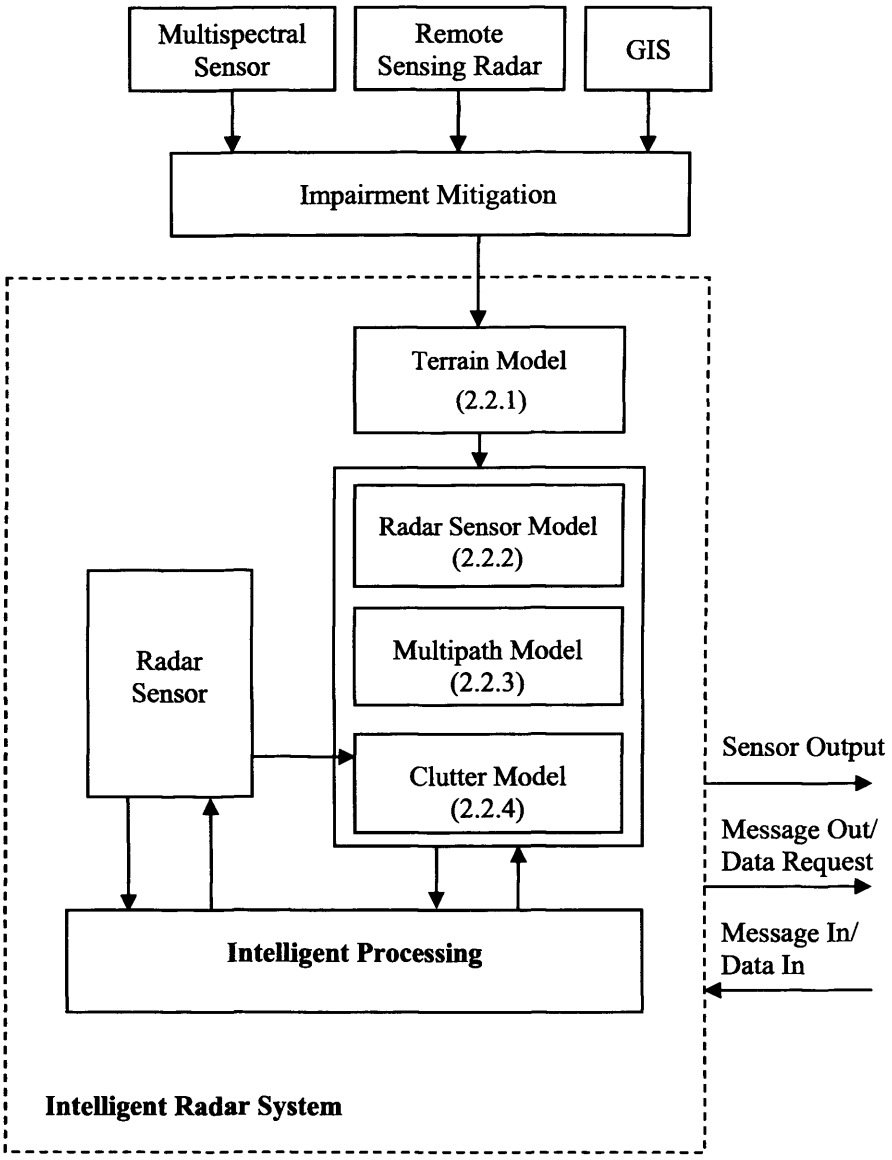

Figure 2.2 Simplified Intelligent Radar Sensor Architecture

Figure 2.2 is similar to Figure 2.1, except that now the details of the intelligent processing block have been suppressed to concentrate on the specific aspects of the intelligent radar sensor that are addressed in this thesis. In particular, the cognitive aspect of the Intelligent Radar Sensor is addressed and the ability of the radar to process information about its environment is investigated. For the remainder of this thesis this simplified architecture for Intelligent Radar Sensor is assumed. The internal models are now discussed; the terrain model is discussed in Section 2.2.1, the radar sensor model in Section 2.2.2, the multipath model in Section 2.2.3, and the clutter model in Section 2.2.4. A description of the software for the intelligent radar sensor

approach described here can be found in Appendix 3, and the software implementation can be found on the Digital Versatile Disc (DVD) included in Appendix 4.

2.2.1 Terrain Model

Information about the terrain provided by other sensors and sources is contained in the terrain model, including but not limited to, digital elevation model (DEM), optical, topographic, SAR, SLAR, and terrain classification data. Terrain classification data refers to information about the type of land surface, such as roads, trees, water and grass. Terrain information can be provided by databases or can be inferred by classification of remote sensing data including optical images, SAR/SLAR and multispectral data. Classification of the data into terrain types can be achieved using techniques based on radial basis neural networks (RBNN) and support vector machines (SVM) developed in [45]. The intensities of radar signal returns are highly sensitive to the relief of the surface and therefore offer efficient representation of land shapes and the topography of the surface being monitored [46]. Optical sensors are not affected by land clutter and multipath propagation effects but are sensitive to other environmental factors such as fog, rain and cloud cover, and an illumination source is required for sensor operation, all of which limit the performance of the sensor [47]. Clearly, each source of data offers an alternative perspective on the environment: DEM provides elevation profiles; remote sensing radar provides direct radar cross section (RCS) measurements of the land surface; and terrain classification data provide information about the land surface type. Therefore, the more types of data we have available the more can be deduced about the environment.

DEM data are required for calculation of radar local grazing angles, target grazing angle, and terrain shadowing effects based on EM wave propagation modelling, all of which are required for sensor error assessment and for site-specific clutter modelling as discussed in Chapter 5. For prediction of multipath radiowave propagation which is discussed in detail in Chapter 4, information about terrain slope is provided by DEM; whilst surface type can be determined by classification of topographic and optical remote sensing data, required for predicting the intensity of the reflected multipath

signals. Remote sensing radar data provides direct radar measurements of the environment but for different grazing angles, and possibly different polarisation or frequency compared with the low-grazing surface-sited radar. Remote sensing data and data fusion techniques can be employed to predict clutter for ground-based radar operating at low-grazing angles.

2.2.2 Radar Sensor Model

The central idea behind the IRS is that if we can model the sensor and factors that affect the operation of the sensor, then we can predict sensor performance for a given scenario and use this information to improve sensor performance. For the IRS we need to model the radar sensor and the environment, in particular, land clutter. Another important influence on radar performance is multipath fading caused by specular reflections from the Earth's surface due to scattering of the EM signal emitted from the radar and reflected back by the target. In order to accurately predict radar performance it is necessary to model all aspects of radar operation and environmental interferences including land clutter, multipath propagation interferences, and clutter attenuation due to terrain topography.

Application of this approach to radar modelling can also be useful for benchmarking new radar systems during the development stages and can provide a suitable tool for assisting in efficient radar system design. In [48] Skolnik identifies the importance of the radar equation and probability of detection, discussing how they can provide valuable tools for the following three applications:

(a) Prediction and assessment of radar performance
(b) Radar system design and assessment of system trade-offs
(c) Assisting in development of the technical requirements for new radar systems

The importance of the radar model and probability of detection for case (a) is the basis of the intelligent sensor in this thesis, highlighting the advantages of the modelling approach for predicting performance (a) and optimising radar system parameters (b).

2.2.3 Multipath Model

It is important to predict multipath effects because they result in fluctuations in the received signal power due to constructive and destructive interference at the receiver. This interference will either increase or decrease the received signal power, increasing or decreasing the radar detection range. Therefore, to accurately predict radar performance multipath effects must be considered. Modelling multipath propagation effects requires modification of the free-space assumption to account for reflections from the land surface, in addition to direct reflections from the target.

In order to model multipath effects detailed information about the Earth's surface is required; height, slope, moisture, and roughness can be obtained from high resolution remote sensing data; while land surface type can be determined from remote sensing data or geographical databases, as discussed in Section 2.3.1. Multipath propagation of radiowaves is considered in detail in Chapter 4.

2.2.4 Clutter Model

For radars operating at low grazing angles signal returns from ground clutter severely impair the performance of the radar and its ability to detect targets. To predict these impairments for the particular scenario the clutter model is computed using the land clutter prediction method proposed in Chapter 5, by fusion of remote sensing data and application of land backscattering models. This approach provides the opportunity for prediction of radar performance for any position within the operation region, provided suitable information about the environment is available.

The advantage of this approach for optimal sensor deployment and sensor placement has already been discussed in Chapter 1. However, if we can incorporate this knowledge within the radar sensor then we can introduce a degree of intelligence and promote intelligent behaviour for the radar sensor. Predicting clutter in advance is an advantage for mobile radar sensing platforms. It can provide the opportunity for optimisation of sensor performance through intelligent selection of sensor position within the environment. Examples of mobile radar which can benefit from such an

approach are land-based, ship-based and airborne radars all of which have the ability to change position in order to improve current sensor performance or move to another location to meet new goals and objectives. Another application is a network of mobile radar sensors in which they all need to cooperate and perform joint optimisation to achieve a common goal.

2.3 Summary

The concept of an intelligent radar sensor is "in the air" at present and is currently receiving significant attention from the radar research community, as discussed in Chapter 1. However, this thesis adopts a fusion-based approach which is an alternative approach compared to those discussed in Chapter 1. An intelligent radar sensor concept has been developed where the innovation lies in application of a modelling approach, which is based on incorporation of sensor and environment models for prediction of sensor performance. For radar sensors operating at low-grazing angles land clutter causes significant impact on the operation of the sensor. Application of a radar model to the clutter map data permits prediction of sensor operation and performance, while intelligent processing of this information provides the opportunity for self-optimisation of sensor operation to improve the performance of the radar sensor.

For application of the IRS, we consider three scenarios: (a) a mobile radar capable of changing its position in order to improve radar sensor performance, or moving to another location to observe a region of the territory that is not visible from the original radar position; (b) radar sensor deployment; (c) and a radar sensor network.

The radar model and target detection are discussed in detail in Chapter 3. Multipath propagation is discussed in Chapter 4. Clutter modelling is addressed in Chapter 5, in which mitigation of SAR remote sensing impairments are also considered. Applications for IRS are considered in Chapter 6.

Chapter 3

Radar Modelling in the Context of an Intelligent Radar Sensor

This chapter identifies the collection of elements required to understand the radar model and its operation within the intelligent radar sensor. The components of the radar sensor model and its role within the intelligent radar sensor are discussed in the context of predicting radar sensor performance and accounting for environmental interference. Nothing in this and the following chapter are new, but it is necessary to present the material in order to properly explain the research reported in Chapters 5 and 6.

3.1 Prediction of Radar Sensor Performance

Radar system performance can be evaluated by the following criteria:

- Maximum detection range
- Ability to resolve multiple targets – this depends on radar resolution and target ambiguity
- Ability to detect targets and reject unwanted interference
- Accuracy of measured target position

These criteria are the most important factors for assessing radar performance; however, the performance of radar for these criteria can not be determined by radar sensor characteristics alone. The performance of a radar depends strongly on the environment in which it is deployed; therefore, to predict radar sensor performance environmental factors must also be considered.

This chapter considers a model of a single-pulse radar where sensor performance is evaluated based on probability of detecting targets. The important components of the radar sensor model are identified, and the implications of environmental interference are considered. Degradation of radar sensor performance is discussed in Section 3.2. All components of the radar model are described in Section 3.3, including the standard radar equation, radar geometry, target detection, and radar model parameters. A discussion on the application of the radar model within the intelligent radar sensor to predict radar sensor performance is detailed in Section 3.4. Conclusions are drawn in Section 3.5.

3.2 Factors which Affect Radar Performance

The emitted radar signals are propagated through the atmosphere and are therefore affected by atmospheric conditions such as rain, snow, fog, atmospheric absorption, refraction and ducting. Additionally, the radar signals are subject to interference from noise produced by natural sources such as the Sun and galactic noise, and from EM interference from radio or power masts, other sensors and even intentionally generated interference (jamming). The radar is also subject to internal system impairments due to equipment noise, equipment errors, and distortion introduced by signal processing.

The target area illuminated by the radar antenna pattern will return signals from the target of interest and other objects in the target background, such as buildings, trees, and the terrain. These unwanted signal returns received by the radar from objects other than the target are referred to as clutter. Clutter impairs the ability of the radar to detect signals of interest (targets) because the received signals from the targets are often smaller than the signals returned by clutter. Additionally, the antenna pattern of the radar also compounds the problem of multipath effects especially at low-grazing angles. It is not only the main beam (central lobe) of the antenna pattern that is of concern, but the presence of sidelobes also affects radar performance.

One aspect of radar performance is the probability of the radar detecting a target. An efficient radar will maintain a high probability of detection and a low probability of

false alarms. The detection of targets is determined by radar characteristics, but detection performance is degraded by natural and artificial interference, both accidental and intentional. All these contribute to deterioration of radar performance and all must be taken into account in predicting radar performance. Although there are other measures of radar performance such as, weight, size, cost, power consumption, and others; it was determined that the most appropriate measure of performance for the scenarios considered in this thesis, in which target detection is of primary importance, is the probability of detection measure. The radar model is now discussed in detail in Section 3.3.

3.3 Radar Sensor Modelling

The main components of the radar model considered in this thesis are shown in Figure 3.1, together with the section within which the component is discussed.

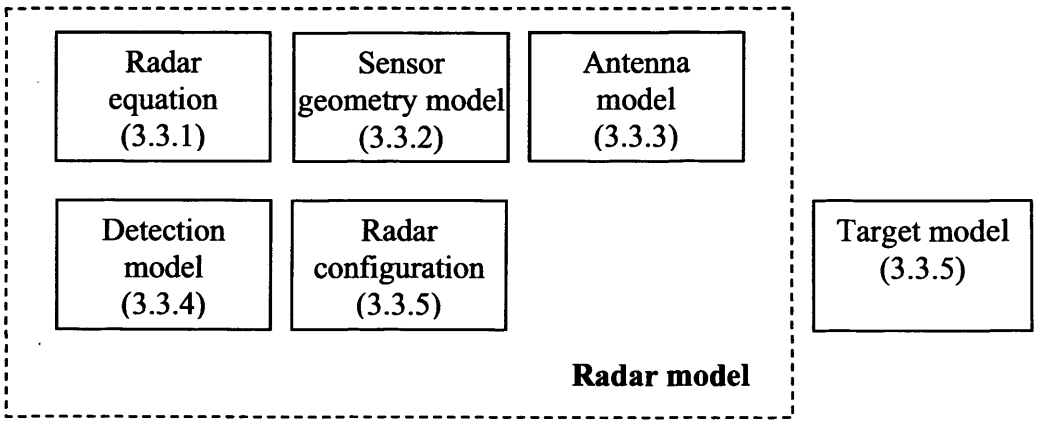

Figure 3.1 Components of the radar model.

The radar equation, discussed in Section 3.3.1, is used to determine the received signal power from both target and clutter returns, and calculate signal-to-noise ratio (SNR) and clutter-to-noise ratio (CNR) respectively. Radar sensor geometry is discussed in Section 3.3.2. The antenna model, discussed in Section 3.3.3, accounts for antenna pattern characteristics including gain, antenna pattern sidelobes, antenna azimuth and elevation beamwidths. The detection model, discussed in Section 3.3.4, describes the detection stage of the radar receiver and ultimately describes the

performance of the radar under the conditions considered. The detection model describes the detection law which can be modelled by Marcum's Q-function for a constant RCS target model [49], or Swerling's models for fluctuating targets [48]. Additionally, there is an allowance for atmospheric refraction, which contributes to bias error in measured target elevation angle. The four-thirds Earth radius model is based on the valid assumption that for low-grazing angles the refractive index is almost constant [50]. Radar configuration parameters are discussed in Section 3.3.5. The radar configuration contains information about the characteristics of the radar sensor, including but not limited to, radar operating frequency, waveform, radar resolution and range limits, antenna pattern, transmit and receive gains, radar position, height, and orientation. The target model also discussed in Section 3.3.5, includes information about the characteristics of targets, including position, height, radar cross section (RCS) and target type. It is now necessary to discuss the radar equation which is an integral component of the radar model.

3.3.1 Radar Equation

The relationship between the characteristics of the radar, the target, transmitted and the received signal can be described by the radar equation. The radar equation required for calculating received power from a point target when a single antenna is used for both transmit and receive can be defined as

$$SNR = \frac{P_t G^2 \lambda^2 \sigma_t}{(4\pi)^3 k T_e B F_n L R^4} F^4 \qquad (3.1)$$

where P_t is peak transmitted power in W, G is antenna gain and accounts for when the target is not at beam maximum, λ is radar wavelength in metres, σ_t is target RCS in m^2, k is Boltzmann's constant in J/deg, T_e is the effective noise temperature in $^\circ K$, B is receiver bandwidth in Hz, and R is range in metres. F_n is the noise figure which represents SNR losses due to thermal noise in the radar amplifier. F^4 is the fourth-power propagation factor and can be used to account for propagation losses and gains such as atmospheric absorption and diffraction losses. In this thesis, however, F^4 only

concerns multipath effects. Atmospheric losses are not directly modelled but are accounted for in the loss factor L which can be defined as

$$L = L_t L_\alpha L_p L_x \tag{3.2}$$

Here L_t is transmission loss, L_α is atmospheric loss, L_p is antenna pattern beamshape loss, and L_x is signal processing loss. $L_\alpha = 10^{0.1 k_\alpha R}$, where k_α is the attenuation coefficient in dB/km [50].

The target usually occupies a small fraction of the area illuminated by the radar beam and therefore can be hard to detect. The clutter-to-noise ratio (CNR) is defined by [51]

$$CNR = \frac{P_t G^2 \lambda^2 \sigma_c}{(4\pi)^3 k T_e B F_n L R^4} F^4 \tag{3.3}$$

where the cross section for clutter σ_c is the product of the reflectivity σ^0 and the illuminated area A_c as follows

$$\sigma_c = \sigma^0 A_c \tag{3.4}$$

A simple constant γ model [13] can be applied in which surface reflectivity is modelled as $\sigma^0 = \gamma \sin\psi$, where σ^0 is reflectivity (cross section per unit area m^2/m^2), ψ is grazing angle in radians, and γ is a dimensionless parameter describing the scattering effectiveness of the surface. However, this model is limited because here σ^0 is only a function of grazing angle and does not account for surface type or roughness. In this thesis σ^0 is determined by the clutter model described in Chapter 5.

The signal-to-clutter-plus-noise ratio (SCNR), also known as signal-to-interference ratio (SIR), is defined by [51]

$$SCNR = \frac{1}{\frac{1}{SNR} + \frac{1}{SCR}} \tag{3.5}$$

where the Signal-to-Clutter ratio (SCR) is obtained by dividing Equation (3.1) by Equation (3.3).

To calculate the cross section for clutter σ_c it is necessary to first calculate the illuminated area A_c, which can be achieved by considering radar sensor geometry as discussed now in Section 3.3.2.

3.3.2 Sensor Geometry

The geometry for the calculation of clutter area A_c is shown in Figure 3.2 which is a reproduction of the illustration in [51]. Here h_r is radar height, h_t is target height in degrees, θ_t is target elevation angle in radians, θ_r is the clutter region depression angle in radians, R is slant range in km, R_g is ground range in km, ΔR is range resolution, ΔR_g is the ground projection of ΔR, and θ_E and θ_A are the antenna 3-dB elevation and azimuth beamwidths in degrees, respectively. The area for mainbeam clutter, A_{MBc}, and area for sidelobe clutter, A_{SLc}, can be calculated as follows

$$A_{MBc} = \Delta R_g R_g \theta_A \tag{3.6}$$

$$A_{SLc} = \Delta R_g \pi R_g \tag{3.7}$$

The main beam clutter RCS and sidelobe clutter RCS can then be defined as

$$\sigma_{MBc} = \sigma^0 A_{MBc} G^2(\theta_t + \theta_c) \tag{3.8}$$

$$\sigma_{SLc} = \sigma^0 A_{SLc} (SL_{rms})^2 \tag{3.9}$$

where G is antenna gain and SL_{rms} is the root-mean-square (rms) value of the antenna sidelobe levels. Then σ_c can be defined as

$$\sigma_c = \sigma_{MBc} + \sigma_{SLc} \tag{3.10}$$

As can be seen in (3.8) and (3.9) in order to calculate the cross section for clutter σ_c we need to account for antenna pattern gain. Antenna pattern characteristics are now considered in Section 3.3.3.

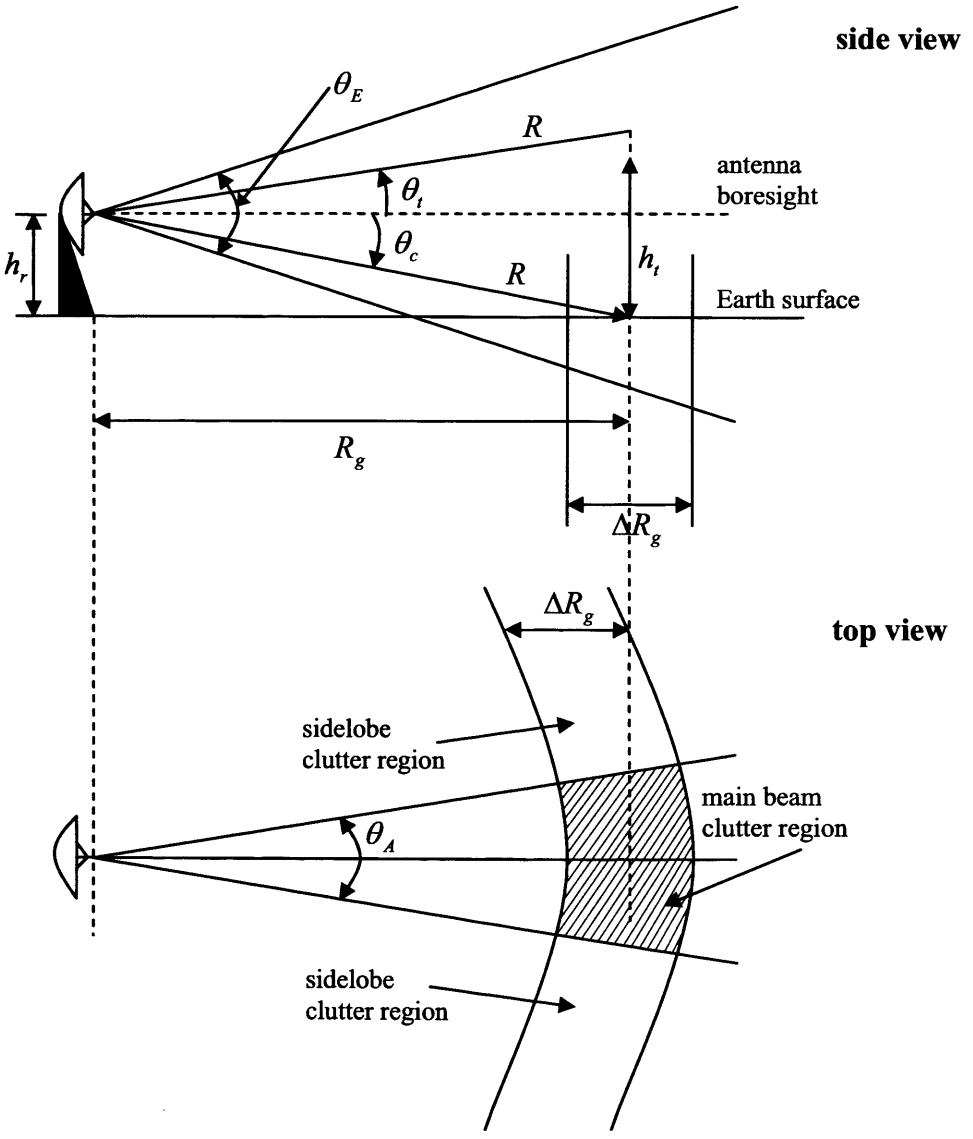

Figure 3.2 Clutter geometry (taken from [51])

3.3.3 Radar Antenna Pattern

Antenna gain G can be described by the following relationship.

$$G = \frac{4\pi A_e}{\lambda^2} \tag{3.11}$$

where $A_e = \upsilon A$, and υ is aperture efficiency ($0 \leq \upsilon \leq 1$). Gain can also be expressed in terms of antenna elevation and azimuth beamwidth as follows

$$G = k\frac{4\pi}{\theta_E \theta_A} \tag{3.12}$$

where θ_E is elevation beamwidth in radians, θ_A is azimuth beamwidth, and $k \leq 1$ is a shape factor depending on the geometry of the physical aperture.

A Gaussian antenna pattern is assumed, which although unrealistic has been selected to keep this intelligent radar sensor approach generic. The Gaussian antenna main lobe can be defined as [51]

$$G(\theta) = \exp\left(-\frac{2.776\theta^2}{\theta_E^2}\right) \tag{3.13}$$

The antenna pattern has a constant sidelobe level at -35dB. This Gaussian antenna pattern in dB is shown in Figure 3.3(a) in polar form and Figure 3.3(b) in rectangular form. The elevation beamwidth in this case is $\theta_E = 11°$, and is shown later in Table 3.1 on page 43. The azimuth beamwidth is much smaller, 1.33 , and this is shown in Figure 3.3.

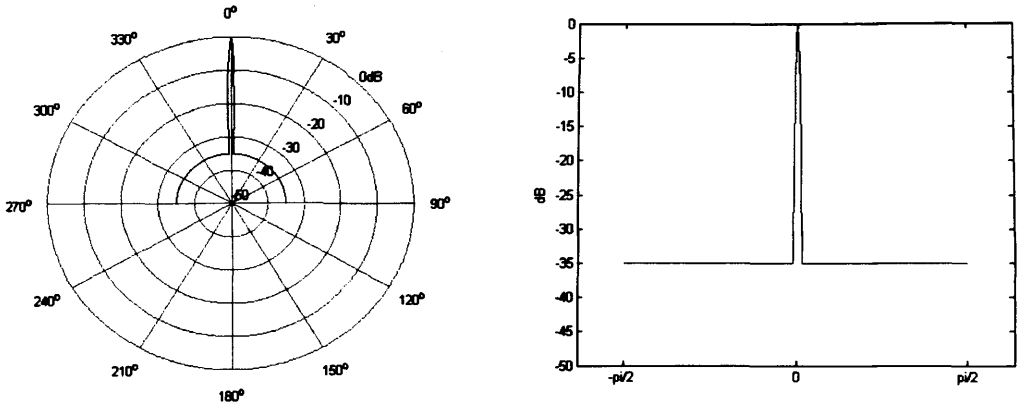

(a) (b)

Figure 3.3 Gaussian antenna patterns in:
(a) polar form; (b) rectangular form.

In order to halve the computation for convolution the range of the side lobe pattern was truncated to $\pm\pi/2$. Now that we can calculate the SNR, CNR, and SCNR we must next consider the detection process which determines the ability of the radar to detect targets. This is discussed in detail in Section 3.3.4.

3.3.4 Target Detection Modelling

The detection of targets in radar is based on threshold detection, where a threshold is established at the output of the receiver. A target is determined to be present if the receiver output exceeds the threshold; otherwise it is assumed that only noise is present in the received signal. Random fluctuations in the received signal due to noise (radar thermal noise) and interference (from the environment and other RF sources) can have significant impact on detection [48]. If the received noise and interference signals are sufficiently high then the threshold may be exceeded in the absence of a target. This is known as a false alarm. Setting a higher threshold reduces the probability of false alarms (P_{fa}), but at the expense of a lower probability of detection (P_d), where signals returned from weak targets may not be high enough to exceed the threshold. The challenge therefore is to maximise P_d whilst minimising P_{fa}. Various techniques exist for doing this, including adaptive threshold constant false alarm rate (CFAR) [50].

The process of threshold detection is shown in Figure 3.4 for a simplified system consisting of an envelope detector and threshold detector, and is taken from [51].

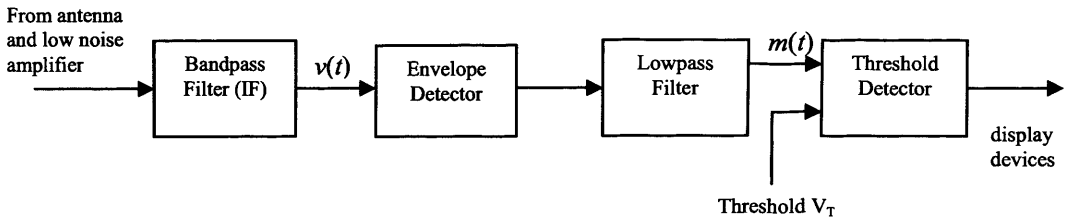

Figure 3.4 Simplified envelope detector and threshold receiver

The receiver input signal is composed of the radar echo signal $s(t)$ and additive white Gaussian noise $n(t)$ with variance ψ^2, where it is assumed that the input noise is uncorrelated with the signal.

The signal $v(t)$ is the output of the bandpass IF filter and can be written as

$$v(t) = v_I(t)\cos\omega_0 t + v_Q(t)\sin\omega_0 t = m(t)\cos\left(\omega_0 t - \varphi(t)\right)$$

$$v_I = m(t)\cos\varphi(t)$$

$$v_Q = m(t)\sin\varphi(t) \qquad (3.14)$$

Here v_I and v_Q are the in-phase and quadrature components, $m(t)$ is the envelope of $v(t)$, the phase is $\varphi(t) = \tan^{-1}(v_Q / v_I)$, and $\omega_0 = 2\pi f_0$, where f_0 is the radar operating frequency.

A target is determined to be present when $m(t)$ exceeds the threshold V_T. The decision scheme is:

$s(t) + n(t) > V_T$ Detection

$n(t) > V_T$ False alarm

The Marcum Q-Function is an established method for predicting the probability of detection for non-fluctuating targets in pulsed radar [49]. Swerling extended this model for probability of detecting targets with fluctuating RCS [48]. For the purposes of this thesis we consider Marcum's constant RCS model which can easily be substituted for application of the Swerling models. It is necessary now to discuss the particulars of probability of false alarm and probability of detection.

Probability of False Alarm

The probability of false alarm P_{fa} is the probability that a sample M of $m(t)$ will exceed the threshold voltage V_T when only noise is present in the radar signal [48]. This is

$$P_{fa} = \int_{V_T}^{\infty} \frac{m^2}{\Psi^2} \exp\left(-\frac{m^2}{2\Psi^2}\right) dr = \exp\left(-\frac{V_T^2}{2\Psi^2}\right) \tag{3.15}$$

Inverting this relationship gives the voltage threshold V_T as

$$V_T = \sqrt{2\Psi^2 \ln\left(\frac{1}{P_{fa}}\right)} \tag{3.16}$$

The probability of false alarm can be expressed in terms of false alarm time T_{fa}, which is the time between false alarms. This is then defined as

$$T_{fa} = \frac{t_{\text{int}}}{P_{fa}} \tag{3.17}$$

where t_{int} is the radar integration time. Given that the radar operating bandwidth B is the inverse of t_{int}, then substituting (3.16) into (3.17) T_{fa} can be rewritten as

$$T_{fa} = \frac{1}{B}\exp\left(\frac{V_T^2}{2\Psi^2}\right) \tag{3.18}$$

It can be seen that T_{fa} can be reduced by increasing the threshold V_T, however this results in decreasing the maximum detection range. We can now address probability of detection.

Probability of Detection

The probability of detection P_d is the probability that a sample M of $m(t)$ will exceed the threshold voltage V_T when noise plus signal is present in the radar signal, defined as [51]

$$P_d = \int_{V_T}^{\infty} \frac{m}{\Psi^2} I_0\left(\frac{mA}{\Psi^2}\right)\exp\left(-\frac{m^2 + A^2}{2\Psi^2}\right)dr \tag{3.19}$$

where A is amplitude and I_0 is the modified Bessel function of order zero. The integrand is the probability density function (pdf) of a Rician distribution, which becomes the Raleigh pdf when $A/\Psi^2 = 0$. When A/Ψ^2 is very large it becomes the Gaussian pdf with mean A and variance Ψ^2. Assuming the input at the receiver is a sinusoidal signal with amplitude A and power $A^2/2$, then for a single pulse $SNR = A^2/2\Psi^2$ and $V_T^2/2\Psi^2 = \ln(1/P_{fa})$, and Equation (3.19) can be written as [51]

$$P_d = \int_{\sqrt{2\Psi^2 \ln(1/P_{fa})}}^{\infty} \frac{m}{\Psi^2} I_0\left(\frac{mA}{\Psi^2}\right)\exp\left(-\frac{m^2 + A^2}{2\Psi^2}\right)dr = Q\left[\sqrt{\frac{A^2}{\Psi^2}}, \sqrt{2\ln\left(\frac{1}{P_{fa}}\right)}\right] \tag{3.20}$$

where $$Q[\alpha,\beta]=\int_{\beta}^{\infty}\zeta I_0(\alpha\zeta)e^{-(\zeta^2+\alpha^2)/2}d\zeta \tag{3.21}$$

Here Q is Marcum's Q-Function. The Marcum Q-Function is a definite integral whose integrand involves a modified Bessel function, and no analytical solution exists. Many good approximations for the Marcum Q-Function have been proposed in the literature [52, 53]. A very accurate approximation proposed in [54] is

$$P_d \approx 0.5\times \text{erfc}\left(\sqrt{-\ln P_{fa}} - \sqrt{SNR+0.5}\right) \tag{3.22}$$

where the complementary error function erfc(·) is defined as

$$\text{erfc}(z)=1-\frac{2}{\sqrt{\pi}}\int_0^z e^{-v^2}dv \tag{3.23}$$

We have now developed the radar model required for the intelligent radar. The parameters required for the radar model are detailed in section 3.3.5.

3.3.5 Radar Model Parameters

The parameters in the radar configuration component of the radar model are shown in Table 3.1. The values for these parameters are representative of typical X-band radar and therefore are not an implementation of a specific radar system. Radar position, antenna orientation, and antenna pattern characteristics are also accounted for but are not listed in Table 3.1.

The target model is not an internal component of the radar model but it is included in this chapter as it is the most natural place to discuss this component. The target model for a fighter jet with 6dBsm RCS is shown in Table 3.2.

Table 3.1 Radar Model Parameters

Symbol	Parameter	Value
P_t	peak transmitted power	75 kw
τ	pulse width	0.1 μsecs
G	antenna gain	34.5 dB
T_e	effective noise temperature	290 °K
λ	Wavelength	3.75 cm
f_o	radar operating frequency	8 GHz
F	noise figure	5 dB
B	receiver bandwidth	6 MHz
L	radar losses	6 dB
θ_E	elevation 3dB angle (degrees)	11°
θ_A	azimuth 3dB angle (degrees)	1.33°
$R_{\min}$	minimum detection range	500 m
$R_{\max}$	maximum detection range	12 km
k	Boltzmann's constant	1.38×10^{-23} J/°K
E_R	Earth's radius	6378 km
P_{fa}	probability of false alarm	9.25×10^{-11}
h_r	height of radar	25 m

Table 3.2 Constant RCS Target Model

Symbol	Parameter	Value
σ_t	target RCS	6 dBsm
h_t	target height	250 m

This is a constant RCS model which does not account for RCS fluctuations due to complex target shapes with multiple scatterers or changes in target orientation with respect to radar position and aspect angle. However, this model can be modified to account for more complex target types. The models in Tables 3.1 and 3.2 are

implemented for the scenarios considered in Chapter 6. We will now discuss how all these components for the radar model can be applied to predict radar performance.

3.4 Radar Model Operation within the Intelligent Radar Sensor

The processes and models involved in predicting radar sensor performance are shown in Figure 3.5.

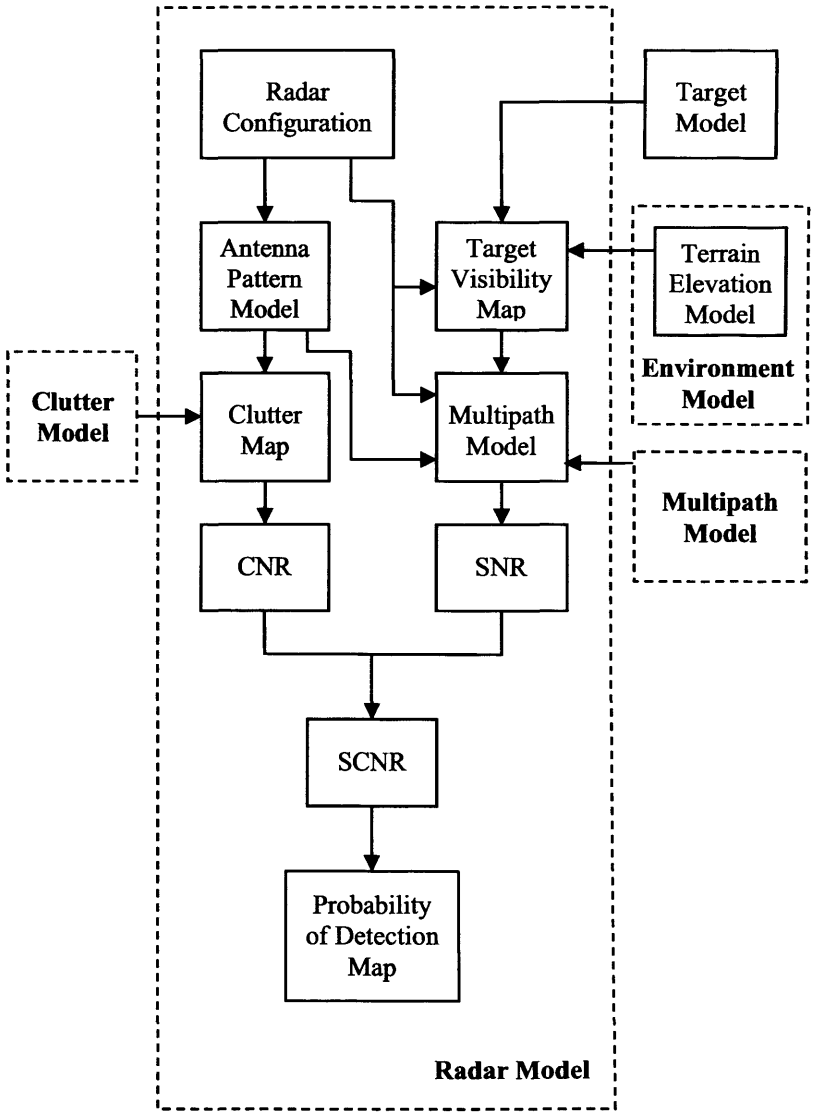

Figure 3.5 Radar model application and operation

The radar configuration describes radar characteristics and properties required for application of the radar equation. The radar configuration provides antenna

characteristics which enables the antenna pattern model to be constructed. The target model, radar position and terrain elevation data are required for calculating the target visibility map which depicts whether the target is visible from the radar position or obscured by terrain shadowing. To determine multipath effects, information about the radar position, antenna pattern, polarisation, target position, target visibility map are required in addition to terrain elevation data and surface type. The SNR can then be calculated by application of Equation (3.1) as shown in Figure 3.6(a).

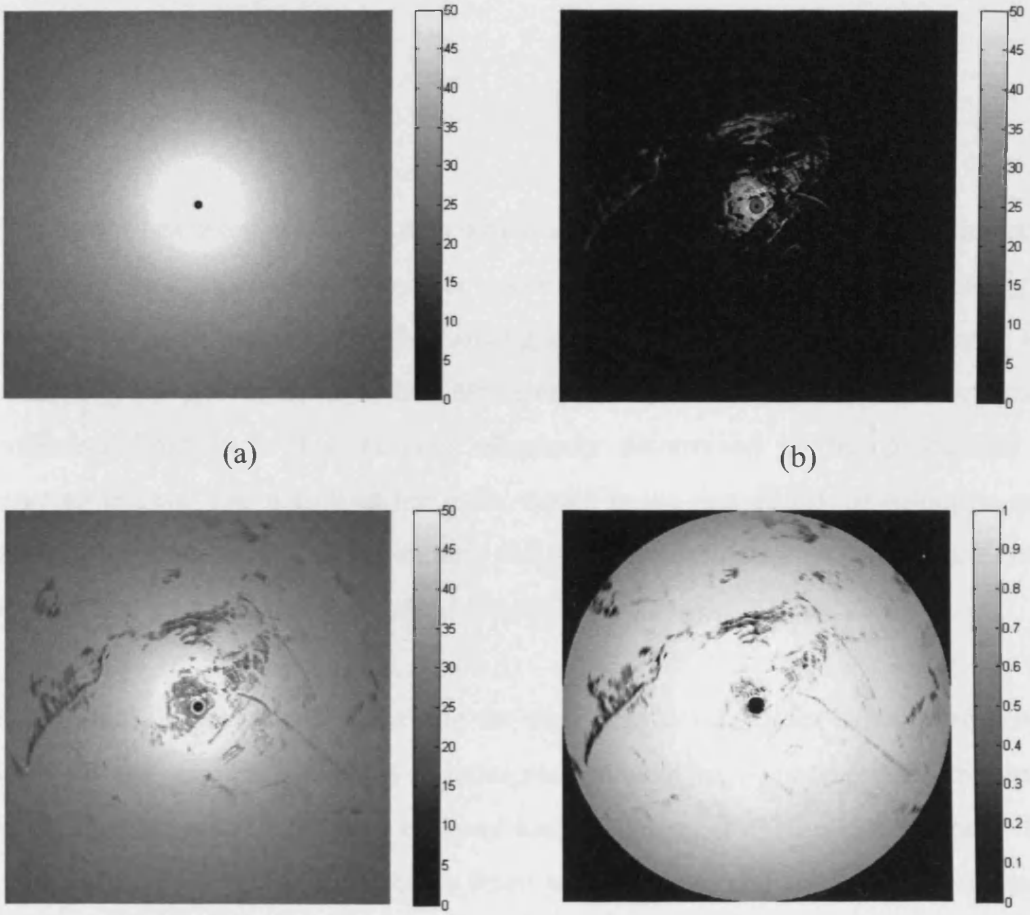

Figure 3.6 Performance measures:
(a) SNR in dB; (b) CNR in dB; (c) SCNR in dB;
(d) Probability of Detection Map (without multipath effects).

The antenna pattern model is applied to the predicted clutter map produced by the clutter model to account for antenna pattern effects. The CNR can then be calculated by application of Equation (3.3) as shown in Figure 3.6(b). The ability of the radar to

detect target signals in interference determined by SCNR Equation (3.5) as shown in Figure 3.6(c), is used by the detection model Equation (3.22) to predict probability of detection map as shown in Figure 3.6(d) which in this case does not account for multipath effects. Multipath effects will be discussed in Chapter 4 and will be accounted for in the three scenarios in Chapter 6. The probability of detection map describes probability of the radar detecting a target accounting for radar characteristics and environmental factors. The probability of detection map is accordingly, an important measure for radar performance.

3.5 Summary

This chapter has discussed the factors which affect radar performance in the detection of targets. The components of the radar sensor model and its role within the intelligent radar sensor have been discussed, showing how modelling of the radar sensor and accounting for the environmental interferences can be utilised to predict radar performance, which in this thesis is ultimately determined by the probability of detecting targets. The output of the radar model is the probability of detection map which in this case illustrates the radar's ability to detect the target while accounting for multipath propagation effects, land clutter, and radar parameters.

The material in this chapter leads into the next chapters. In order to apply the radar model for site-specific prediction of radar performance we need to predict multipath propagation effects and account for land backscattering from the local terrain. The multipath model is now considered in detail in Chapter 4, and the land clutter model discussed in Chapter 5.

Chapter 4

Modelling Multipath Radiowave Propagation

In this chapter, after a review of radiowave propagation modelling, the components required for multipath modelling are discussed. It is necessary to model multipath propagation to account for the increase or decrease in radar target detection due to the constructive and destructive interference which this phenomenon causes. The geometry for multipath surface reflections is considered in Section 4.3, the multipath propagation factor F is discussed in Section 4.4, and surface characteristics which determine the intensity of the reflected signal are considered in Section 4.5.

4.1 Multipath Modelling

When a radar signal is intercepted by an object the signal is scattered in various directions. How the signal is scattered is determined by the wavelength of the radar signal, polarisation of the signal, incidence angle, and underlying surface. The roughness of the surface determines whether the signal is specular or diffusely scattered. Only specular reflections contribute to multipath propagation effects. The wavelength of the signal is also an important factor in specular reflections due to the relative dimensions of surface roughness and wavelength. Additionally, surface type affects signal backscattering, depending on the dielectric constant of the material and also on wavelength of the signal. The wavelength of the signal is important as it determines the penetration properties of the radiowaves, allowing the signals of certain frequencies to penetrate through trees, vegetation and even soil. In general, short wavelengths will produce backscattering from the overlying vegetation such as leaves, twigs and branches; while long wavelengths will penetrate the overlying vegetation to produce backscattering from tree trunks and soil [55].

Modelling multipath effects entails modification of the free-space assumption to account for the reflection of waves from the surface in addition to the direct path

signal [50]. Multipath occurs when the signal propagates to the object and returns to the radar receiver via more than one path. This results in a set of received signals with different amplitudes and different phases. The problem with this is that the receiver will sum the received signals and, depending on the phase differences, this could lead to either an increase or decrease in the magnitude of the vector sum of the received signals. A single multipath reflection is shown in Figure 4.1.

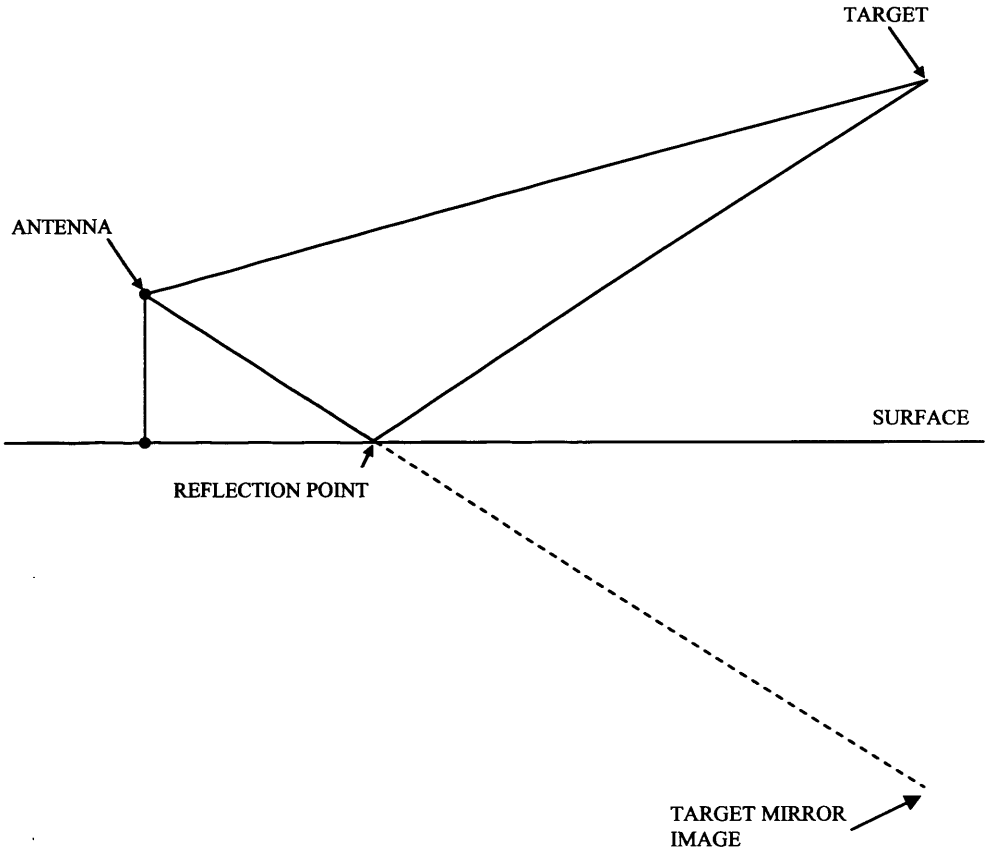

Figure 4.1 Multipath reflection

An additional effect of multipath reflection is that the reflection from the surface appears to the radar as an image below the surface (mirror image), which leads to errors in the estimation of target height.

In Section 4.2 we will now consider multipath effects and discuss various methods applicable for modelling them.

4.2 Review of Multipath Propagation Modelling

Environmental factors such as atmospheric conditions and terrain features affect radiowave propagation causing refraction, diffraction and reflection; resulting in attenuation of the radiowave energy. For low-grazing radar, the most important non-free-space effect is multipath fading which results in constructive and destructive interference at the receiver. Multipath fading effects are due to interference between the direct and ground reflected signals; and strongly depend on the geometry of the terrain and terrain type. Multipath effects cause interference lobes in radar coverage with the shape and position of the lobes and nulls determined by surface characteristics. These lobes and nulls are due to the phase difference of the reflected multipath signal and depending on whether the signal is in or out of phase with directly reflected signal, results in either an increase or decrease in target detection range. It is important to predict the electromagnetic fields due to the effect of the environment on radiowave propagation, to account for the fluctuations in signal power at the receiver as a result of multipath effects. To model multipath surface reflections we need detailed information about the characteristics of Earth's surface such as height, slope, surface roughness and surface type. Terrain elevation data can be obtained from a variety of sources such as stereo imaging satellites, or SAR interferometers; or constructed from topographic contour lines. Terrain type can be determined through geographical databases such as MODIS and GLC2000 [56], or can be extracted from topographic map data.

There are generally three approaches to modelling radiowave propagation effects; parabolic equations (PE), wave theory which uses physical optics (PO), and ray tracing methods also known as geometric optics (GO) [57]. Solutions to the Partial Differential Equations (PDE) arising from Maxwell's equations [58] can be obtained by PE which comprises one approach to modelling radiowave propagation. PE are particularly useful for modelling changes in the refractive index of the atmosphere. They have difficulty, however, in dealing with rough surfaces. PE were first proposed for radiowave propagation in 1946 [59], but limited processing power of computers in 1946 restricted practical application. Developments in the sonar community led to the split step solution (SSS) which uses the FFT to advance the solution over small range steps and allowed application of PE [60]. The radar community then adopted PE for

prediction of tropospheric propagation [61], propagation over irregular terrain [62], and tropospheric ducting and multipath fading over irregular terrain [63].

The PO approach uses EM wave theory to study the reflection and propagation of waves accounting for diffraction and propagation loss, while GO makes the assumption of short wavelengths in order to simplify the reflection problem. Geometric models are approximations of physical models and are only suitable when the wavelength is relatively small compared with surface roughness. However, GO does not account for variations in the refractive index of the atmosphere to predict the effects of ducting and the resulting enhanced range detection. Hybrid methods have been developed to combine the advantages of PE which works well for low angles and ray optics which works well for higher angles [64].

In this thesis, modelling of radiowave propagation is restricted to multipath effects and tropospheric effects. For modelling tropospheric effects the four-thirds Earth radius model for standard atmospheric conditions is used. Ray tracing methods are only applicable for the interference region and are not valid for modelling pattern propagation factors in the diffraction region [65]; however, multipath effects do not occur in the diffraction region. For modelling propagation factors when the target is in the diffraction region methods based on EM wave theory such as Maxwell's equations provide a relatively simple solution [58]. As we are only concerned with modelling multipath effects in this thesis, the approach taken is based on ray tracing using a GO approach which allows relatively simple calculation of radar geometry parameters, and the interference propagation factor for predicting multipath interference. The geometry for surface reflections is now considered in Section 4.3.

4.3 Surface Reflection Geometry

Radar sensor and surface reflection geometry are shown in Figure 4.2, which is a modification of the illustration in [66].

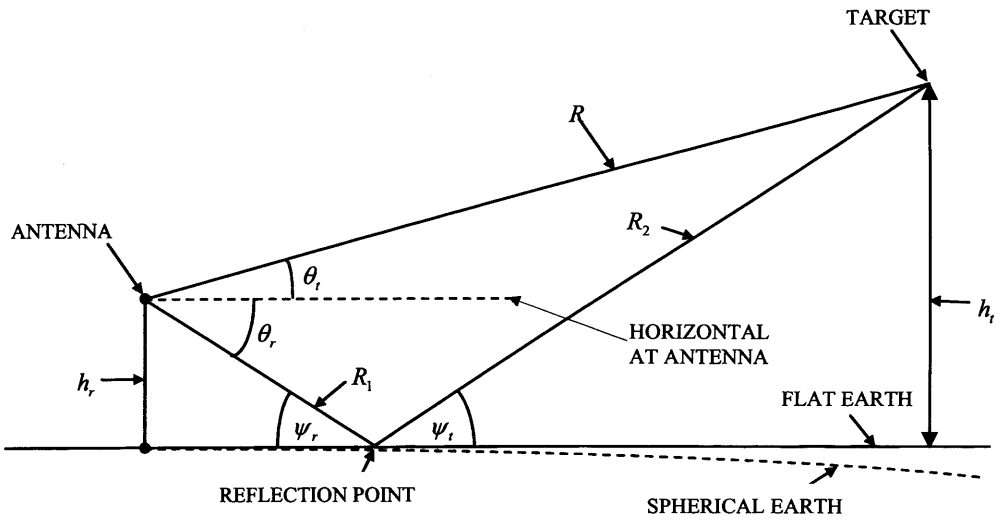

Figure 4.2 Radar geometry with multipath

Here h_r is radar height in metres, h_t is target height in metres, θ_t is target elevation angle in radians, θ_r is the reflection point depression angle in radians. A two-path multipath is shown where R is the direct pathlength, R_1 and R_2 are the reflected pathlengths, ψ_r is the radar grazing angle in radians and ψ_t the target grazing angle in radians. Specular reflection occurs when $\psi_r \approx \psi_t$. It can be shown that [50]

Target elevation $$\theta_t = \sin^{-1}\left(\frac{h_t - h_r}{R}\right) \approx \frac{h_t - h_r}{R} \tag{4.1}$$

Grazing angle $$\psi = \sin^{-1}\left(\frac{h_t + h_r}{R}\right) \approx \frac{h_t + h_r}{R} \tag{4.2}$$

Pathlength difference $$\delta_0 = R\left(\frac{\cos\theta}{\cos\psi}\right) \approx \frac{2h_r h_t}{R} \tag{4.3}$$

Range to reflection point $$x_0 = \frac{h_r}{\tan\psi} = \frac{Rh_r}{h_r + h_t} \tag{4.4}$$

These equations provide the parameters required to calculate the propagation factor, which is discussed now in Section 4.4. However, these equations do not account for

the terrain local slope in 3D; therefore, in this thesis the parameters required for calculating the propagation factor are determined using 3D Digital Terrain Elevation Data (DTED). This approach is extremely computationally expensive, but is necessary to provide a more accurate and realistic multipath model.

4.4 Propagation Factor

The pattern propagation factor F can be described [66] as

> "*the magnitude of the ratio of the electric-field strength at that point to the field strength that would exist at the same range in free space* and *in the antenna beam maximum.*"

It follows that

$$F = \left| \frac{E}{E_0} \right| \tag{4.5}$$

where E is the electric field intensity of the received signal over the path of interest, and E_0 is the free-space field intensity. The fourth-power propagation factor F^4 describes the two-way power ratio with the inverse square law operating on both the forward and return paths. As discussed in Section 1.5 page 18, only a two-path model is considered. The general formula for two-path interference pattern propagation factor is [50]

$$F_i = \left| f(\theta_t) + f(-\psi)\rho D \exp(-j\alpha) \right| \tag{4.6}$$

Here $f(\cdot)$ is the antenna pattern factor, θ_t is the target elevation, ψ is grazing angle, ρ is the magnitude of the surface reflection coefficient, D is the divergence factor to account for a spherical Earth, and α is the phase difference between the direct and reflected waves, given by [50]

$$\alpha = \frac{2\pi\delta_0}{\lambda} + \phi \tag{4.7}$$

where δ_0 is the extra pathlength for the reflected wave, and ϕ is the phase angle of the reflection coefficient. As will be seen later, ϕ can be assumed to be $-180°$ for small grazing angles. The interference region corresponds to $\delta_0 > \lambda/6$. To model propagation effects without considering a specific antenna pattern the following formula can be applied [50]

$$F = \sqrt{1 + \rho^2 + 2\rho\cos\left(\frac{2\pi\delta_o}{\lambda} + \phi\right)} \tag{4.8}$$

where ρ is the surface reflection coefficient which we will now discuss in section 4.5.

4.5 Surface Reflection Coefficient

The surface reflection coefficient accounts for the influence of the land surface on the reflected signal, and is usually considered as the product of three factors:

$$\rho = \rho_0 \rho_s \rho_v \tag{4.9}$$

Here ρ_0 is the Fresnel reflection coefficient (the fraction of the intensity of the incident ray that is specularly reflected from the perfectly smooth surface), ρ_s is the specular scattering coefficient to account for surface roughness, and ρ_v is the vegetation absorption coefficient. The reflection coefficient is complex valued and for horizontal polarisation can be written as [50]

$$\Gamma_h = \rho_0 \exp(-j\phi) = \frac{\sin\psi - \sqrt{\varepsilon_c - \cos^2\psi}}{\sin\psi + \sqrt{\varepsilon_c - \cos^2\psi}} \tag{4.10}$$

where ε_c is the complex dielectric constant, $\varepsilon_c = \varepsilon_r - j60\lambda\sigma_e$ [50, 67, 68], ε_r is the relative dielectric constant and σ_e is the conductivity of the surface material. Similarly, the reflection coefficient for vertical polarisation can be written as [50]

$$\Gamma_v = \rho_0 \exp(-j\phi) = \frac{\varepsilon_c \sin\psi - \sqrt{\varepsilon_c - \cos^2\psi}}{\varepsilon_c \sin\psi + \sqrt{\varepsilon_c - \cos^2\psi}} \qquad (4.11)$$

Typical values for ε_r and σ_e are given in Table 4.1 [50].

Table 4.1 Electrical Properties of Typical Surface Types

Surface type	ε_r	σ_e
Good soil (wet)	25	0.02
Average soil	15	0.005
Poor soil (dry)	3	0.001
Snow, ice	3	0.001
Fresh water (λ=1m)	81	0.7
Fresh water (λ=0.03m)	65	15
Salt water (λ=1m)	75	5
Salt water (λ=0.03m)	60	15

For low grazing angles for both polarisations the phase angle is near 180°. However, there is a sudden change in phase near the Brewster angle ψ_B (the angle of incidence at which the ray can not be reflected) for vertical polarisation as defined by Equation (4.12), where angles greater than ψ_B have a phase close to zero [50].

$$\psi_B = \sin^{-1}\frac{1}{\sqrt{\varepsilon_r - 1}} \qquad (4.12)$$

Table 4.1 does not consider all terrain types, therefore, the assumption $\rho_0 = -1$ and $\phi = -180^o$ is valid for small grazing angles where $\psi < 2^o$ for water and $\psi < 10^o$ for other surface types [50]. It is now necessary to determine the surface roughness to calculate the specular scattering coefficient ρ_s and vegetation absorption coefficient ρ_v.

4.5.1 Specular Scattering Coefficient and Vegetation Absorption Coefficient

The specular scattering coefficient ρ_s is a function of surface roughness σ_h, wavelength and grazing angle defined as [50].

$$\rho_s = \exp\left[-\frac{1}{2}\left(\frac{4\pi\sigma_h}{\lambda}\sin\psi\right)^2\right] \tag{4.13}$$

Typical values for σ_h and ρ_v are shown in Table 4.2 for various surface types [69].

Table 4.2 Surface Roughness and Vegetation Factor

Surface type	σ_h	ρ_v
Concrete	0.5-2	1
Arable land	10-15	1
Snow	0.5-10	1
Coniferous forest	>100	0
Deciduous forest	>100	0
Grass < 0.5m	10-20	0.8-0.5
Grass > 0.5m	10-30	0.5-0.1
Urban	>300	0
Water (as concrete)	0.5-2	1

Finally, we must address the impact of a spherical Earth on the geometry of radiowave propagation; this is discussed in section 4.6.

4.6 Accounting for Spherical Earth and Terrain Local Slopes

The effect of a spherical Earth leads to bias in height estimation of both target and the Earth surface. This effect and terrain local slopes influence the grazing angle and therefore need to be considered. In Figure 4.2 the dip of the spherical Earth below the surface tangent can be calculated by [50].

$$\delta_h = ka\left(\sqrt{1+\left(\frac{G}{E_E}\right)^2}-1\right)\approx\frac{G^2}{2E_E} \tag{4.14}$$

where E_E is four-thirds the Earth radius and G is ground range. To model the dip of the Earth surface it is necessary to reduce the terrain elevation height by δ_h.

The local slope of the terrain must also be accounted for when calculating grazing angles as shown in Figure 4.3.

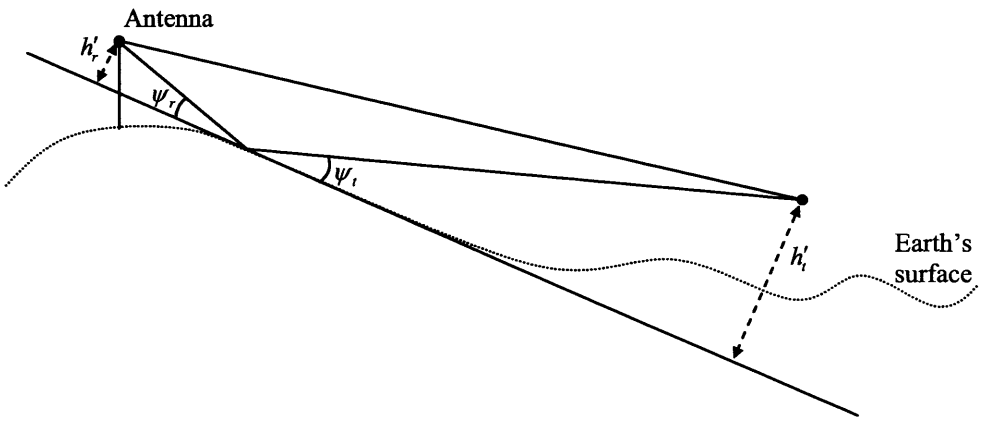

Figure 4.3 Geometry of specular reflection accounting for local slope tangent

Here ψ_r is radar grazing angle, ψ_t is target grazing angle, h'_r is radar height with respect to the tangent specular point, and h'_t is target height with respect to the tangent. The following condition determines whether the reflection is specular: $\psi_r \approx \psi_t$, where $|\psi_r - \psi_t| < \varsigma$ and $\varsigma = 0.03^o$ is the threshold. The pathlength difference can then be defined as [50].

$$\delta_0 = \frac{2h'_r h'_t}{G} \tag{4.15}$$

The results for multipath modelling using measured data are presented in Section 4.7.

4.7 Site-specific Modelling of Multipath Propagation and Discussion

The data required for predicting multipath propagation effects are terrain elevation data and terrain type data. The terrain elevation data is required for calculating local grazing angles and in our experiments it is provided by SAR interferometer measurements obtained by the Spaceborne Imaging Radar (SIR-C) sensor [70]. Land surface type is required for determining the intensity of the multipath reflected signal and is provided by RBFC classification [45] into appropriate terrain classes of the multispectral data obtained by the Landsat TM Mapper sensor [71]. Classification using the RBFC is considered in detail in Chapter 5.

The processes involved in predicting multipath effects and determining the propagation factor F are shown in Figure 4.4.

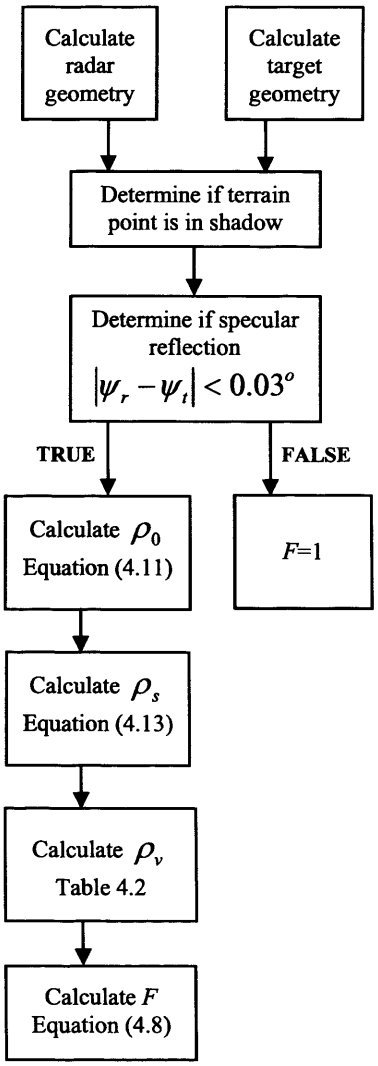

Figure 4.4 Process for calculating propagation factor F

The parameters for the radar and the target are taken from Table 3.1 and Table 3.2, respectively. The first stage is to calculate radar and target geometry parameters, including the specular reflection point (if one exists), grazing angle of the specular point for both the radar and the target, and the pathlength difference of the multipath signal. If it is determined that no specular point exists, $|\psi_r - \psi_t| > 0.03°$, then the propagation factor F equals unity (0dB), and multipath interference is absent for the considered surface position. If $|\psi_r - \psi_t| < 0.03°$, then multipath interference is present and the propagation factor F is calculated using Equation (4.8). In order to calculate F it is necessary to first calculate the surface reflection coefficient which is the product of the Fresnel reflection coefficient ρ_0 given by Equation (4.11), specular scattering coefficient ρ_s given by Equation (4.13), and the vegetation absorption coefficient ρ_v obtained from Table 4.2.

An example of propagation factor F experimental calculation for the considered radar coverage region is shown in Figure 4.5.

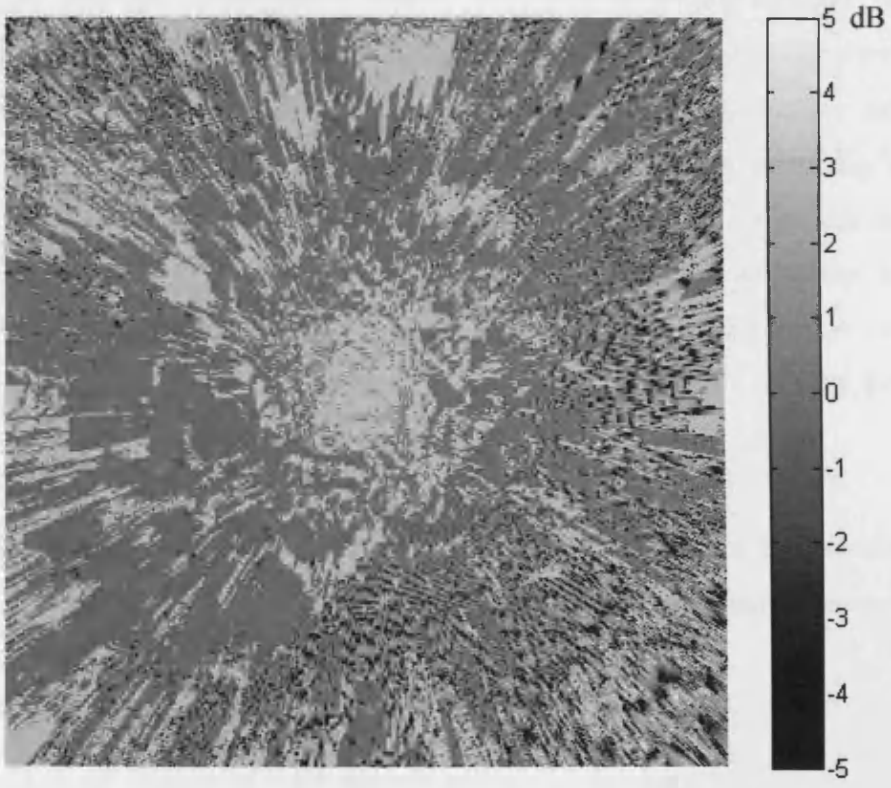

Figure 4.5 Propagation factor F

We have discussed the multipath model for the intelligent radar sensor, identifying the remote sensing data sources and propagation modelling techniques required for predicting the intensity of multipath interferences. This multipath model can now be applied to Equation (3.1) to allow the intelligent radar sensor to predict radar performance, while accounting for fluctuations in the received signal power due to multipath surface reflections.

4.8 Conclusions

In this chapter we have reviewed standard approaches for predicting multipath propagation effects and identified the most appropriate approach for modelling these effects for the purposes of this thesis. The influence on target detection due to the constructive and destructive interference caused by multipath effects have been considered, highlighting the importance of modelling multipath propagation when predicting radar performance. The components required for modelling multipath propagation effects have been discussed in sufficient detail including radar and target geometry, the propagation factor F, and the dependency of the reflected signal intensity on the characteristics of the land surface. The land surface characteristics which have the most significant influence on multipath propagation are surface roughness and terrain type. Surface roughness influences specular scattering while terrain type determines signal reflectivity and absorption. Surface roughness can be estimated using remote sensing data which provides information about the terrain elevation, such as SAR interferometer measurements. Land surface type can be obtained through geographical databases, extracted from topographic data, or through classification of remote sensing multispectral data.

We will now consider the impact of land surface clutter on radar performance in Chapter 5, in which a new method for predicting of land clutter intensity is proposed.

Chapter 5

Land Clutter Modelling for Radar Operating at Low-Grazing Angles

In this chapter, after a review of land clutter modelling methods, a new approach for predicting land clutter intensity for surface-sited low-grazing angle radar is presented. Fusion of remote sensing data and application of a land backscattering model provides the basis for site-specific prediction of up-to-date land clutter models. The methodology of this approach is described identifying the necessary remote sensing data required for land clutter modelling, and the method of data fusion. Results are then presented using measured remote sensing data.

5.1 Review of Standard Methods for Clutter modelling

Land clutter presents significant problems for low-angle radar in the detection of targets, primarily because signal returns from land surface clutter are generally stronger than returns from targets. Low-altitude or terrain-following targets can be masked by clutter and hidden or shadowed by terrain features making detection extremely difficult [72]. In strong clutter environments poor performance is attained for detection of weak targets [73].

Land clutter dynamically changes over time due to varying environmental conditions, and strongly depends on terrain and environmental parameters, such as terrain slope, terrain type, surface roughness, and moisture [73]. Site specific clutter modelling provides the opportunity for developing tools for testing and developing radar in realistic simulated environments prior to deployment, and for optimising radar parameters [13]. Characterisation of clutter and terrain modelling also provide the opportunity for optimisation of radar parameters.

Clutter prediction is an important task to be solved because clutter degrades radar performance. There are many practical uses for clutter modelling such as planning of sensor deployment and Constant False Alarm Rate (CFAR). With respect to sensor deployment, prediction of clutter and multipath propagation for a region will provide the opportunity for placement of radar sensors to provide optimal coverage of the region and minimisation of the impact of clutter. For moving radar applications this information can be utilised to continuously predict clutter maps for the next positions on the moving radar path and therefore allow dynamic route calculation to provide maximum radar coverage whilst the radar is moving between positions. Also, the information provided by clutter maps can be used as an effective tool for mission planning applications [72] to determine the best route for an aircraft to avoid detection by enemy radar and ensure maximum survivability by masking the aircraft in clutter to remain undetected. In addition to clutter map data, multipath effects must also be considered when predicting radar performance, as discussed in Chapter 4.

Land clutter is a function of radar frequency, polarisation, grazing angle, terrain type, and terrain elevation [73]. Experimental results of clutter modelling [73] have shown that radar resolution changes the clutter amplitude distribution spread but the clutter mean level of the distribution remains unaffected. There are typically two approaches for modelling land clutter, generalised and site-specific. Generalised models usually take the statistical approach aiming to identify the underlying trends of clutter intensity for basic terrain types. Site-specific approaches must consider clutter and terrain visibility, both of which depend critically on terrain topography.

Statistical models serve well for general clutter models providing realistic clutter maps, but do not account for site-specific characteristics of the radar environment due to the local terrain. Statistical modelling methods have been applied for site-specific clutter modelling by application of GIS data to provide information about the environment. The site-specific approach in [13] uses DTED for estimation of local grazing angle and terrain shadowing effects. Additionally, direct measurements of atmospheric temperature, pressure and humidity are used to create refractivity profiles to account for electromagnetic wave propagation. This approach combined with Parabolic Equations [59-64] and GO [57] have shown to provide high accuracy clutter maps, however, a relatively simple constant-gamma model has been used for

estimation of land surface reflectivity which does not account for terrain type or the relief of the terrain. As discussed, land clutter intensity changes with terrain type and terrain local slope which produces terrain shadowing effects, and therefore it is important to account for these factors.

This limitation has been addressed in [74] by application of the MIT Lincoln Laboratory empirical clutter models [73] to estimate land surface reflectivity based on terrain surface type, showing improved accuracy of clutter modelling. Digital Feature Analysis Data (DFAD) and DTED have been utilised to estimate land surface parameters in order to apply the relevant clutter model based on terrain characteristics. In this case DFAD provides information about dominant scatterers which contributes to strong reflectivity such as buildings, radio masts and power transmission masts. This approach has been adopted in [75] in combination with flying obstacle register data which provides information on radio masts and other high objects, for knowledge-aided analysis of the impact of clutter on the performance of air surveillance radar.

Clutter temporal and spatial variability due to geographical features and man-made sources surrounding the radar reinforce the need for site-specific land clutter models over more general statistical approaches. To date, site-specific approaches use GIS data which may be out-of-date and therefore do not reflect the current state of environmental conditions; and more importantly do not account for direct measurements of clutter which can be provided by remote sensing radar. Remote sensing radar is an important source of information as it provides direct measurements of normalised RCS but for alternative grazing angles. Generally, grazing angles are much higher for remote sensing radar compared with land-based low-grazing angle radar, and this difference in grazing angle accounts for the difference between the clutter maps for remote sensing and land-based radar. The remainder of this chapter investigates the opportunity for fusing radar remote sensing data, information about terrain characteristics, and application of empirical land backscattering models for land clutter prediction.

5.2 Input Data for Clutter Modelling

The most important parameters for clutter modelling are radar frequency, polarisation, grazing angle, terrain type, and terrain elevation. Site-specific clutter modelling requires information about the land surface and the use of additional information about the land surface has been shown to improve the accuracy of clutter map prediction [74]. Remote sensing imaging data can provide valuable information about the terrain and can supplement terrain classification [45], and estimation of bare soil parameters such as roughness and moisture [76]. SAR and SLAR images describe electromagnetic wave backscattering from the Earth's surface, where the image pixel brightness represents the intensity of the backscattering coefficient σ^0. It has been demonstrated [73] that measurements of clutter for ground-based and airborne radars at adjacent grazing angles are highly correlated, illustrating the suitability of SAR/SLAR remote sensing data for aiding site-specific clutter map prediction. When considering the surface reflectivity dependence on grazing angle for remote sensing radar, the grazing angle is in the plateau region resulting in a relatively weak angular dependence on the land backscattering coefficient due to diffuse scattering of electromagnetic waves. Surface-sited surveillance radar for detection of low altitude targets usually operate in the near-grazing region where clutter returns are generally produced by a small number of strong isolated scatterers [66].

In order to apply remote sensing radar data for prediction of clutter maps it is important to account for the difference in backscattering mechanisms for land-based and airborne radar by considering the following factors:

- Dependency of the backscattering coefficient on grazing angle and land surface type.
- Dependency of the backscattering coefficient on radar frequency and polarisation.
- Local slope of the land surface.
- Terrain shadowing effects due to terrain elevation.
- Height and position of antenna for land-based and remote sensing radars.
- Electromagnetic wave propagation in the troposphere.

The land backscattering model can be applied to account for these factors. Application of the land backscattering model also permits correction of angular dependencies and estimation of the difference in the backscattering coefficient for land-based and remote sensing radars. The remote sensing data required for clutter modelling are shown in Figure 5.1.

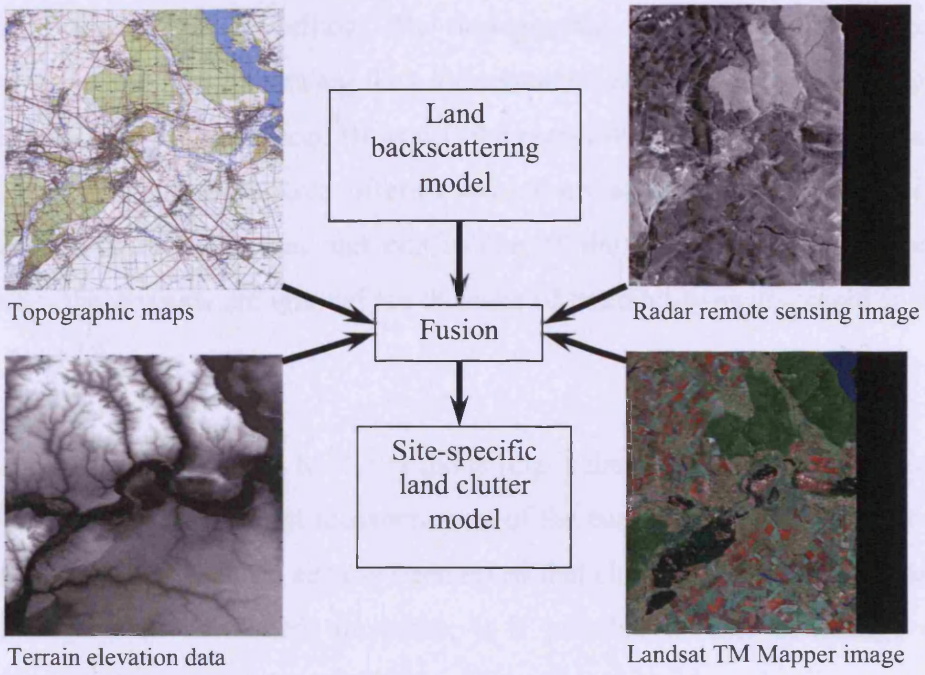

Figure 5.1 Fusion of remote sensing images and topographic data.

This data is for a region near Kharkov in the Ukraine and was used for clutter modelling experiments. The topographic map scale is 1:100000 and the radar image pixel resolution is about 12m. The terrain elevation data has 90m pixel resolution and 1m elevation resolution. Terrain elevation data is required for estimation of local grazing angles to account for changes in clutter intensity with change of grazing angle, and also for calculation of the terrain visibility map to estimate visible clutter regions. Terrain elevation data can be provided by stereo satellite images, reconstructed from topographic contour lines [77], or produced by spaceborne SAR interferometers [78]. For the purpose of clutter modelling in this thesis, Spaceborne Imaging Radar (SIR-C) terrain elevation data is used to provide up-to-date measurements and because it can operate in complicated weather conditions, such as cloud, rain, and at night. It can also provide measurements of the backscattering coefficient for the land surface and can be obtained from [70].

Information about the terrain type can be extracted from the topographic map; however, this could be out-of-date due to changes in the environment. A more convenient method is classification of multispectral remote sensing images or using information provided by global land cover maps such as MODIS and GLC2000 [56]. We use direct classification of multispectral Landsat TM Mapper images because it provides the opportunity for deciding appropriate terrain classes and features most applicable for clutter modelling. The topographic map is used for geometric registration of the remote sensing data to a common coordinate system and also for supporting terrain classification. However, the registration process is problematic due to the fact that data sources have differing resolutions, additive quantisation noise, and uncertainties in the precision and confidence of the data. With the exception of resolution, these issues are ignored for the sake of tractability as discussed in Section 1.5 on page 18.

The novelty of this approach to clutter modelling is the application of remote sensing radar images to provide direct measurements of the backscattering coefficient for the radar coverage region. It has already been noted that clutter measurements at adjacent grazing angles are correlated; therefore, it is possible to take advantage of this correlation to improve clutter modelling. The remote sensing radar images must be preprocessed to remove the influence of radar system imperfections such as speckle, geometric distortions, and radiometric calibration on the measured data. Radiometric calibration of the remote sensing radar image is necessary to convert the signal intensities into absolute RCS values. Additionally, impairments in the data need to be reduced to minimise the effects on clutter modelling. Analysis of the SLAR data has shown that only speckle noise is present; but should any other impairment be present then they should be mitigated prior to further processing. SAR impairment mitigation and fusion are considered in Sections 5.2.1-5.2.3. Fusion and mitigation of impairments in satellite optical remote sensing imagery to improve terrain classification in the presence of various types of impairments, has been considered in our publication [79]. Here, several different types of image impairments were considered: narrowband high-frequency interferences, sensor noise, and geometric distortions due to communication system synchronisation errors. A two-stage approach was adopted so that standard (unmodified algorithms) can be applied for mitigation and fusion with the advantage of not having to modify the algorithms. At

the first stage impairments were mitigated. A technique based on the mean absolute difference similarity measure was used for correction of communication system synchronisation errors. Narrowband high-frequency interferences were removed by preliminary spectral analysis and frequency-domain adaptive linear filtering techniques. Image mean level correction techniques together with linear and nonlinear adaptive filtering were applied to eliminate periodic variation of image mean intensity. We also used nonlinear adaptive filtering in a sliding window approach to suppress additive and impulsive noise. Then at the second stage, image fusion and classification algorithms based on artificial neural networks and support vector machines were applied to classify the terrain into a limited number of terrain types. The specific details of the fusion and classification algorithms used will be provided later in Section 5.5.3 on page 95.

5.2.1 Fusion of Radar Remote Sensing Data and Mitigation of Impairments

It is preferred now to digress slightly from the topic of clutter modelling in order to discuss the importance of removing any impairments present in remote sensing radar data to improve the accuracy of clutter prediction. This digression is fairly lengthy and we considered moving this discussion to an Appendix, but decided that this was the most appropriate place for this topic; however, a more detailed analysis can be found in Appendix 1 and Appendix 2. The discussion on clutter modelling will then continue in Section 5.3 on page 87.

Information provided by sensors is often incomplete or inaccurate due to sensor imperfections and other contributing factors such as, sensor operating conditions, environmental conditions and errors in the data caused by the medium used to store or transmit the data. By modelling the sensor, communication channel and the errors produced by these sources, suitable mitigation techniques can be developed to mitigate the impairments in the data, prior to fusion [41, 79]. This is the motivation for the approaches applied for fusion and mitigation of radar remote sensing impairments, as discussed in Sections 5.2.2 and 5.2.3. For SAR/SLAR data we are presented with three types of noise impairments. Additive noise due to equipment errors is small and therefore not considered; but we do consider impulse noise caused

by data transmission errors and multiplicative noise (speckle) which is inherent due to the nature of SAR.

Data fusion can help reduce impairments, improve accuracy of measurements and provide enhanced information. Additionally, fusing multiple SAR/SLAR data from different sensor platform trajectories can improve the estimate of backscattering coefficient due to non-isotropic (anisotropic) scatterers within the terrain, such as ploughed troughs in bare soil and rows of planted crops [80]. Therefore, by improving the estimated backscattering coefficient we provide the opportunity to improve prediction of land clutter in environments where non-isotropic scattering is present, such as, ploughed troughs and rows of plated crops. Fusion of SAR/SLAR data can be realised through Multiresolution (MR) approaches.

MR schemes based on image pyramids and the wavelet transform have grown in popularity over the past decade, and have been shown to provide an appropriate tool for fusion of remote sensing data. Fusion of remote sensing image data has been shown to provide advantages for various practical applications including classification [81], target identification [82] and improved object detection [83]. Different source images usually contain both common and complementary information, which can be exploited by appropriate fusion techniques that have been developed to efficiently extract the salient information [84, 85]. A considerable amount of research has been conducted in MR fusion and many comparisons exist between MR image fusion techniques for various applications [85-87]. Additionally, MR signal analysis techniques such as DWT and DTCWT have also shown to be effective tools for image denoising for applications such as edge detection [88], image enhancement [89], improved classification [90] and object detection [91]. A discussion on the filter bank implementations of the DWT and DTCWT can be found in Appendix 5. The Dual Tree Complex Wavelet Transform (DTCWT) [40] has been proposed as an approximate shift invariant alternative and has been shown to offer improved directional selectivity over the DWT [40]. The DTCWT produces six bandpass sub-images with complex coefficients at each level. These bandpass sub-images are strongly oriented at angles of $\pm 15^{\circ}$, $\pm 45^{\circ}$, $\pm 75^{\circ}$. This directional sensitivity results from the complex filters' ability to distinguish negative and positive frequencies both horizontally and vertically. A more complete explanation of DTCWT and the filters

which are suitable for use with DTCWT is given in [40, 92]. Mitigation of transmission errors is considered in Section 5.2.2, and a new multiresolution approach based on DCT for speckle suppression is presented in Section 5.2.3.

5.2.2 Mitigation of Transmission Errors in SAR Data

The work detailed in this section has been published in [41] and is intended only as a summary of the techniques and outcomes of the simulations. A detailed discussion and analysis of the results can be found in Appendix 1. If the data are transmitted from the sensor platform via a communication channel then the data may be corrupted by transmission errors and errors produced by the communication equipment. This form of error modelling applies not only to SAR/SLAR sensors but any remote sensor that transmits the sensor data via a communication channel; however, alternative mitigation techniques may be required for different sensor modalities depending on the nature of the data and on the nature of the errors.

Consider the scenario shown in Figure 5.2 for multi-channel radar image fusion and impairment mitigation. Several radar sensors are installed on a single platform, which could be airborne or spaceborne, with all the sensors monitoring the same region and having different operating configurations to provide additional information content.

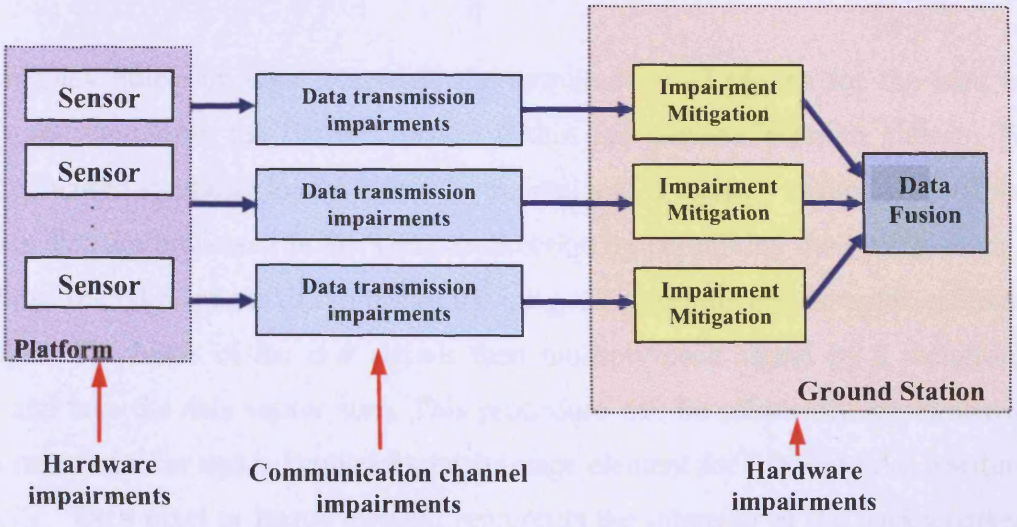

Figure 5.2 Scenario for multi-channel radar image fusion and impairment mitigation

The data acquired by the sensors are then coded and transmitted via a communication channel back to the ground station for processing. During the stages of acquisition and transmission the data are subjected to various impairments which can significantly distort the data and therefore degrade the data fusion process. Sources of these impairments can be attributed to hardware at both the sensor and the ground station, including coding/decoding errors, synchronisation issues and hardware failure. Additionally, the data will contain impairments due to the characteristics of the communication channel used to transmit the data.

For modelling impairments the i.i.d uniform noise model is used; this is the worst case scenario for when there is no *a priori* knowledge of the data transmission channel characteristics. The raw SAR hologram data are corrupted by data transmission errors, then mitigation techniques are applied to remove the impairments at the stage of SAR image synthesis, and finally, unmodified fusion algorithms are implemented to fuse the mitigated images. For mitigation of these impairments the robust non-linear α-trimmed estimate [41] is implemented, which has been shown to provide superior performance for the mitigation of impulse noise in SAR images. Other robust alternatives include the M-estimate which is a Maximum Likelihood estimate based on robust estimation theory, and the Marginal Median estimate, both of which are also detailed in [41] where robustness studies and comparisons are made between all three techniques.

The complex hologram data represents the amplitudes and phases for the sum of signals reflected from the Earths' surface within the antenna azimuth pattern. To achieve focused synthesis for SAR images the real and imaginary components of the complex data are processed in the azimuth direction by combining the returns from a number of spatial positions to synthesise the image. To provide this complex estimate we adjust the phases of the raw signals then multiply each signal by a weighting factor and take the data vector sum. This procedure can be efficiently implemented with a matched filter and is applied for each image element for focused SAR aperture synthesis. Each pixel or image element represents the intensity of the backscattered signal reflected from a point of the Earths' surface.

Assuming that the hologram rows correspond to the azimuth direction, the standard linear algorithm for focused SAR image synthesis can be expressed as follows [93]:

$$J(r,c) = \frac{1}{N} \sum_{n=-N/2}^{N/2} h(r,c+n) \cdot f_w(r,n)^* \ ,$$

$$I(r,c) = \left| J(r,c) \right| \tag{5.1}$$

where the complex amplitude estimates of the reflected signal are denoted by $J(r,c)$, SAR image samples generated by taking the absolute value correspond to $I(r,c)$, and $|\cdot|$ denotes the complex modulus. r and c correspond to row and column indices, N is the length of the synthetic aperture in samples of the SAR hologram data, and $h(r,c)$ are complex samples from the SAR hologram. $f_w(r,n)^* = f(r,n)^* \cdot w(n)$ is the complex conjugate of the point target response function $f(r,n)$, multiplied by a weighting function $w(n)$. The purpose of the weighting function $w(n)$ in Equation (5.1) is to decrease the level of sidelobes of the SAR response [66, 93]. A Hamming window was implemented as the weighting function w for the sake of simplicity.

α-trimmed L-estimate for Robust Mitigation of Data Transmission Errors

The standard linear algorithm for SAR image synthesis [66, 93] is optimal when components of the complex signal are corrupted with Additive White Gaussian Noise (AWGN), however, this is not true when data are coded and transmitted via a communication channel. Under these conditions the matched filter is no longer optimal as the data may also be corrupted by impulse noise which substantially degrades the quality of the synthesised image. To provide estimates of complex parameters that are robust to impulse noise and insensitive to deviations from the Gaussian noise distribution, the α-trimmed estimate [41] is considered. This has been shown to offer improved robustness when estimating complex signals amplitude in the presence of impulse noise. The α-trimmed estimate trims the samples to remove impulses before producing an estimate of the signal. The α parameter can be selected according to the intensity of noise present in the signal allowing for a more robust

estimate. The α parameter can be selected automatically but this is not the place to discuss this. The method is described in Appendix 1 Section 1.2 and will form the topic for a future publication.

Considering the task of robust SAR image synthesis the marginal α-trimmed mean estimate algorithm can be written as

$$\hat{I}(r,c) = \left| \sum_{n=-N/2}^{N/2} a_n [r_s(n) + j \cdot i_s(n)] \right| \tag{5.2}$$

where $\sum_{n=-N/2}^{N/2} a_n = 1$, and $r_s(n)$ and $i_s(n)$ are values of the sets $\{R_s(n), I_s(n), n = -N/2,...,N/2\}$, sorted into ascending order: $r_s(-N/2) \le ... \le r_s(N/2)$, $i_s(-N/2) \le ... \le i_s(N/2)$. Coefficients $R_s(n)$ and $I_s(n)$ are defined as

$$\begin{aligned} R_s(n) &= \mathrm{Re}[h(r,c+n) \cdot f_w^*(r,n)] \\ I_s(n) &= \mathrm{Im}[h(r,c+n) \cdot f_w^*(r,n)] \end{aligned} \tag{5.3}$$

where $n = -N/2,...,N/2$. The coefficients a_n for odd N are calculated as

$$a_n = 1/(N-2T),\ T = \lfloor (1-\alpha)N/2 \rfloor \tag{5.4}$$

when $n \in [\, T - \lfloor N/2 \rfloor, \lfloor N/2 \rfloor - T \,]$ and $a_n = 0$ otherwise. $\lfloor x \rfloor$ denotes the largest integer less than or equal to x. The number of samples of $r_s(n)$ and $i_s(n)$ used for the mean value estimation are determined by the α parameter, while the remaining smallest and largest samples are trimmed. The α parameter in the α-trimmed mean estimate can be varied in the range $0 \le \alpha \le 1$ to tune the robustness and noise suppression properties of the estimate. For $\alpha = 0$ it is straightforward to prove that the estimate (5.3, 5.4) becomes the marginal median, while $\alpha = 1$ results in a mean estimate. The α parameter determines the number of trimmed samples which determines the estimate's ability to eliminate impulse noise.

Mitigation Results

The original horizontally transmitted horizontally received (HH) polarised SAR image without impulse noise impairments is shown in Figure 5.3.

Figure 5.3 SAR image HH polarisation without impairments.

The images in Figure 5.4 demonstrate the effectiveness of α-trimmed estimate in mitigating i.i.d impulse noise for $0.1 \leq P_{imp} \leq 0.5$, where P_{imp} is the probability of occurrence of a full amplitude impulse in the raw hologram data.

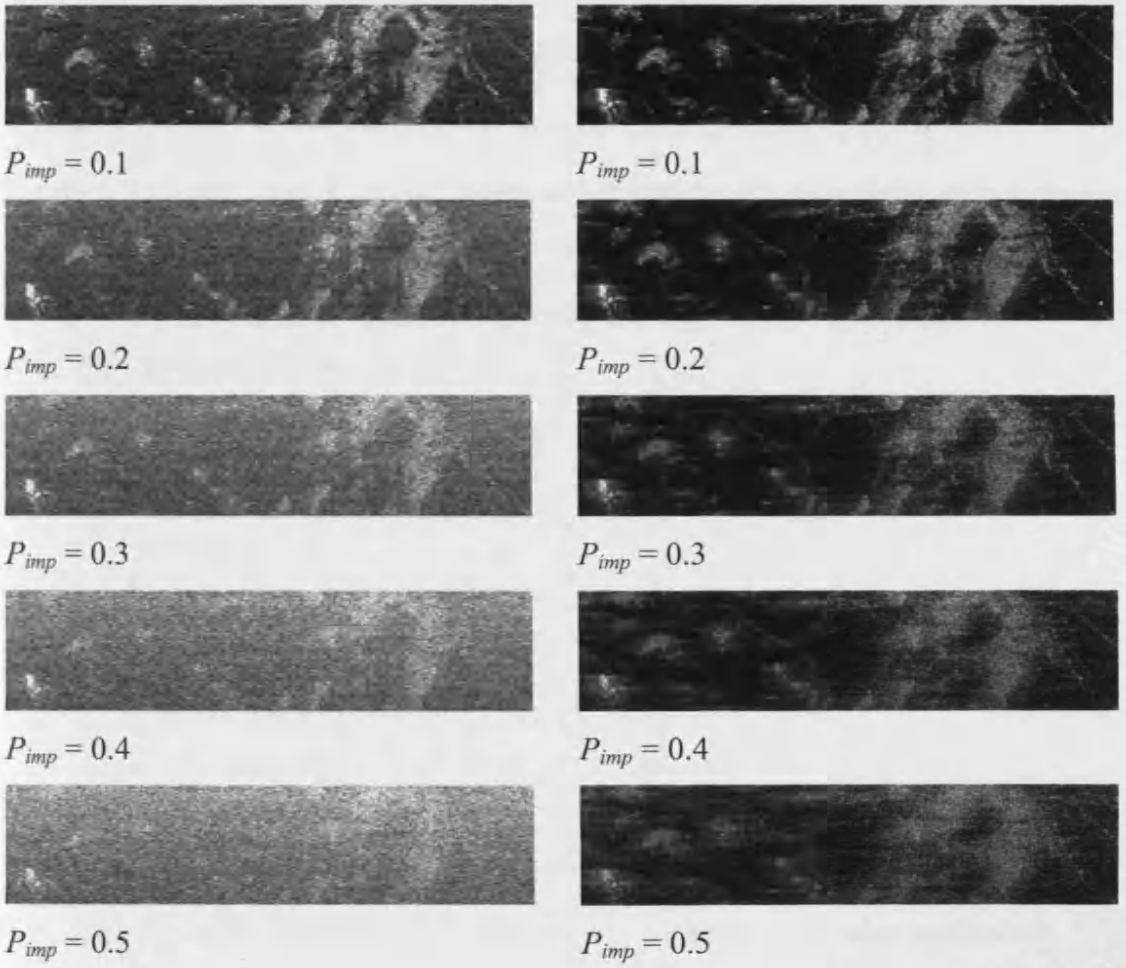

Figure 5.4 α-trimmed mitigation results for impulse noise model.

Visual analysis confirms substantial improvements in image quality of mitigated images for all intensities of impulse noise. Even for SAR images corrupt with high intensities of impulse noise where $P_{imp} \geq 0.3$ some potentially useful information can be recovered using the α-trimmed estimate. Clearly, the α-trimmed estimate offers considerable improvements in image quality. Figure 5.5 illustrates the SNR for mitigation of impulse noise for the considered noise model.

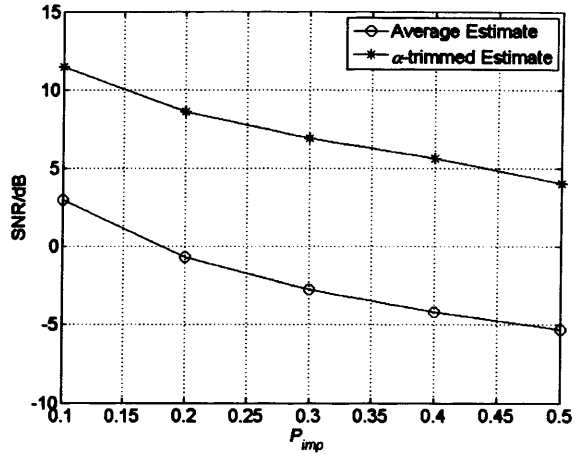

Figure 5.5 SNR for SAR α-trimmed estimate impulse noise mitigation.

Figure 5.5 shows the SNR with and without mitigation of impairments, demonstrating performance gains greater than 8dB. Clearly, the α-trimmed estimate offers considerable improvements in image quality. The MSE shown in Figure 5.6 confirms the same trends as SNR shown in Figure 5.5.

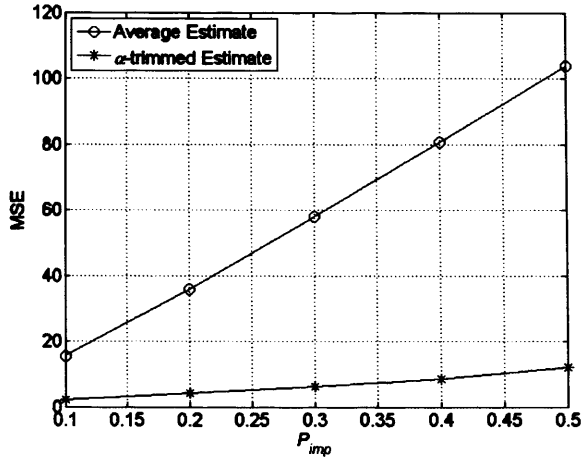

Figure 5.6 MSE for SAR α-trimmed estimate impulse noise mitigation.

The standard linear algorithm given by Equation (5.1) demonstrates complete intolerance to impulse noise as expressed by both SNR and MSE, with high P_{imp} resulting in extreme degradation in performance. However, the average estimate presents superior results in the absence of impulse noise because it is the matched filter in this case. Clearly, the α-trimmed estimate is robust, providing desirable characteristics, efficiently suppressing noise while adequately preserving image content such as bright point objects and edge details.

Mitigation and Fusion of SAR imagery

To assess the impact of impulse noise mitigation on the fusion process, the fusion schemes using DWT and DTCWT to provide MR analysis and Maximum Selection (MS), Weighted Average (WA) and Window Based Verification (WBV) [94] to fuse the MR coefficients were implemented. A more detailed explanation of these fusion rules can be found in Section A5.2 in Appendix 5. Combining the MR techniques and fusion rules six fusion and denoising schemes are obtained, as shown in Table 5.1.

Table 5.1 Fusion/denoising Schemes

Scheme	Description
DWT-MS	DWT with *maximum selection*
DWT-WA	DWT with *weighted average*
DWT-WBV	DWT with *window based verification*
DTCWT-MS	DTCWT with *maximum selection*
DTCWT-WA	DTCWT with *weighted average*
DTCWT-WBV	DTCWT with *window based verification*

Considering the SAR images obtained from two polarisations horizontally transmitted horizontally received (HH) and vertically transmitted vertically received (VV) as shown in Figure 5.7, simulated impulse noise was added to the raw hologram data. The images were fused without performing mitigation of impulse noise, and also fused after attempting to mitigate the impulse noise in the images. Finally the results of each approach were compared.

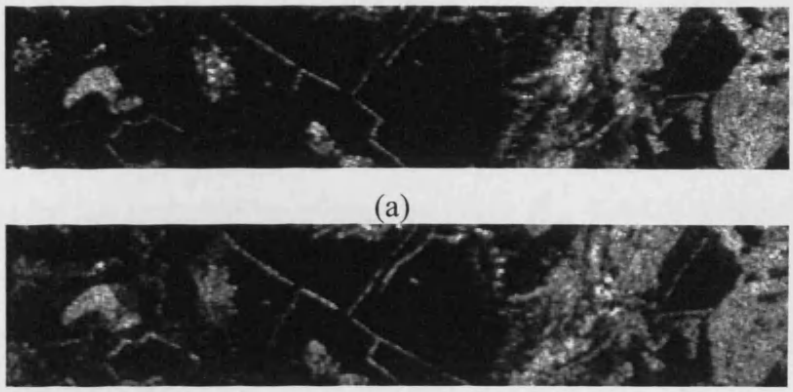

(a)

(b)

Figure 5.7 original SAR images:

(a) HH polarisation; (b) VV polarization.

Figure 5.8 shows the results for fusion of SAR images using the DWT-MS and DTCWT-MS fusion schemes with simulated impulse noise P_{imp} ={0, 0.1, 0.3}, with and without mitigation of impairments.

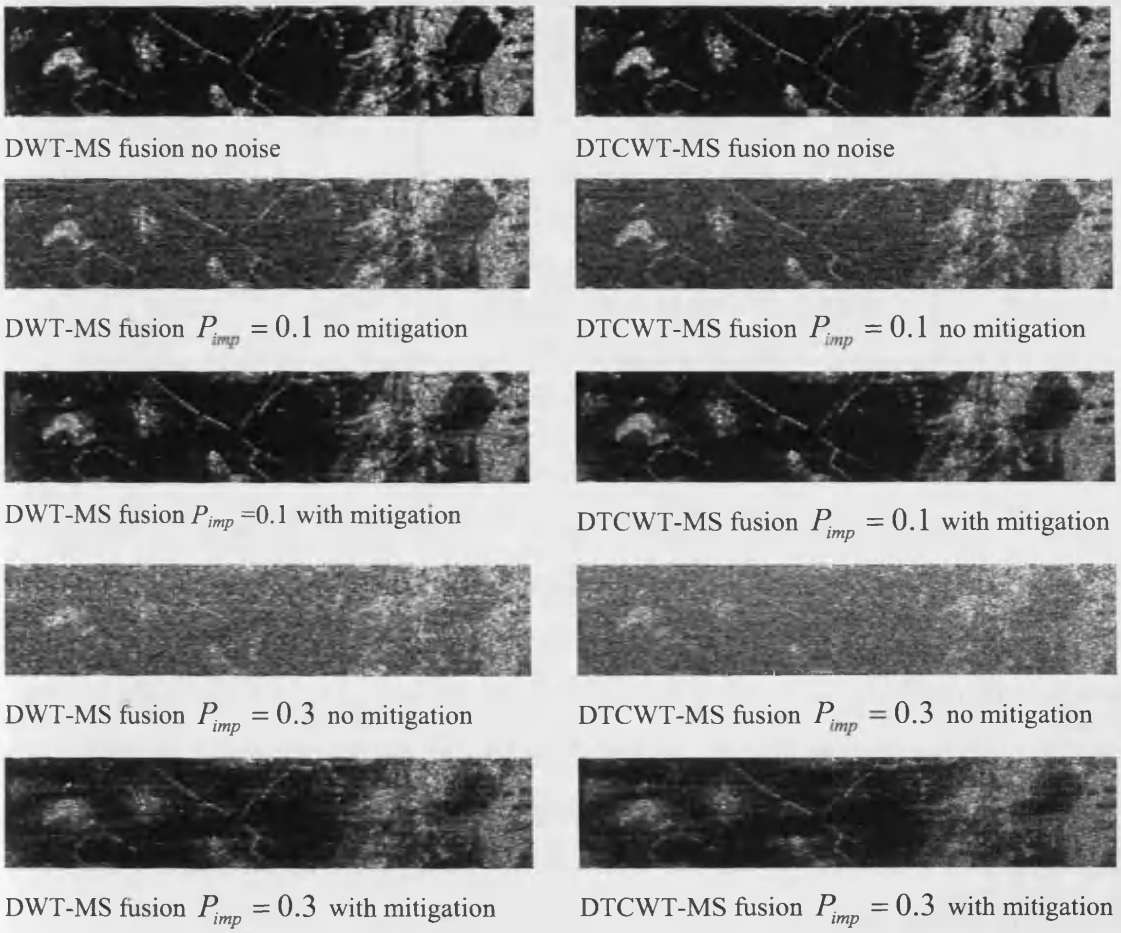

Figure 5.8 Fusion results with and without mitigation

The presence of impulse noise in the images used for fusion severely impairs the fused images, while images corrupt with noise $P_{imp} \geq 0.3$ result in almost total degradation of information content. However, fused images are obtained containing potentially useful information using α-trimmed estimate to mitigate impairments prior to fusion, and for low probabilities of impulse noise $P_{imp} \leq 0.1$ it is possible to recover the majority of important information. Visually DWT and DTCWT offer comparable performance with only minor differences, however, the DTCWT is more robust in the presence of impulse noise.

Quanitative results are presented in Table 5.2 for all fusion schemes in the absence of simulated impulse noise. The quantitative measures MI [102], Q_{abf} and Q_w [103] are discussed in greater detail in Appendix 5 Section A5.3.2. For all three measures larger values indicate better results.

Table 5.2 Quality Measures for Fusion schemes without impulse noise

	DWT-MS	DWT-WA	DWT-WBV	CWT-MS	CWT-WA	CWT-WBV
Q_{abf}	0.68	0.62	0.61	0.72	0.7	0.66
Q_w	0.74	0.72	0.71	0.78	0.78	0.75
MI	0.42	0.43	0.42	0.45	0.47	0.46

Comparing the Discrete Wavelet Transform and Dual-Tree Complex Wavelet Transform it is obvious that the Dual-Tree Complex Wavelet Transform offers an improvement over Discrete Wavelet Transform for all fusion rules with the maximum selection fusion rule outperforming the weighted average and window-based verification. Generally, Q_{abf} and Q_w tend to agree showing CWT-MS to offer superior performance. However, MI identifies CWT-WA as the best overall. For the untrained eye it is difficult to discriminate between the fused SAR images for Discrete Wavelet Transform and Dual-Tree Complex Wavelet Transform, but extensive visual analysis confirms that Dual-Tree Complex Wavelet Transform provides better quality for some edge details and textured areas.

In summary, the α-trimmed estimate is an appropriate alternative to the standard linear algorithm for fusing hologram components and synthesising SAR images, providing robust estimation in an impulse noise and Gaussian noise environment. It has been shown in [41], that the α-trimmed estimate offers superior performance to that of the average estimate in suppressing even severe impulse noise, with the robustness of the α-trimmed algorithm depending on the number of trimmed samples.

The α-trimmed estimate has been shown to exhibit impressive mitigation properties in the presence of impulse noise. More importantly, it has been shown that SAR fusion results can be improved by mitigation of data transmission errors prior to fusion. This two stage approach of using standard algorithms for mitigating impairments and image fusion has shown that it is possible to improve fusion results, with the additional advantage of not having to modify fusion algorithms to cope with impairments present in the source data.

5.2.3 A New Method for Filtering Speckle Noise and Fusing Remote Sensing Radar Data

The work described in this section has been published in [42] and is intended only as a summary of the technique and experimental results. A more detailed analysis can be found in Appendix 2. Speckle noise is common to all coherent imaging systems resulting in 'grainy' texture in SAR/SLAR images. It is due to the random phases of the backscattered signals. Speckle is also due to the fact that often there is more than one discrete point scatterer in each resolution element; therefore, it also depends on the resolution of the radar. The characteristics of speckle are well modelled [93, 95] and therefore, these generally accepted models are used in this thesis.

Details are important in SAR/SLAR images but speckle degrades image quality. Therefore, it is important to reduce speckle prior to any further analysis. Additionally, we also need to suppress speckle to improve the estimate of the backscattering coefficient which is required for clutter modelling in this thesis. However, there exists a trade-off between speckle reduction and preservation of image details. Speckle filtering techniques based on local statistics such as those described by Lee [96], Kuan

[97] and Frost [98], use estimates of expectation and variance within some neighbourhood. The importance of these filters is their ability to work well for multiplicative noise with different pdfs not just Gaussian, including non-symmetric distributions, and their ability to adapt to the characteristics of the noise. Comparative studies have shown that although these methods based on local statistics offer good speckle reduction and detail preservation, they do not perform as well for homogenous regions. An alternative approach is to transform the multiplicative noise to additive noise using the logarithmic transform [95], allowing standard techniques for additive noise removal to be directly applied.

By combining DCT with a MR approach a technique is obtained that is suitable for both denoising and fusion. This technique has good signal localisation properties in both the spatial and frequency domains. Based on this approach a new MR DCT-based method is proposed for simultaneous fusion of SAR images and denoising of speckle noise. The MR Laplacian pyramid transform [43] and orthogonal DCT transform are combined to achieve the advantages of the two individual approaches [89, 99, 100], good time adaptation, and frequency flexibility. It has been demonstrated that using this new approach, simultaneous denoising and fusion is now possible in the DCT transform domain for radar images of the land surface.

Denoising is achieved by thresholding the MR transform coefficients to suppress the effects of noise. Two common approaches for thresholding transform coefficients are hard thresholding and soft thresholding. Hard thresholding reduces all coefficients below the threshold value to zero. Soft thresholding reduces all coefficients by the magnitude of the threshold. Thresholding when applied to wavelet denoising is referred to as wavelet shrinkage because when thresholding is applied we effectively shrink the wavelet coefficients. Hard and soft thresholding techniques can not be directly applied to the multiplicative noisy SLAR data because they are specifically designed to filter AWGN but radar images contain speckle noise which can be considered as multiplicative noise. Instead, we transform the multiplicative noise model to additive noise model by applying the logarithmic homomorphic transform to the SLAR data, allowing soft and hard thresholding techniques to be applied [95, 101].

For the SLAR remote sensing image speckle can be modelled as multiplicative i.i.d Gaussian noise as [95]

$$g_i = f_i n_i, \tag{5.5}$$

where g_i is the observed noisy signal, f_i is the original signal and n_i is noise with unity mean and variance determined by the properties of radar imaging system. The absence of an additive noise component is a common assumption which is commonly adopted. Assuming n_i is independent of f_i, multiplicative noise can be transformed to additive noise by applying the logarithmic homomorphic transform as

$$\tilde{g}_i = \tilde{f}_i + \tilde{n}_i$$

and

$$\tilde{g}_i = \ln(|g_i|),\ \tilde{f}_i = \ln(|f_i|),\ \tilde{n}_i = \ln(|n_i|) \tag{5.6}$$

Here $\tilde{g}_i$ is the logarithmically transformed signal, $\tilde{f}_i$ is the logarithmic transform of the original signal and $\tilde{n}_i$ is the signal-independent noise component. It is assumed that the Gaussian distribution of n_i is not significantly modified by the logarithmic transformation. This issue has been explained in [95], where justification is provided. For simultaneous denoising and fusion the proposed Laplacian pyramid MR-DCT approach is shown in Figure 5.9.

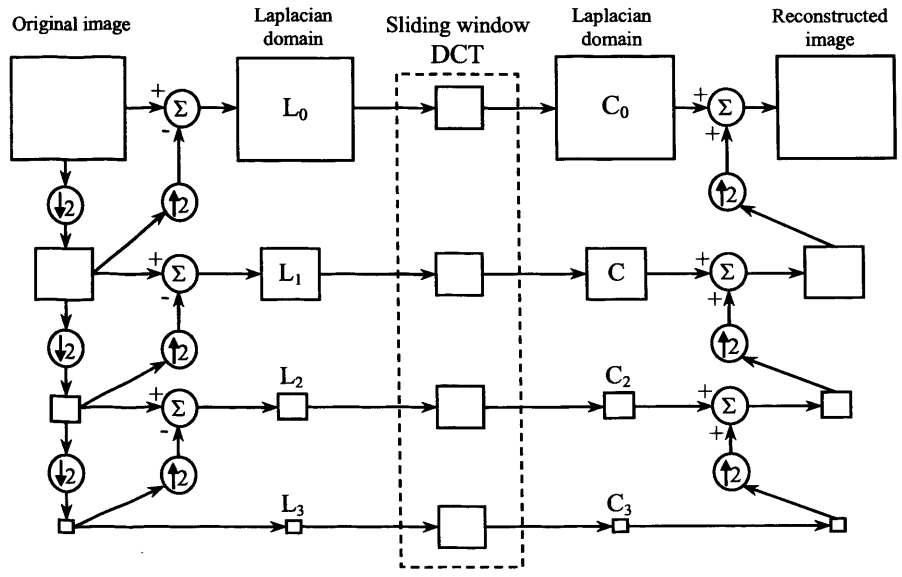

Figure 5.9 MR-DCT scheme for denoising and fusion

The Laplacian decomposition of the noisy signal can be obtained by

$$\mathbf{G} = \mathbf{L}^{l}\mathbf{g}, \tag{5.7}$$

where $\mathbf{G}$ are the Laplacian transform coefficients, $\mathbf{L}^{l}$ is an l-stage Laplacian transform and $\mathbf{g}$ is the noisy signal to be analysed. The sliding window DCT can be regarded as a time-frequency representation which can be expressed as

$$\mathbf{D}^{(m,n)} = \mathbf{T}\mathbf{G}^{(m,n)}, \tag{5.8}$$

where $\mathbf{T}$ is the DCT transform, $\mathbf{D}^{(m,n)}$ are the DCT coefficients of the l^{th} decomposition level of the Laplacian transform coefficients $\mathbf{G}^{(m,n)}$. $\mathbf{G}^{(m,n)}$ is an $M\times N$ frame from the l^{th} level Laplacian decomposition matrix including the coefficients $(m,n),\ldots,(m+M-1,n+N-1)$. Thresholding of the DCT coefficients within a window can be efficiently implemented as

$$\hat{H}_{ij}^{(m,n)} = w_{ij}D_{ij}^{(m,n)}, \tag{5.9}$$

where $D_{ij}^{(m,n)}$ is the ij^{th} spectral coefficient of the signal in the window, w_{ij} are the weighting coefficients of the scalar filter and $\hat{H}_{ij}^{(m,n)}$ is the denoised estimate. Soft thresholding [101] to suppress contaminated coefficients is implemented as

$$w_{ij} = \begin{cases} \operatorname{sgn}(D_{ij})(|D_{ij}| - T) & |D_{ij}| \geq T \\ 0 & |D_{ij}| < T \end{cases}. \tag{5.10}$$

where T is the threshold. The denoised estimate of the Laplacian pyramid transform coefficients are then obtained by applying the inverse DCT transform as

$$\hat{\mathbf{h}}^{(m,n)} = \mathbf{T}^{-1}\hat{\mathbf{H}}^{(m,n)} \tag{5.11}$$

The central value of $\hat{\mathbf{h}}^{(m,n)}$ is the estimate of the denoised coefficient ($m+M/2$, $n+N/2$) of the Laplacian transform. The inverse Laplacian pyramid transform can then be defined as

$$\hat{\mathbf{f}} = \left(\mathbf{L}^{l}\right)^{-1}\hat{\mathbf{h}}, \tag{5.12}$$

where $\hat{\mathbf{f}}$ is the denoised estimate of the noisy signal $\mathbf{g}$, and $\left(\mathbf{L}^{l}\right)^{-1}$ is the inverse Laplacian pyramid transform.

The DWT and state-of-the-art DTCWT methods have been implemented for simultaneous denoising and fusion of SAR images from sensors with different operating characteristics, and compared to the new technique described above. The fusion and denoising schemes in Table 5.1 are implemented for DWT and DTCWT, while the fusion and denoising schemes in Table 5.3 are implemented for MRDCT.

Table 5.3 MRDCT Fusion/denoising Schemes

Scheme	Description
MRDCT-MS	MRDCT with *maximum selection*
MRDCT-WA	MRDCT with *weighted average*
MRDCT-WBV	MRDCT with *window based verification*

The denoising and fusion results were assessed using quantitative metrics to determine the effectiveness of each technique. The techniques were assessed using the mutual information (MI) [102] between the two source images and the fused image, and the qualitative measures proposed by Wang and Bovik, namely Q_{abf} and Q_w [103]. This not the place to discuss these measures but results can be found in [42].

A qualitative visual analysis was also performed to confirm the validity and plausibility of the quantitative measures. Simulations have shown [42] that the multiresolution DCT-based approach can outperform the DTCWT for simultaneous denoising and fusion, demonstrating superior results for textured regions of the test images which were specifically selected to most resemble the textured characteristics of SAR images.

Simultaneous Fusion and Denoising of Test Image

First, simultaneous denoising and fusion is considered for noisy test images. Denoising and fusion is considered for the noisy "Barbara" test images as shown in Figure 5.10. The "Barbara" test image was selected because it is representative of typical SAR imagery as it contains a substantial amount of homogenous regions such as the face and arm, as well as texture detail particularly in the headscarf regions.

Figure 5.10 Denoising and fusion images:
(a) original test image Barbara; (b) test image 1 blurred on left hand side; (c) test image 2 blurred on right hand side; (d) test image 1 blurred on left hand side and simulated noise; (e) test image 2 blurred on right hand side and simulated noise; (f) DWT-WA; (g) DTCWT-WBV; (h) MRDCT-WBV (9×9).

The original noiseless Barbara test image as shown in Figure 5.10(a) is used for the ground-truth data required for image quality estimation. The blurred Barbara test images are shown in Figures 5.10(b)-(c), where the right and left hand sides of the images have been blurred, respectively. The images were blurred so that each image contained important information not present in the other image. This is required so that the performance of the fusion algorithms can be assessed. The blurred Barbara test images with noise added are shown in Figures 5.10(d)-(e). The best fusion and denoising results obtained for DWT, DTCWT and MRDCT are shown in Figures 5.10(f)-(h) respectively. For simultaneous denoising and fusion the DWT-WA shown in Figure 5.10(f) provides the worst results visually, failing to efficiently suppress noise. The DTCWT-WBV Figure 5.10(g) and MRDCT-WBV Figure 5.10(h) provide much better results, but each scheme is better for different reasons. Both schemes provide efficient noise suppression, but the MRDCT offers better texture preservation most noticeable in the headscarf regions. However, the DTCWT suppresses noise to a greater degree in homogenous regions such as the face and hand, while the MRDCT appears to have more artefacts in these areas. There also seems to be a loss in definition of the left side of the face and texture artefacts near the mouth region for the MRDCT scheme. Regardless of this, the texture information is clearly superior for the MRDCT. These observations are supported by the quanitative measures in Table 5.4.

Table 5.4 Denoising and Fusion Results for Barbara test image

Scheme	SNR, dB	MSE
DWT-MS	15.96	472.78
CWT-MS	19.09	229.7
MRDCT-MS (9x9)	18.66	253.69
DWT-WA	16.27	439.82
CWT-WA	18.96	237
MRDCT-WA (9x9)	19.01	234.34
DWT-WBV	16.19	448.55
CWT-WBV	19.09	229.62
MRDCT-WBV (9x9)	19.1	229.48

The visually poor results produced by the DWT are confirmed by lower SNR and MSE estimates. MRDCT and DTCWT achieve comparable results with the MRDCT marginally outperforming the DTCWT. Although the MRDCT attains better texture preservation and the DTCWT performs best for homogenous regions, they still achieve similar values for SNR and MSE. Therefore, each is suitable for different applications depending on the most important criterion, texture or homogenous information.

The test images are perfectly registered; therefore, the shift-invariance properties of the MRDCT and the DTCWT have no real advantage here. For DTCWT fusion and denoising the phase information is not considered by the fusion rules. This would imply that the results achieved for the DTCWT are due to its increased directional sensitivity, having six directional subbands, whereas the MRDCT and DWT only have three directional subbands. The results obtained by the MRDCT must therefore be attributed to its good signal localisation in both the spatial and frequency domains, permitting suitable selection of coefficients for both fusion and denoising.

Fusion and Denoising of SAR imagery

Now two real SAR amplitude images are considered in HH and VV polarisations as shown previously in Figure 5.7. These contain speckle noise with estimated noise variance $\sigma_n^2 = 0.05$. SAR image fusion quality is assessed by estimating how much important information is transferred to the fused image from the input images, using the quantitative measures MI [102], Q_{abf} and Q_w [103]. Visual analysis of the fused results without denoising are shown in Figure 5.11 indicates that the proposed MRDCT provides better quality for some edge details and textured areas.

(a)

(b)

(c)

(d)

Figure 5.11 SAR fusion results:
(a) DTCWT-MS without denoising; (b) MRDCT-MS (3×3) without denoising;
(c) DTCWT-MS with denoising; (d) MRDCT-MS (9×9) with denoising.

SAR image fusion quality is assessed by estimating how much important information is transferred to the fused image from the input images, using the quality measures Q_{abf}, Q_w and *MI*. Quantitative analysis of the results shown in Table 5.5 and are discussed in greater detail in Appendix 2.

Table 5.5 Fusion results for SAR image

Scheme	Q_{abf}	Q_w	*MI*
DWT-MS	0.7	0.796	0.391
CWT-MS	0.745	0.831	0.433
MRDCT-MS (3x3)	0.747	0.824	0.435
DWT-WA	0.665	0.776	0.4
CWT-WA	0.733	0.821	0.456
MRDCT-WA (3x3)	0.725	0.808	0.463
DWT-WBV	0.659	0.774	0.393
CWT-WBV	0.728	0.806	0.426
MRDCT-WBV (3x3)	0.73	0.813	0.455

Generally, all three measures agree that the Multiresolution DCT and Dual Tree Complex Wavelet Transform offer comparable performance for all fusion schemes, with the maximum selection fusion rule attaining best performance. Q_{abf} identifies MRDCT-MS with a (3×3) DCT window as the best fusion scheme, Q_w identifies CWT-MS as the best, and *MI* identifies MRDCT-WA with a (3×3) DCT window as the best.

In summary, different fusion schemes have proven to be more efficient than others depending on the nature of the data and the presence of noise within the data. Results obtained from the simulations conducted on the test images suggest that the MRDCT is good for fusion but it is degraded by noise. However, results obtained for fusion and denoising of the test images suggest that MRDCT provides better noise suppression and texture preservation than the DTCWT, but it is not as efficient for homogenous regions. Additionally, the size of the sliding window used for the DCT affects the results of fusion; a smaller window is desirable for fusion but efficient denoising requires a larger window. Clearly, the tasks of fusion and denoising have conflicting requirements with respect to DCT window size. It is noted that the opportunity exists for improving denoising and fusion results by applying of an

adaptive window size, where the window size is dependent on the image content (texture or homogenous) and the presence of noise within the data. An adaptive window size was not considered in this thesis due to time constraints.

Fusion of multiple sources of SAR data can provide the opportunity for improved estimation of the RCS of the underlying scene, therefore providing better source data for further processing or direct use for an application. The MRDCT has been shown to be a suitable method for efficiently fusing and denoising SAR data. We now return to the task of clutter modelling in Section 5.3 where the new method for predicting land clutter is discussed in detail.

5.3 New Method for Predicting Land Clutter

Predicting land clutter is important for analysing the performance of ground-based radar in detection of low-angle targets. This section describes the methodology for predicting clutter maps using remote sensing data. The novelty lies in application of remote sensing radar data to provide direct RCS measurements of the land surface and fusion for clutter modelling. A clutter map describes how the intensity of clutter is spatially distributed. A site-specific approach to predicting clutter is necessary to account for radar position, radar parameters, terrain topography, and local propagation effects. The clutter model in this thesis accounts for the following most important factors:

- Atmospheric refraction and the Earth's curvature.
- Terrain elevation model.
- Terrain classification model.
- Terrain visibility model.
- Direct measurements of RCS, provided by remote sensing radar.
- Land backscattering model for correcting angular and frequency dependencies.

The main stages of data processing and fusion for clutter map generation are shown in Figure 5.12.

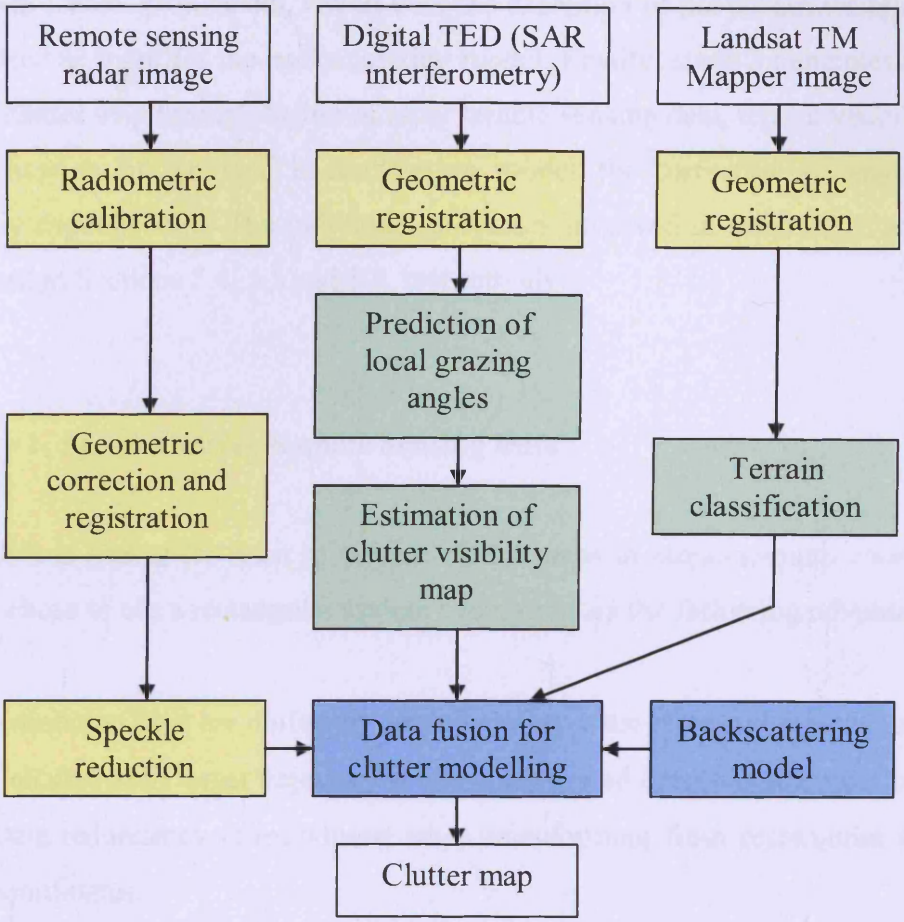

Figure 5.12 Main stages of clutter map generation.

The three data sources required as input are: radar remote sensing image, DTED provided by SAR interferometer, and Landsat TM Mapper image [71]. All of these have been discussed in Section 5.2. The system can then be considered as a 3 stage process:

Stage 1: Pre-processing remote sensing data (yellow)

Stage 2: Estimating and Extracting terrain characteristics (green)

Stage 3: Fusion of terrain data and backscattering model (blue)

Stage 1 involves pre-processing the data including geometric registration of data to a common reference grid, radiometric calibration to compensate radiometric distortions, geometric correction to compensate geometric distortions, and impairment mitigation of radar remote sensing data to suppress noise. Stage 2 involves estimation and extraction of terrain characteristics including local grazing angles, terrain visibility

and terrain surface parameters, which with the exception of the terrain visibility map, are required as input for the backscattering model. Finally, stage 3 generates the site-specific clutter map through fusion of radar remote sensing data, terrain visibility map and application of the land backscattering model for correction of angular and frequency dependencies. The individual processes involved in stages 1, 2 and 3 are considered in Sections 5.4, 5.5 and 5.6, respectively.

5.4 Stage 1: Pre-processing Remote Sensing Data

Although it is typical for radar to present clutter maps in range-azimuth coordinates, we have chose to use a rectangular system because it has the following advantages:

- Resolution cells are uniformly spaced and have the same cell dimensions.
- Calculation of target trajectory is less complicated in rectangular coordinates.
- Data redundancy is introduced when transforming from rectangular to polar coordinates.
- In a polar coordinate system there is a singularity at the position of the radar.

The first stage as shown in Figure 5.12, involves pre-processing the remote sensing data to correct for geometric distortions and sensor impairments. Radiometric calibration of the radar remote sensing data is considered in Section 5.4.1, filtering the radar remote sensing data to remove speckle noise is discussed in Section 5.4.2, and geometric correction and registration of all the remote sensing data to a common coordinate system is detailed in Section 5.4.3.

5.4.1 Radiometric Calibration

Radiometric calibration of the remote sensing radar measurements is essential to reduce the influence of radar characteristics on the measurements of surface reflectivity by converting image pixel brightness into absolute values of the backscatter coefficient. When presented in absolute values, the backscattering

coefficient can be corrected to account for angular and frequency dependencies in order to predict clutter maps. Therefore, calibration errors need to be minimised to improve the accuracy of clutter modelling.

The dynamic range of the signal returns across an image is large because of variations in the antenna pattern, distance, and backscattering coefficient. For propagation in free-space the received power is inversely proportional to the fourth power of slant range R^4, resulting in weak signal returns at far range. To compensate for the $1/R^4$ law, antenna gain may be higher at upper elevation angles than at lower elevation angles. Additionally, the reflectivity of the surface is a function of antenna beam incidence angle. These effects cause variations of intensities in the radar image across the range swath. Radiometric calibration corrects for these effects reducing the dynamic range of the data and ensuring average image brightness and contrast are more uniformly distributed.

The calibration method in [104] was used to calibrate the remote sensing SLAR image acquired by an X-band airborne SLAR sensor onboard the MARS platform [105]. The method combines external and internal calibration methods to compensate variations in antenna and receiver gain with range, achieving a calibration accuracy of about 2dB [104]. Internal calibration measures critical radar parameters such as receiver gain and transmitter power, to achieve continuous control over radar parameters. Internal calibration for the SLAR radar is achieved by directional couplers on both transmitter and receiver circuits to directly connect them together [104]. The connection between the couplers has a known attenuation, and is used to feed the transmitted signal to the receiver to allow relative calibration. The delayed and attenuated radar signal is recorded synchronously with the received radar image. The power of the recorded calibration signal is

$$P_k = \frac{P_e L}{\gamma_c} \tag{5.13}$$

where P_e is the power of the transmitted signal, L is the gain of the receiver and signal processing circuits, and γ_c is the calibration channel attenuation. Using the

radar equation, the absolute values of backscattering coefficient is then estimated from the ratio of the received and calibration signals as

$$\sigma^0 = \frac{(4\pi)^3 R^4}{G^2 \lambda^2 \gamma_c A_0 F} \frac{P_r}{P_k} \tag{5.14}$$

where P_r is received signal power, A_0 is the illuminated area, R is slant range, and F is the propagation factor to account for tropospheric propagation. External calibration is achieved by using corner reflectors and active devices [80], which permit accurate estimation of the G and γ_c parameters.

5.4.2 Speckle Filtering

The properties of speckle and the importance of removing speckle have already been discussed in Section 5.2.3. The approach adopted for speckle suppression shown in Figure 5.10 follows from previous results in Section 5.2.3 and uses the DTCWT, logarithmic transform to convert speckle to additive, and soft thresholding [101]. For experimental purposes the Antonini 9,7 tap filters and Quarter Sample Shift Orthogonal (Q-Shift) 10,10 tap filters [92] were selected, which were determined through simulations to produce the best results for this particular application.

Thresholding the DTCWT coefficients is achieved through a global threshold, which is defined as $T = c\sigma_n$, where c is a single constant used for all directions and decomposition levels, and σ_n^2 is the noise variance of the speckle. Analysis of the uniform regions of the radar image is used to evaluate σ_n^2, while c is determined through simulation. Until an automatic method to determine c is available the application of this thresholding method for real data is limited. The threshold is applied to the magnitude of the DTCWT complex coefficients in each directional subband, excluding the approximation subband.

5.4.3 Geometric Correction and Registration of Remote Sensing Data

To apply remote sensing data for clutter modelling it is necessary to correct the data for geometric distortions due to different sensor geometry and spatial resolution from the ground based radar. Additionally, all the data need to be transformed to a common coordinate system so that corresponding image pixels represent the same spatial location.

For the remote sensing radar the data are presented in slant-range spatial coordinates and therefore must first be converted to ground-range coordinates. Random geometric distortions may also be present due to variations in sensor platform trajectory resulting in image shift, rotation and non-linear distortions. Another source of geometric distortions in remote sensing images result from the curvature of the Earth, however these effects are minimal for low-altitude airborne radar and also for Landsat because of a narrow swath [106].

Geometric correction is applied in two stages. First, slant-to-ground range conversion is applied for the right looking radar, that can be obtained by

$$p_x = \sqrt{(q_x + R_{\min})^2 - h^2} - \sqrt{R_{\min}^2 - h^2}, \quad p_y = q_y \tag{5.15}$$

where (p_x, p_y) and (q_x, q_y) are the point coordinates for the ground and slant ranges respectively, $R_{\min}$ is the minimum slant range, and h is the height of the radar platform.

At the next stage, registration of the ground-range radar image to the topographic map is applied to correct for geometric distortions. This is achieved by selecting ground control points (GCPs) representing identical features in both the radar image and topographic map, such as road junctions, buildings, and curves of rivers. To transform the radar to topographic coordinates an affine transformation is applied to rotate, scale and shift the radar image to match corresponding GCPs in the topographic map. The affine transformation requires six parameters which are estimated automatically by minimising the discrepancy between corresponding GCPs of the topographic map and

radar image. After registration the radar image is now transformed to new coordinates and resampled to be the same format as the topographic map.

For the terrain elevation data obtained from the SIR-C Imaging Radar sensor [70] and Landsat TM data [71], visual analysis confirms that there are no impairments present which may affect the modelling results. Therefore only registration to the topographic map coordinate system is necessary. This is achieved through the same process as for the radar image. For registration of the terrain elevation data the selected GCPs included valleys, steep hills, and buildings, all of which can be identified in the topographic map which is selected as the base image for registration.

The impairments in the remote sensing data have been mitigated, and the data corrected for geometric distortions, and transformed to a common coordinate system. The next stage is to extract from the remote sensing data the necessary terrain information required for clutter modelling. This is considered in Section 5.5.

5.5 Stage 2: Estimating and Extracting Terrain Characteristics from Remote Sensing Data

The experimental land backscattering model uses grazing angle, radar frequency, polarisation, and terrain type for prediction of land clutter intensity at low-grazing angles. Additionally, attention must be paid to terrain visibility due to obstructions caused by elevated terrain. Grazing angle and terrain visibility are essential in determining terrain reflectivity. Both can be calculated using the terrain elevation model and a ray tracing approach such as GO [57] discussed in Section 4.3 and 4.6.

Calculation of local grazing angles is discussed in Section 5.5.1, generation of terrain visibility maps are detailed in Section 5.5.2, and classification of remote sensing data to obtain terrain type is discussed in Section 5.5.3.

5.5.1 Grazing Angle Calculation

For calculation of the local grazing angle it is necessary to account for land surface local slope with respect to radar position, antenna height, the curvature of the Earth and electromagnetic wave propagation in the troposphere. Grazing angle is defined here as the angle between the ray and the terrain slope, where terrain slope is the complement of the surface normal. A flat Earth surface assumption permits simple geometric calculations, and then corrections for the Earth's curvature and electromagnetic wave propagation in the troposphere can be applied to calculate grazing angle.

Grazing angle for a perfectly flat Earth surface can be defined as

$$\psi = \frac{\pi}{2} - \arccos(\hat{n}_r \cdot \hat{n}) \tag{5.16}$$

where $\hat{n}$ is the surface normal, and $\hat{n}_r$ is the unit vector from the surface position pointing towards the radar. The normal vector $\hat{n}$ accounting for slope of the surface can be defined as

$$\hat{n} = \frac{-\hat{x}\xi_x - \hat{y}\xi_y + \hat{z}}{\sqrt{1+\xi_x^2+\xi_y^2}} \tag{5.17}$$

where $\hat{x}$, $\hat{y}$, $\hat{z}$ are unit vectors along the Cartesian coordinates, and ξ_x, ξ_y, are the local slopes along the x and y coordinates. The reduction in grazing angle for a spherical Earth model is defined as

$$\Delta\psi = \frac{r}{2E_R} \tag{5.18}$$

where r is the ground range and E_R is the Earth's radius. A four-thirds Earth model is used to account for propagation effects in the troposphere which assumes standard atmospheric refraction, whereby the E_R is increased 4/3 times [13].

5.5.2 Terrain Visibility Map and Shadowing Effects

Terrain shadowing occurs when free-space wave propagation is interrupted by hills and other obstacles, resulting in clutter attenuation due to some regions not being visible from the radar position. For radar in the microwave band, the wavelength is considerably smaller than the dimensions of the surface macro-relief. Therefore, only directly illuminated areas contribute to land clutter returns. Additionally, diffraction effects are minimal [65], and clutter returns are non-existent for shadowed regions. Based on these assumptions, the GO method for ray tracing provides a suitable method for modelling clutter attenuation due to shadowing effects [13, 57].

Shadowed regions and visible regions are described by the terrain visibility map which is determined by calculating the straight line ray trajectory between the radar antenna position, antenna height, and all other terrain points. A point of the land surface is determined to be in shadow if the ray trajectory intersects the land surface profile. To account for standard tropospheric propagation the four-thirds Earth model is applied to decrease the terrain elevation height with increasing distance from the radar. Using this approach ensures the validity of straight line ray trajectories as used in GO. The effective decrease in terrain height with range can be calculated as

$$h_e = \frac{r^2}{2E_E}, \tag{5.19}$$

where r is range, $E_E = \frac{4}{3}E_R$ is the effective Earth's radius, and E_R is the actual Earth's radius.

5.5.3 Terrain Classification

As discussed in Section 5.1, the terrain type is one of the factors which influence the intensity of the clutter signal returned from the land surface. The terrain type of the land surface can be determined from topographic maps, GIS and land cover maps [56]; however, these are limited by low spatial resolution and long periods between

updates. Accurate prediction of clutter maps require up-to-date information to account for changes within the environment and seasonal variations. Therefore, it is more convenient to use higher resolution remote sensing data and classify this data into terrain classes of interest. The region under consideration (near Kharkov city, Ukraine) consists of six terrain classes: roads; urban areas; water; bare soil; forest; and grass. These terrain classes correspond with the terrain classes required by the land backscattering model to predict clutter intensity [37]. A Radial Basis Function Classifier (RBFC) and Support Vector Machine (SVM) have been shown to be effective tools for classification of terrain type in optical satellite remote sensing images providing accurate classification results [79].

Landsat TM Mapper images and topographic data contain the necessary information to classify the region into specific terrain classes. Initially, ground truth data was used to train the RBFC on four terrain classes: water; bare soil; forest; and grass, as shown in Figure 5.13(a). The RBFC was used to classify the Landsat TM Mapper data but was not trained to classify urban areas and roads for the following two reasons. Firstly, urban areas and bare soil are difficult to discriminate between in the Landsat TM Mapper image and therefore lead to incorrect classification of these two classes in many regions. Excluding urban classes from the classification process resulted in correct classification of all bare soil areas; however, all urban areas are now classified as bare soil. Secondly, roads are extremely difficult to detect in the Landsat TM Mapper image. Therefore, to obtain accurate classification of roads and urban areas, manual classification was necessary; however, it is acknowledged that automatic methods for extraction of roads exist. Topographic data was considered unsuitable for automatic classification using RBFC because it contains symbolic data, grid lines and contour lines; all of which result in misclassification errors. However, topographic data provides the information required for identification of roads, due to the road network being easily detectable. When used in conjunction with Landsat TM Mapper data urban regions can also be easily identified. The RBFC classified image was then fused with the manually classified road and urban classes as shown in Figure 5.13(b)-(c), to provide the final classified data containing all six terrain classes as shown in Figure 5.13(d).

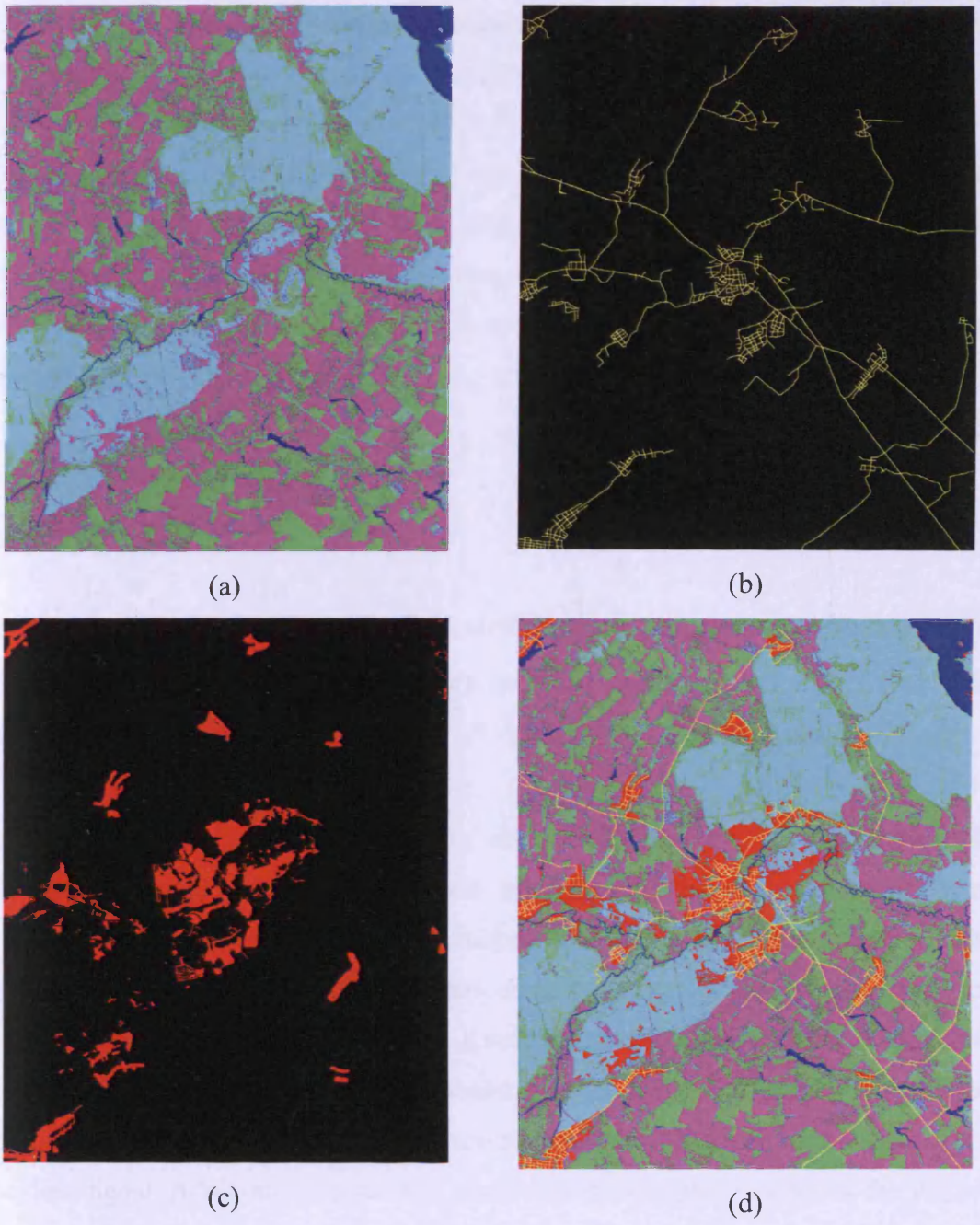

Figure 5.13 Terrain Classification of test site: (a) RBFC for four classes; (b) road class; (c) urban class; (d) final classified image.

Now that we have extracted the necessary terrain information from the remote sensing data, we consider in Section 5.6, the details of the land backscattering model and how fusion of radar remote sensing data can reduce the land backscattering model errors.

5.6 Stage 3: Fusion of Radar Remote Sensing Data, Terrain Data and Application of the Land Backscattering Model

The final stage involved in generating of site-specific clutter maps is fusion of remote sensing data and application of land backscattering models. The empirical land backscatter model is considered in Section 5.6.1, and application of this model for remote sensing data fusion for prediction of site-specific clutter map is discussed in Section 5.6.2.

5.6.1 Land Backscattering Model

In order to generate a site-specific land clutter map it is necessary to determine the backscattering coefficient σ^0 for every position in the clutter map. There are generally two approaches for predicting σ^0: theoretical, and experimental.

The theoretical approach for modelling signal scattering by the land surface is appropriate, providing constraints on the properties of the land surface are met. Backscattering models based on the Kirchhoff and small perturbation methods are applicable in the microwave band for quasi-smooth surfaces without vegetation, such as concrete and asphalt [107, 108]. The Kirchhoff model assumes that the surface is sufficiently smooth and the spatial correlation radius (the averaged width of the irregularities of a rough surface) is significantly smaller than the wavelength of the incident signal. Additionally, boundary conditions for the plane facets of the surface are expressed in terms of parameters that characterise the surface profile. The small perturbation model is valid for quasi-smooth surfaces [107], providing constraints on surface parameters are satisfied. In this case, the standard deviation of surface height should be much smaller than the wavelength. The integral equation method [109] is an extension of these theoretical models and can be used to describe signal scattering from bare soil surfaces, which have higher surface roughness than can be modelled using the Kirchhoff or small perturbation models.

The theoretical models discussed here have demonstrated results consistent with experimental data for particular types of surface without vegetation, such as concrete and bare soil [65]. However, the application of these theoretical models for describing signal scattering from the surface is limited by the following factors:

- They are only applicable for a limited range of surface types and do not provide accurate results for very rough surfaces.
- They can only be applied for spatially homogenous surfaces which can be expressed by a single roughness parameter; therefore they are not applicable for surfaces with complicated geometry.
- They assume that the backscatter coefficient for quasi-smooth surfaces is a function only of surface roughness and the dielectric constant of the surface.

The experimental approach uses empirical models which are based on the analysis of experimental measurements of the backscattering coefficient, and are valid for a wider range of radar parameters and land surface types. This advantage of empirical models justifies application of the experimental approach for our purposes, rather than the theoretical models for determining σ^0 which are only valid for the limited surface types as discussed above. The clutter modelling approach in this thesis uses the empirical backscattering model developed in [37, 65] which classifies the land surface into basic terrain types that correspond well to the terrain types present in the radar deployment region considered in this thesis. The experimental backscattering model accounts for radar parameters and local terrain characteristics. This empirical model is valid for millimetre-wave radar frequencies from 3-100 GHz, and maximum grazing angle $<30°$, which is within the range of radars considered in this thesis. For horizontally transmitted and received polarisation (HH) the backscattering coefficient can be obtained by

$$\sigma^0_{HH}(\psi, f) = A_1 + A_2 \log_{10}(\psi/20) + A_3 \log_{10}(f/10), \text{ dB} \qquad (5.20)$$

where $\sigma^0_{HH}(\psi, f)$ is the backscattering coefficient in dB, f is the radar frequency in GHz, and ψ is the grazing angle in degrees. The coefficients $A_1 - A_3$ are determined by terrain type, as listed in Table 5.6 [65 p.161].

Table 5.6 The Coefficients $A_1 - A_3$ for the Land Clutter Model

Terrain type	A_1	A_2	A_3
Concrete	–49	32	20
Arable land	–37	18	15
Snow	–34	25	15
Deciduous and coniferous forests, summer	–20	10	6
Deciduous forest, winter	–40	10	6
Grass with height > 0.5 m	–21	10	6
Grass with height < 0.5 m	–(25-30)	10	6
Urban territories (town and country buildings)	–8.5	5	3

The empirical model (5.20) and Table 5.6 categorise the land surface into a limited number of terrain classes commonly found in radar coverage regions. The backscattering coefficient for VV polarisation can then be defined as [65]

$$\sigma_{VV}^0 \cong \begin{cases} \sigma_{HH}^0 + 10\left(\frac{f}{10}\right)^{\frac{1}{2}} & \text{dB, for quasi - smooth surfaces} \\ \sigma_{HH}^0 & \text{dB, for other surfaces} \end{cases} \qquad (5.21)$$

Subsequently, the cross-polarised component of the normalised RCS is determined as

$$\sigma_{cross}^0 = \sigma_{HV}^0 = \sigma_{VH}^0 \approx \sigma_{HH}^0 - 10, \text{dB} \qquad (5.22)$$

Equation (5.22) is valid for all of the surface types considered except for quasi-smooth surfaces; in which case, the cross-polarised component of the backscattering coefficient is equal to zero (-∞ in dB).

Equations (5.20)-(5.22) have been determined by solving the radar equation for the returned clutter power obtained through experimental measurements [66]. For these measurements clutter power is defined as σF^4 (because it is difficult to separate the backscatter coefficient from propagation effects and because of the small influence of the propagation factor F for microwave band measurements). Measurements obtained

for the terrain backscatter coefficient (including propagation factor F) for X-band and higher radar frequencies, is relatively small compared with measurements obtained at lower frequency bands. Therefore, we can assume $F^4 = 1$ for X-band and shorter wavelength land clutter modelling.

Then, using the empirical backscattering model (5.20) the backscattering coefficient σ^0_{LB} for the land-based radar, which has a different position and operating frequency compared with the remote sensing radar, can be predicted for HH polarisation as

$$\sigma^0_{LB} = \sigma^0_{RS} + A_2 \log_{10}(\psi_{LB}/\psi_{RS}) + A_3 \log_{10}(f_{LB}/f_{RS}), \text{ dB} \qquad (5.23)$$

where σ^0_{RS} is the backscattering coefficient measured by the remote sensing radar, f_{RS} is the remote sensing radar operating frequency, and ψ_{RS} is grazing angle for the remote sensing radar. The land-based radar operation frequency is f_{LB}, ψ_{LB} is the local grazing angle for the position of the land-based radar, and coefficients A_2, A_3 are given in Table 5.4. An interesting point to note is that the coefficient A_1 has been replaced by σ^0_{RS} implying that errors introduced by the empirical model are reduced. Additionally, if the same operating frequency is selected for both land-based and remote sensing radar, then the term $A_3 \log_{10}(f_{LB}/f_{RS})$ disappears from the equation. The result of this observation is that now the accuracy of the clutter model is dependent on the accuracy of the following factors: the remote sensing radar data, coefficient A_2 from the empirical model, the terrain classification data, and terrain elevation data used for calculating the local grazing angles for both land-based and remote sensing radar. The expressions for estimating the backscatter coefficients for VV and cross-polarisation follow from Equations (5.21)-(5.22).

5.6.2 Fusion of Remote Sensing Radar Data, Terrain Data, and Application of the Backscattering Model

The final stage in generating the clutter map involves fusion of radar remote sensing data, terrain classification data, and local grazing angle data to calculate the

backscattering coefficient for every image pixel. The clutter map is presented in a rectangular coordinate system with uniform spacing, where the grid cell size is determined by the spatial resolution of the remote sensing data. The pre-processing stage ensures all data are co-registered in the same coordinate system so that corresponding pixels represent the same spatial position. The backscattering coefficient is predicted for each pixel position by applying the backscattering model to the remote sensing data as

$$\sigma^0_{LB}(i,j) = Somefunctionof\left[\sigma^0_{RS}(i,j), T(i,j), \psi_{LB}(i,j), \psi_{RS}(i,j), f_{LB}, f_{RS}\right] \quad (5.24)$$

Terrain shadowing effects are minimal for remote sensing radar where terrain height variations are moderate, but have a significant impact on land-based radar clutter modelling [110]. Terrain shadowing effects are not accounted for in Equation (5.24); therefore, the terrain visibility map must be applied to account for clutter attenuation in shadowed regions as follows

$$\sigma^0_{cm}(i,j) = \sigma^0_{LB}(i,j)S(i,j) \quad (5.25)$$

Here $\sigma^0_{cm}(i,j)$ are the site-specific backscattering coefficients and $S(i,j)$ is the terrain visibility map. This is a binary map where one corresponds to visible terrain and zero represents shadowed terrain, where backscattering does not occur.

5.7 Experimental Site-specific Modelling of Land Clutter

Experimental results are now presented using measured remote sensing data for generation of site-specific land clutter map for land-based radar. The site selected can be classified by the terrain types listed in Table 5.6, including forest, agricultural land, grassland, urban regions and roads, where most of the territory can be categorised as rural low-relief according to the classification in [73]. The topographic map of the site near Kharkov in the Ukraine is shown in Figure 5.14.

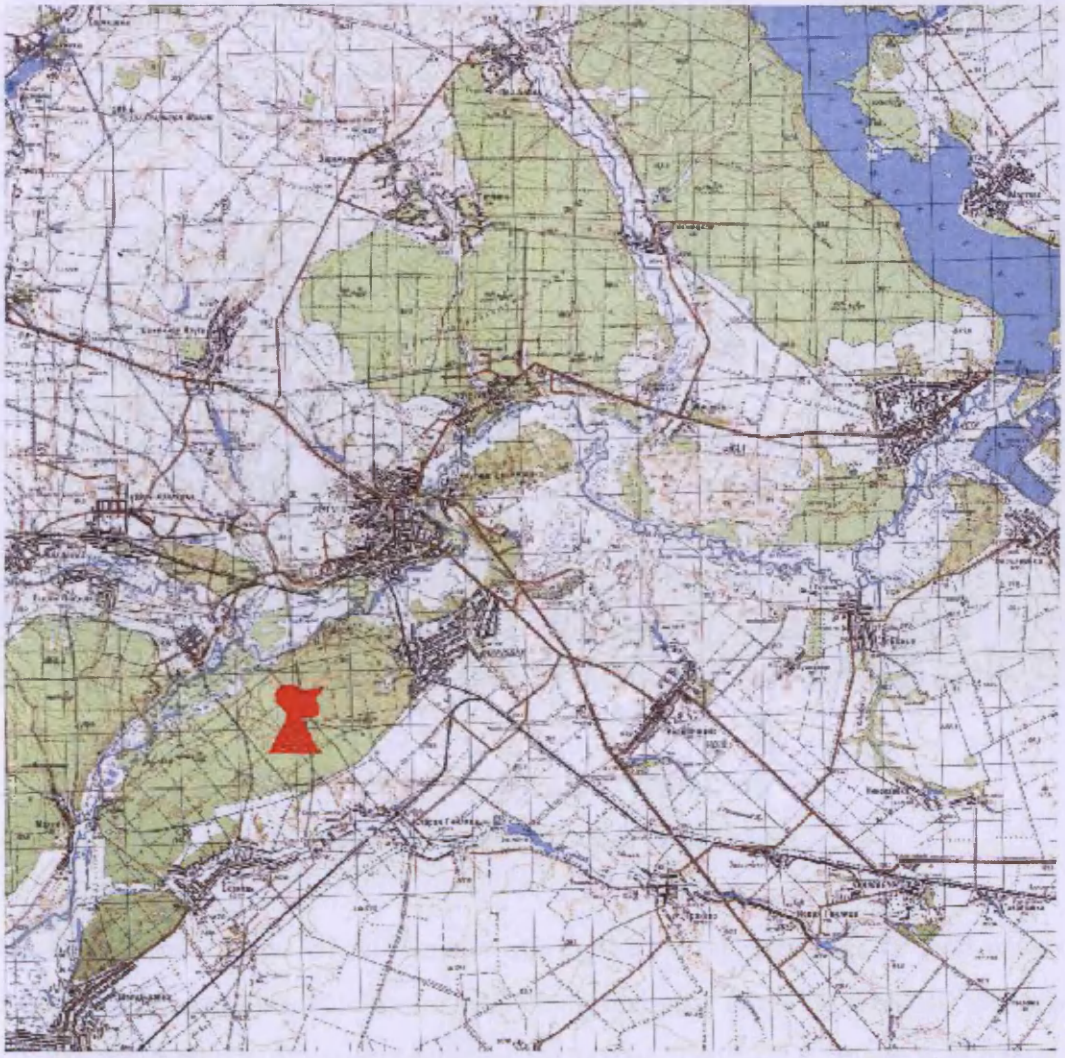

Figure 5.14 Topographic map of test site.

The land-based radar is located 25 metres above the land surface. Its position is indicated by the red symbol. For prediction of the land clutter map two approaches are adopted, and a comparison made between the two methods. Firstly, the land backscattering model (5.20) is applied to the terrain classification map and grazing angle data to predict clutter intensity. Secondly, the method (5.24) is applied based on fusion of remote sensing radar image, terrain classification map, grazing angle data, and application of the land backscattering model to predict clutter intensity. We will now discuss the results of the various stages involved in the prediction of clutter intensity.

The remote sensing radar image was obtained by the multipurpose airborne platform "MARS" [105], which is equipped with two SLAR sensors that operate independently

in Ka band and X band. The remote sensing radar image shown in Figure 5.15(a) was acquired by an X band SLAR sensor operating at 3 cm wavelength, VV polarisation, and slant-range resolution of about 30 metres.

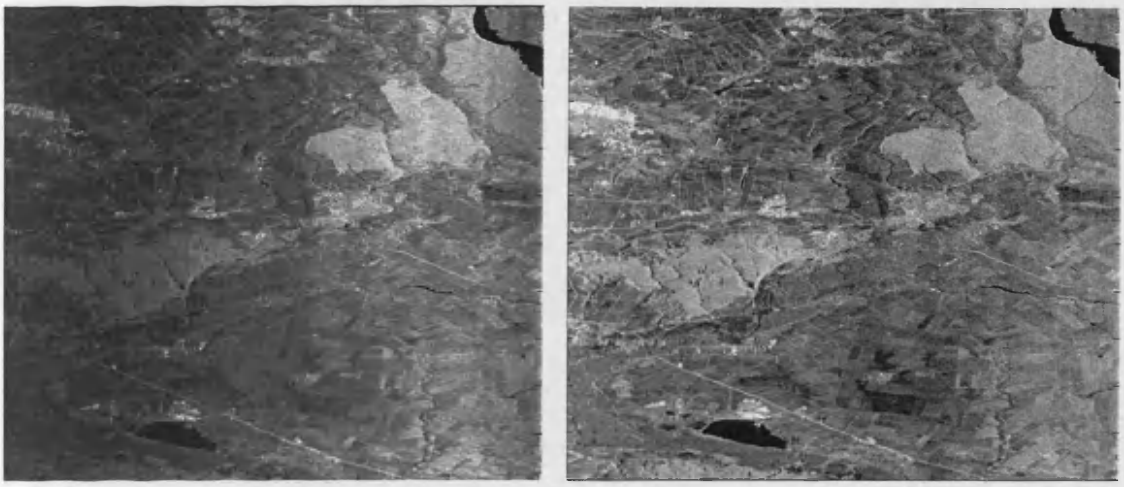

(a) (b)

Figure 5.15 X-band SLAR image of test site:
(a) original image; (b) after calibration.

Visual analysis of the SLAR image in Figure 5.15a) identifies a non-uniform distribution of image brightness observed along the radar range (horizontal) direction, and also the presence of speckle noise in the image. The SLAR image was obtained from a left-look direction resulting in the right side of the image being brighter due to the fact that these positions are spatially closer to the SLAR sensor. The radiometric calibration method was applied to compensate for antenna gain variations, radar system influences on measurements, and to convert the backscattering coefficients to absolute values. The calibrated SLAR image with uniform image mean brightness in the range direction is shown in Figure 5.15(b). Correction for geometric distortions is achieved using an affine transformation to scale, shift and rotate the data in order to co-register the image to topographic coordinates. The geometrically corrected and co-registered SLAR image presented in dB is shown in Figure 5.16(a).

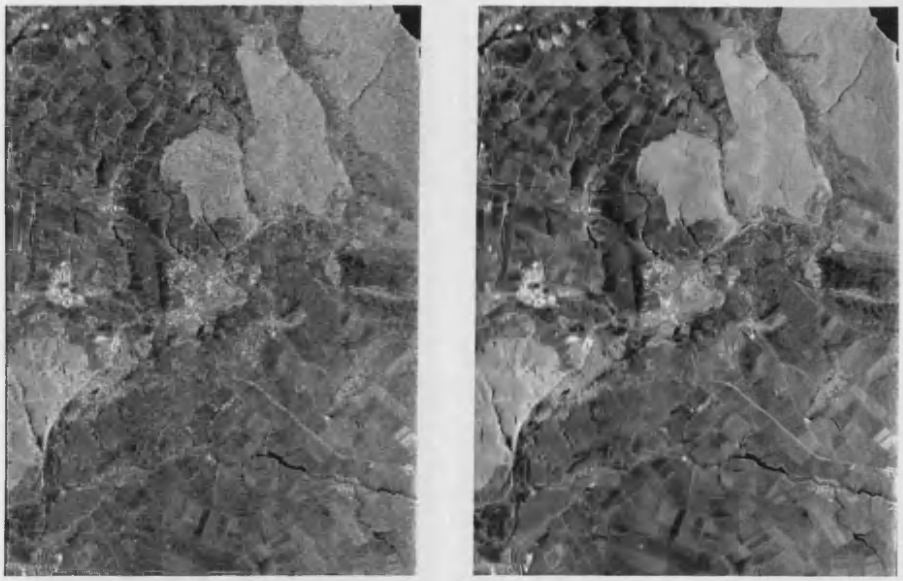

(a) (b)

Figure 5.16 Different stages of SLAR image processing: (a) geometric registration; (b) speckle noise suppression.

24 GCPs were selected in both topographic map and SLAR achieving a discrepancy of about 3 pixels between corresponding GCPs after the transformation. Speckle reduction was achieved by application of the DTCWT with soft thresholding as discussed in Section 5.4.2, and the filtered image is shown in Figure 5.16(b). Clearly, the appearance of the processed radar image in Figure 5.16(b) has been significantly improved and geometric distortions have been removed in comparison with the original radar image in Figure 5.15(a).

The digital terrain elevation model of the test region is generated by a radar interferometer, providing an elevation measurement accuracy of about 12 metres over the whole site. The interferometer measurements can be obtained from [70], and were acquired by the SIR-C Imaging Radar in 2000. The affine transformation was applied using 45 GCPs for geometric registration of the terrain elevation map to the coordinate system of the topographic map, achieving an estimated 2 pixel discrepancy between corresponding GCPs after registration. After geometric registration of the terrain elevation map local grazing angles for the land-based and remote sensing radars can be estimated as shown in Figure 5.17(a) and (b), respectively.

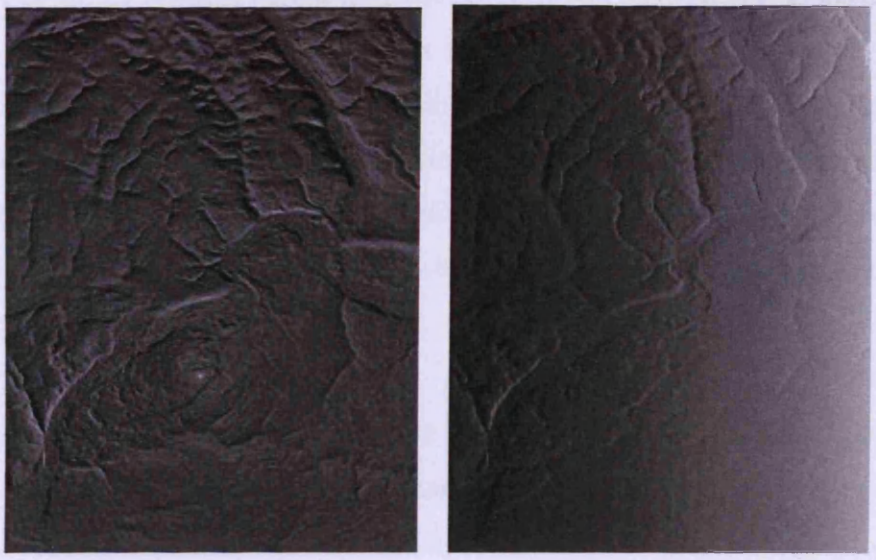

(a) (b)

Figure 5.17 Predicted local grazing angles for: (a) the land-based radar; (b) the remote sensing radar.

Note the clear differences in grazing angles due to different elevation and positions of the sensors. For calculation of the terrain visibility map for the land-based radar shown in Figure 5.18, terrain elevation data and the GO ray tracing method was applied to determine which regions of the terrain are visible from the radar position.

Figure 5.18 Visible and shadowed regions for the test site.

The position of the radar is denoted by the red symbol, shadowed regions are shown in black, and directly illuminated regions are shown in white. The terrain visibility map has been estimated for the radar with an antenna height of 25 metres above the land surface at the radar position. Approximately 73% of the site is shadowed by the relief of the terrain. The visible clutter regions can be further reduced by lowering the height of the radar antenna; however, this will also reduce the visibility of low-angle targets.

The results of terrain classification by the Radial Basis Function Classifier (RBFC) artificial neural network, fused with the manually classified data, are shown in Figure 5.19.

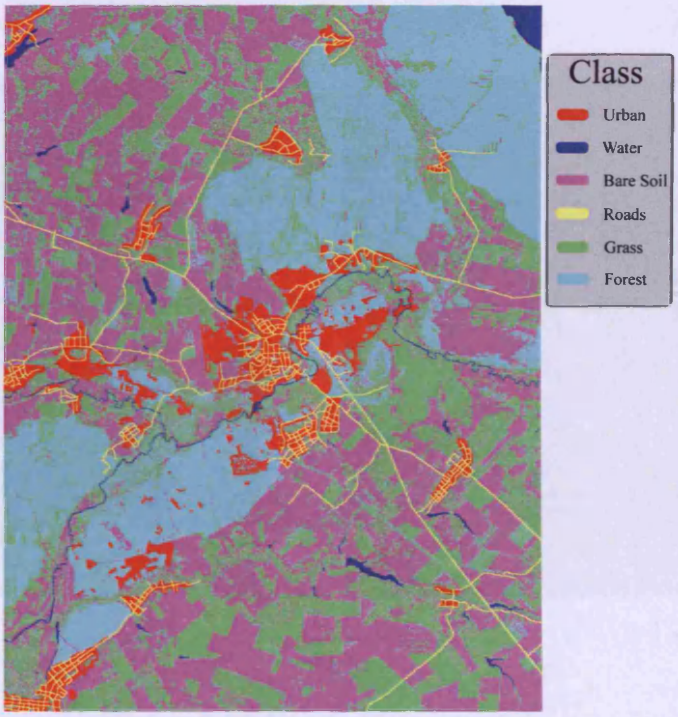

Figure 5.19 Terrain classification map.

The RBFC was trained using fragments of the terrain manually classified as grass, water, forest, and arable land as described in section 5.5.3. The number of training samples was 1.7% of the whole classified image. The cascade-correlation algorithm [111] was implemented at the training stage to determine the number of nonlinear elements in the RBFC artificial neural network hidden layer. The number of nonlinear

elements was automatically selected as 4. For the training samples, a classification accuracy of 96% was achieved.

Terrain classified as water corresponds to rivers and lakes; however, these do not appear in Table 5.6. Therefore, a constant value of -30dB is assigned for the water class backscattering coefficient, which is valid for VV polarised X-band radar operating in moderate wind conditions. The final stage is generation of site-specific clutter maps. The proposed method (5.24-5.25) is shown in Figure 5.20(a), for prediction of a site-specific clutter map by fusion of remote sensing radar data and application of the backscattering model. For comparison purposes Figure 5.20(b) shows the clutter map generated by the land backscattering model, terrain elevation, and terrain classification data only.

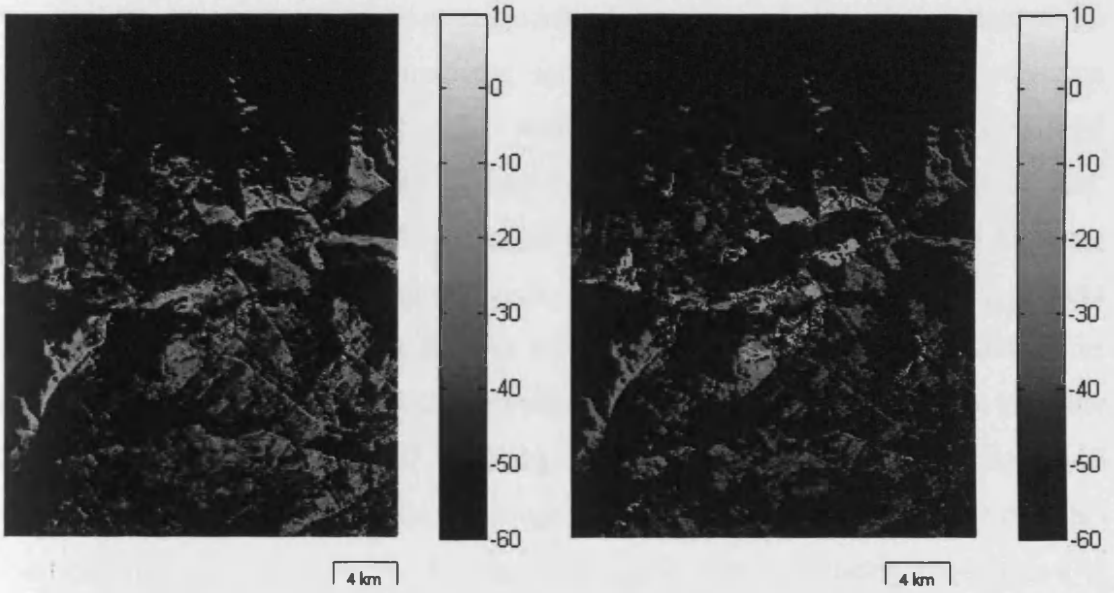

(a) (b)

Figure 5.20 Land clutter model:
(a) based on radar, TED, and optical remote sensing data;
(b) based on only TED.

Analysis of the predicted clutter models in Figure 5.20 identifies that the new method proposed in this thesis, Figure 5.20(a), predicts higher clutter intensity for various areas, most noticeable at far ranges, and that information content has been improved particularly for bare soil regions. A similar effect has been observed in [74] where the clutter modelling approach fuses Defence Mapping Agency Data with TED,

indicating that accurate information about the environment is required or else clutter impact may be underestimated. The new method addresses this issue by incorporating additional radar remote sensing data to provide additional information about the land surface, in the form of direct RCS measurements. Clearly, the more information we have about the environment, then the more accurately we can predict land clutter.

An obviously important question is that of the accuracy of the clutter model. An examination of this issue was undertaken by a colleague, Dr Andrey Kurekin, and is reported in the journal paper submitted to the Elsevier Journal on Information Fusion [38]. Clutter modelling accuracy was assessed by using two remote sensing images obtained from different trajectories (looking at the considered region from opposite directions). The proposed method (5.24-5.25) was applied to radar remote sensing data acquired from one trajectory in order to predict the clutter map for the airborne sensor at the other trajectory. This approach allows the predicted clutter maps to be compared to real radar measurements for assessment of clutter map prediction accuracy. For the clutter model (5.20) which only applies TED a greater than 8dB error was achieved for more than 50% of the region, with a minimum error of 5dB. For the proposed method (5.24-5.25), an error of less than 4dB was achieved for more than 90% of the region, this agrees with a 2dB calibration error for each remote sensing image. A greater than 4dB error was achieved for the remaining 10% of the region, with errors greater than 8dB for bare soil and vegetation surfaces. We attribute the higher errors for bare soil and vegetation to non-isotropic scattering from ploughed troughs and rows of planted crops. It is the authors' point of view that this situation may be improved by fusion of multiple remote sensing trajectories to account for non-isotropic scattering from certain surface or object types.

5.8 Conclusions

This chapter has demonstrated the advantages of using up-to-date remote sensing data to improve the accuracy of site-specific land clutter prediction for surface-sited low-grazing angle radar. The novelty of this approach is application of radar remote sensing images provided by SAR/SLAR for estimation of the land backscattering

coefficient, and implementation of the empirical land backscattering model only to correct for angular and frequency dependencies of measured clutter intensity.

The new technique for clutter modelling proposed in this chapter has been illustrated using measured data which was acquired from a variety of sources. It has been shown that fusion of radar remote sensing data, information about the terrain and application of an empirical model of the land backscattering process can provide additional information about the clutter intensity. The advantage of using radar remote sensing data to provide the required information for clutter modelling is that direct measurements of RCS provides the opportunity for more accurate clutter prediction.

The clutter modelling technique presented in this chapter is an integral component within the intelligent radar sensor, as it allows environmental influences to be accounted for by using up-to-date information provided by remote sensing data. The accuracy of predicting radar performance is improved by prediction of up-to-date clutter maps for the deployed region because it can account for the dynamically changing nature of environmental clutter and benefits from direct RCS measurements.

Potential applications for the intelligent radar sensor will be discussed in Chapter 6 to illustrate the advantages of predicting radar sensor performance for the scenarios considered.

Chapter 6

Improved Radar Sensor Performance

In this chapter, three scenarios are identified for application of the intelligent radar sensor architecture. This is followed by a discussion of how the intelligent radar sensor can be implemented to solve the problems considered. Finally, measured data is used to implement the scenarios identified. The advantages of the intelligent radar sensor approach for predicting radar sensor performance in order to optimise radar operation are assessed.

6.1 Scenarios for Application of the Intelligent Radar Sensor

We now consider a few possible scenarios which could benefit from the intelligent radar sensor (IRS) approach. For ship-based radar where the radar needs to observe a specific region of the land on the coast, a possible solution is to sail along the coastline taking sequential measurements until the required data is obtained. However, it is more desirable to predict at what locations the sensor will be able to meet its objectives (observe the required region), then intelligently select the most appropriate location and move directly to this position to take the necessary measurements. This will minimise exposure time to hostile radar and weaponry.

The data set used in this thesis which had been described in Chapter 5, is specifically suitable for ground-based radar applications; therefore, the following three scenarios are selected for experimentation: radar deployment; radar sensor network; and mobile radar. We will now consider these three scenarios in greater detail.

6.1.1 Radar Deployment Scenario

For the task of radar deployment in a new region or territory, the IRS can be used as a planning tool to predict radar performance prior to deployment and optimally position the radar sensor. The benefit of this approach is reducing the possibility of selecting

inappropriate positions for the radar sensor, therefore avoiding the burden (in terms of time, resources, and cost) of having to relocate the radar after deployment.

6.1.2 Radar Sensor Network Deployment Scenario

Another important task is deployment of a network of radar sensors, either for optimal coverage of the deployment region, or alternatively, for use in a radar sensor network fusion scenario where sensor measurements are fused for improved joint probability of detecting targets. For the fusion scenario, performance of the radar sensors is assessed when measurements are fused to improve detection probability to minimise the effects of clutter and multipath. Considering this scenario, the IRS can be employed to predict radar performance for every location, and then an optimisation task performed to determine the most appropriate spatial configuration for the radar sensors to achieve the desired objective. Depending on whether the purpose of network deployment is optimal coverage of the region or a sensor fusion-based scenario a slightly different approach is required.

6.1.3 Mobile Radar Scenario

For mobile ground-based radars or airborne radars that need to change location to observe some part of the territory that is not visible from the current position, prediction of radar sensor performance can assist in intelligent selection of both position and optimal route to that position or flight route. In this case the objective is to achieve or maintain a specified probability of detection for targets and improve radar sensor performance.

Experimental results for each of the three scenarios are presented in Section 6.3. In Section 6.2 we will now discuss how the intelligent radar sensor can be applied to solve the problems posed by each scenario.

6.2 Application of the Intelligent Radar Model for the Three Scenarios

Although the three scenarios considered are different, in principle they can be broken down into one of two tasks.

- The IRS may need to change position in order to maintain current sensor performance and meet current objectives.
- The IRS may be tasked with new objectives and therefore may need to change position in order to meet the new objectives.

Essentially, both tasks are similar, in that the goal is to change the current position of the radar sensor in order to meet its objectives. The IRS can be implemented to solve these tasks as shown in Figure 6.1.

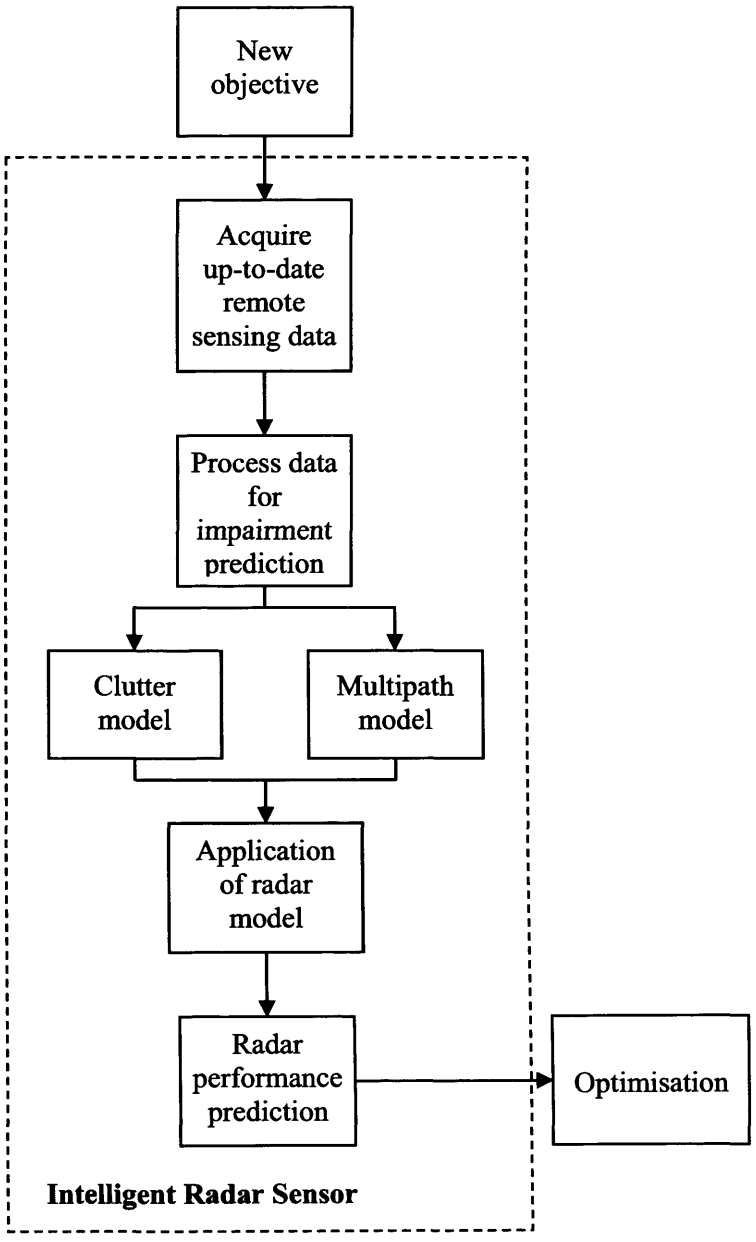

Figure 6.1 Intelligent Radar Sensor Application

Upon recognition that the sensor is failing to meet its current objective or in response to new objectives being issued, the IRS will react in the following way. New remote sensing data is requested and acquired by the sensor. This data is then processed to identify and mitigate any impairment present, using the techniques presented in Chapter 5. The IRS then predicts all applicable clutter maps and multipath effects by using the techniques presented in Chapters 4 and 5, for all the relevant positions within the environment. The radar model discussed in Chapter 3 is then applied to the clutter map data and multipath model to predict probability of detection maps. These are considered as the measure of radar performance for the IRS. Finally, an optimisation task is performed to select the best solution that meets the goals and objectives of the IRS. The task of optimisation is not considered in this thesis because it is a complex issue which requires further investigation; however, it is an important component of the IRS which is required for intelligent operation.

We will now discuss the advantages of implementing the intelligent radar sensor approach to solve the problems posed by the scenarios outlined in section 6.1.

6.3 Application of Measured Data for the Scenarios Considered and Discussion

The intelligent radar sensor is now applied using measured data for the three scenarios discussed in Section 6.1. The benefits of this approach for deployment of a radar sensor are demonstrated in Section 6.3.1. Deployment of a radar sensor network and fusion of radar data is illustrated in Section 6.3.2, and mobile radar route prediction is discussed in Section 6.3.3. The radar parameters for these scenarios are detailed in Chapter 3 and can be found in Table 3.1 and Table 3.2.

6.3.1 Radar Sensor Deployment

In this scenario the idea is to select the best position for deployment of a radar sensor in a new region. To demonstrate the advantages of applying the IRS for this scenario we will consider two radar positions, one good and one bad, as shown by the red symbols in Figures 6.2(a) and (b). We will then discuss the factors which need to be

considered to determine what constitutes a good or bad position. To illustrate how the IRS can be applied to help solve this task we will consider the clutter map which accounts for terrain shadowing effects, target visibility due to terrain shadowing effects, and probability of detection. The clutter maps for the two radar positions are shown in Figure 6.2.

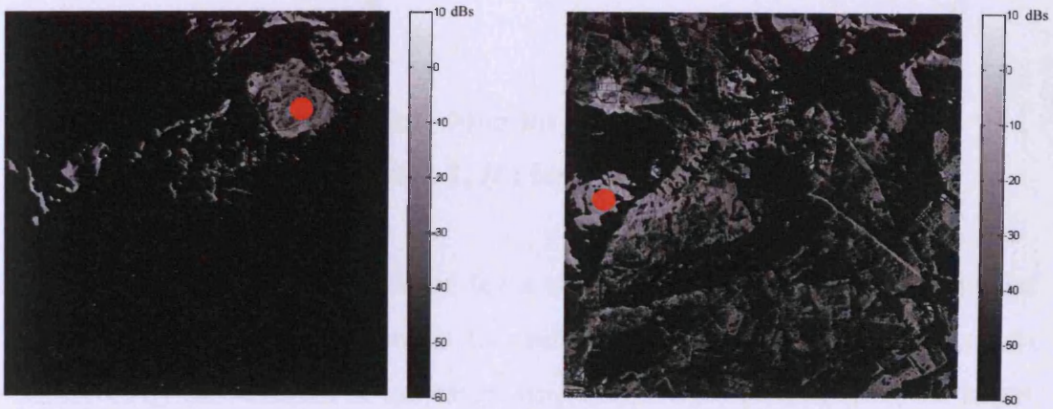

(a) (b)

Figure 6.2 Clutter Map for the whole region:
(a) for radar position 1; (b) for radar position 2.

The radar position in Figure 6.2(a) is considered bad because much of the region is in shadow (93.13%) meaning that low-altitude terrain following targets may be hidden from the radar, however, higher altitude targets will be easier to detect due to the reduced clutter levels. The radar position in Figure 6.2(b) is considered a better position because only 53.95% of the terrain is in shadow, meaning that the probability of low-altitude targets being shadowed by terrain is reduced, albeit at the expense of higher clutter intensity in non-shadowed regions. To illustrate the problem of target shadowing consider the target visibility maps for both radar positions as shown in Figure 6.3.

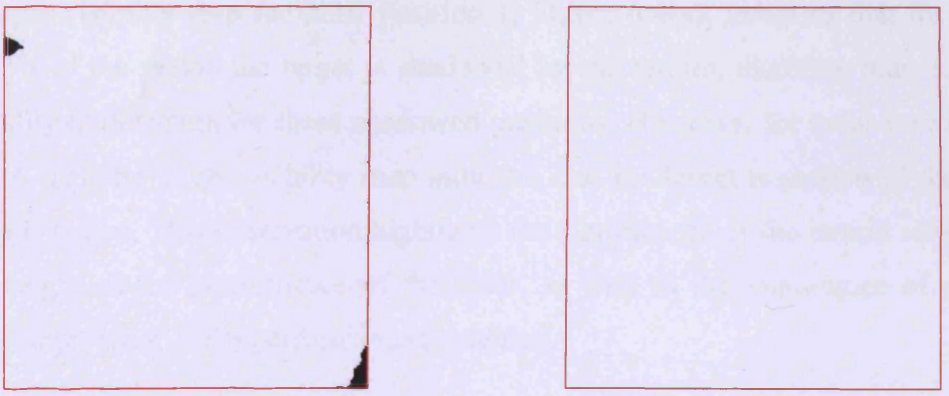

(a) (b)

Figure 6.3 Target Visibility Map for Target Height of 250m: (a) for radar position 1; (b) for radar position 2.

The target visibility maps are calculated for a target height of 250m above the flat Earth surface, where white corresponds to visible target and black corresponds to target shadowed by the terrain. For this target height above the land surface, the target visibility map for position 1, Figure 6.3(a), shows that the target is only in shadow for a small percentage of the whole region; while for radar position 2 the target is *visible completely for the whole region*. If we now consider a target with height of 150m, we can begin to understand the importance of target shadowing and the implications it has on radar performance, as shown in Figure 6.4, where, as before white represents visible terrain and black represents shadowed terrain.

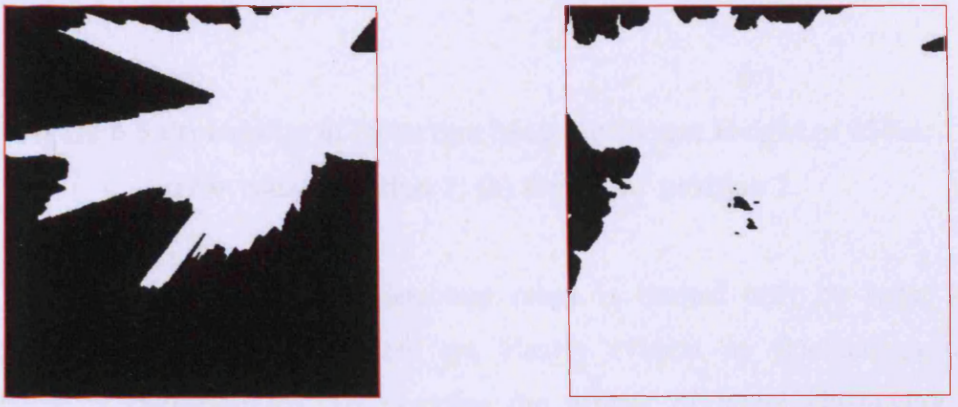

(a) (b)

Figure 6.4 Target Visibility Map for Target Height of 150m: (a) for radar position 1; (b) for radar position 2.

The target visibility map for radar position 1, Figure 6.4(a), indicates that for more than 63% of the region the target is shadowed by the terrain, therefore reducing the probability of detection for these shadowed positions. However, for radar position 2, Figure 6.4(b), the target visibility map indicates that the target is shadowed for only 7% of the region. This observation highlights the significance of the terrain relief and target height on the performance of the radar, as well as the importance of a site-specific approach to radar performance modelling.

For this scenario, radar performance is ultimately assessed using the probability of detecting a target with 6dBsm constant RCS (meaning that the echo from the target does not fluctuate). The probability of detection maps for both radar positions are shown in Figure 6.5. Note the circular boundaries indicating the limited coverage range of the radar. Here the probability of detection maps have been truncated to the radar maximum detection range.

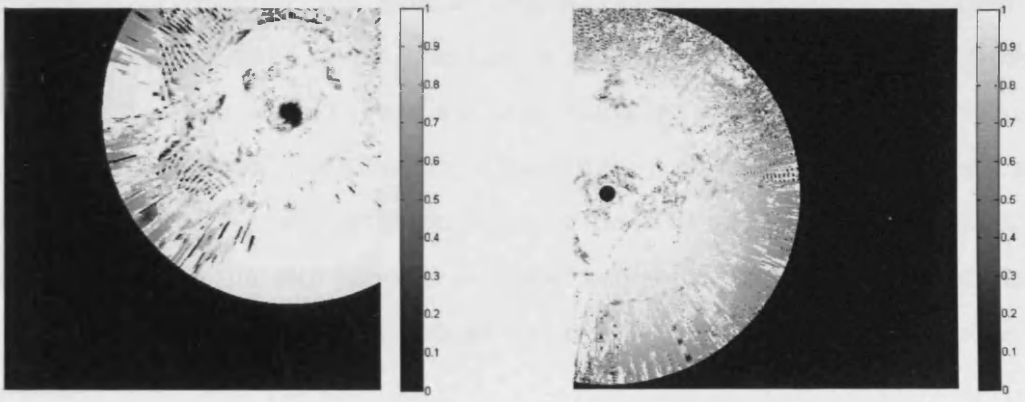

(a) (b)

Figure 6.5 Probability of Detection Map for Target Height of 250m: (a) for radar position 1; (b) for radar position 2.

Here we can see that maximum detection range is limited only by radar sensor characteristics and multipath effects are clearly evident as fluctuations in the Probability of Detection P_D. To examine the effects of target shadowing, it is necessary to compare the probability of detection maps for a target at lower altitude. The probability of detection maps for a target height of 150m, for both radar positions is shown in Figures 6.6(a) and (b).

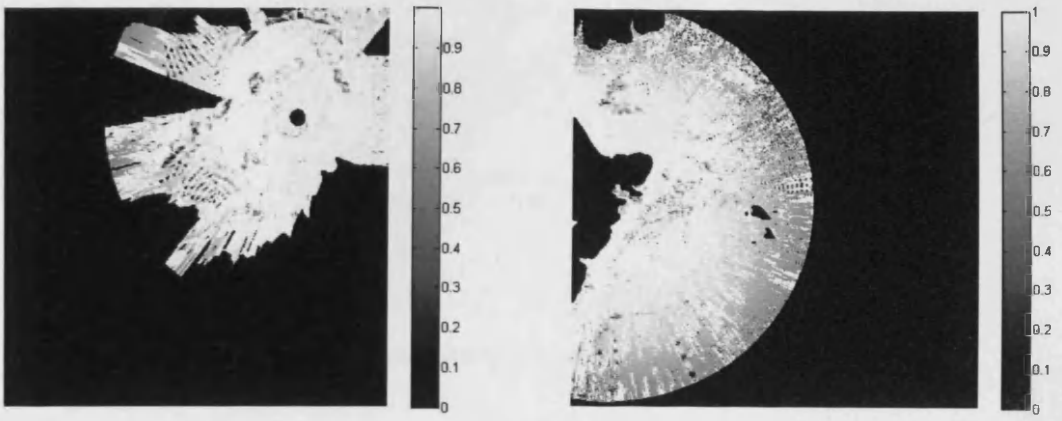

(a) (b)

Figure 6.6 Probability of Detection Map for Target Height of 150m: (a) for radar position 1; (b) for radar position 2.

Here we can observe the impact of target shadowing due to the relief of the terrain on the probability of detecting low altitude targets. For radar position 1 as shown in Figure 6.6(a), the probability of detection is greatly reduced for a considerable percentage of the radar coverage region also resulting in reduced maximum detection range. For radar position 2 as shown in Figure 6.6(b), target shadowing effects are small in comparison. We have demonstrated how the IRS can be used to predict radar performance and discriminate between good and bad solutions. An optimisation task is now necessary to determine the optimal location: but this is beyond the scope of this thesis.

6.3.2 Radar Sensor Network Deployment and Configuration

For the task of deploying a radar sensor network and joint sensor operation we consider the placement of three radar sensors to achieve optimal coverage of a surveillance region. To illustrate the advantages for this scenario we will consider the terrain visibility map, the clutter map, and the probability of detection maps for each radar position. The locations of the three radars are shown in Figure 6.7.

Figure 6.7 Topographic Map Showing Radar Positions

Radar position 1 is shown by the magenta symbol, radar position 2 is shown by the red symbol, and radar position 3 is shown by the blue symbol. Let us first consider the terrain visibility maps calculated as proposed in Chapter 5 for each radar position, as shown in Figure 6.8.

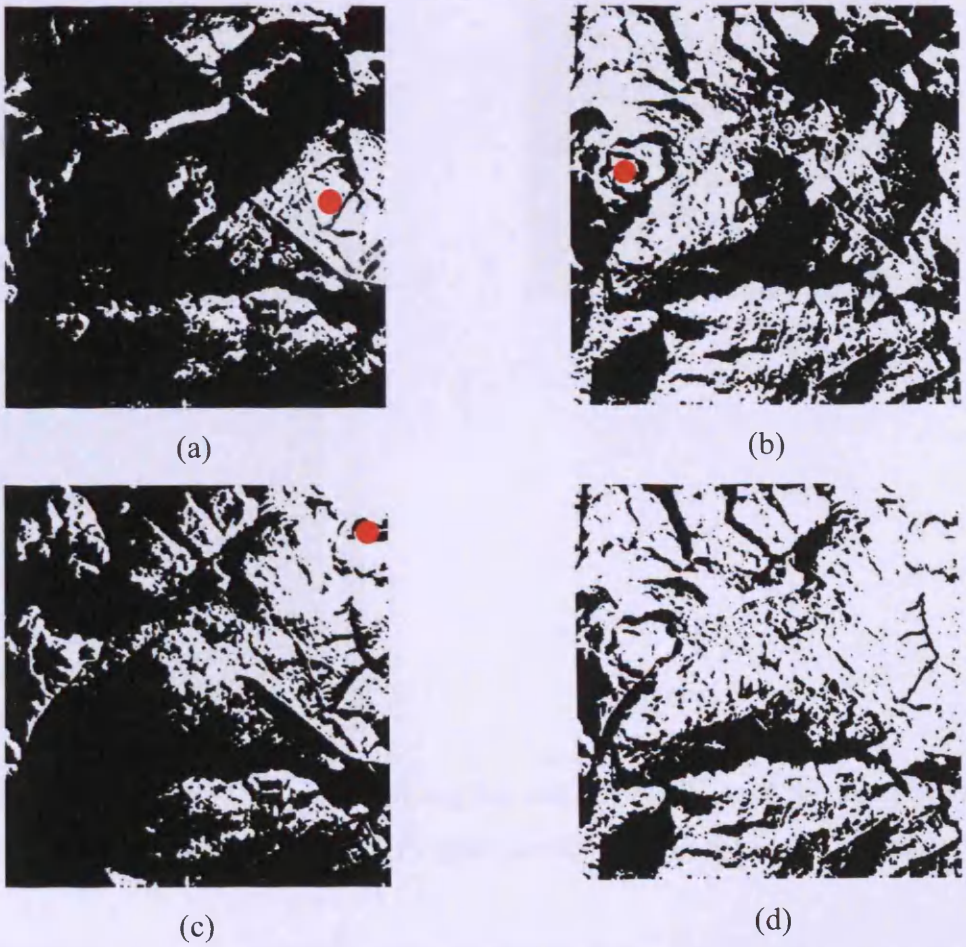

(a) (b)

(c) (d)

Figure 6.8 Terrain Visibility Map for the whole region: (a) for radar position 1; (b) for radar position 2; (c) for radar position 3; (d) for radar sensor network.

The terrain visibility maps for radar positions 1-3 are shown in Figures 6.8(a)-(c), respectively, where white represents visible terrain and black represents shadowed terrain. For radar position 1, 82.04% of the terrain is shadowed, 54.92% is shadowed for radar position 2, and 70.71% is in shadow for radar position 3. Note that although radar positions 1 and 3 have a fairly high proportion of the terrain in shadow, they have the advantage of having different areas of visible terrain which are in shadow for radar position 2. This is illustrated in Figure 6.8(d) which shows the combined terrain visibility map for all three radar positions. For the fused visibility map only 35.12% of the terrain is shadowed, resulting in better radar coverage of the region by fusion of the radar measurements from all three radars.

The clutter maps for the three radars are shown in Figure 6.9.

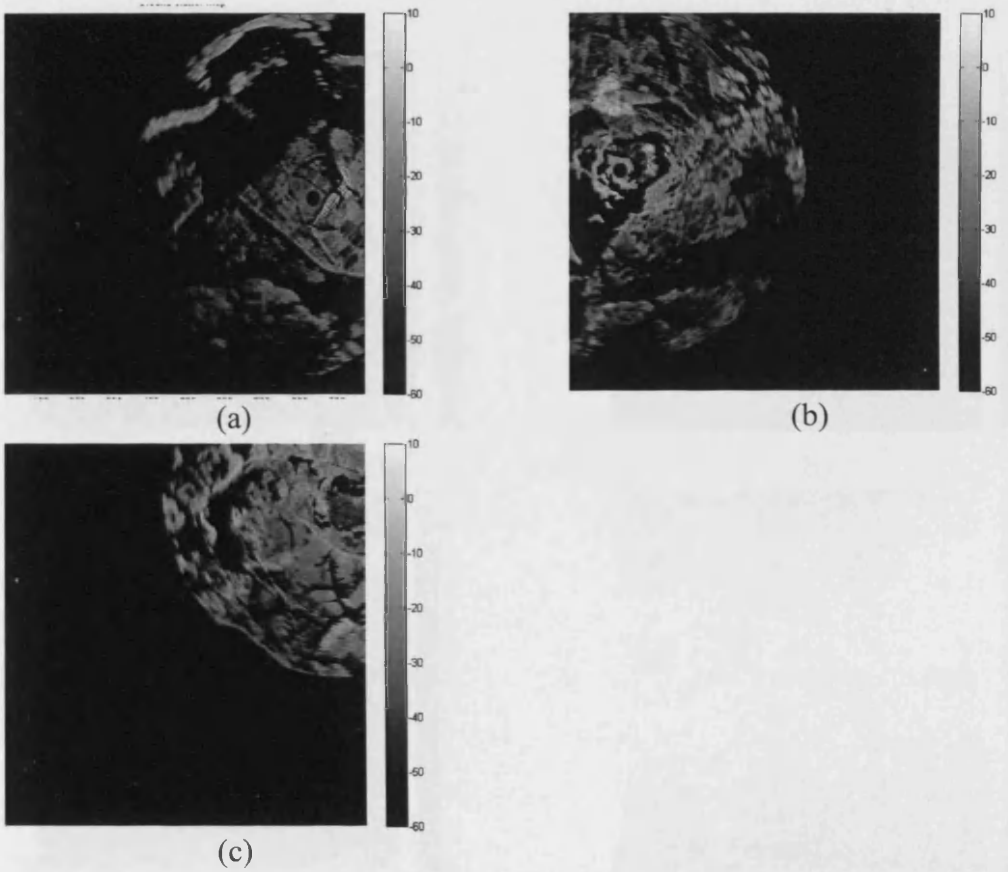

Figure 6.9 Clutter Map accounting for Antenna Pattern Characteristics: (a) for radar position 1; (b) for radar position 2; (c) for radar position 3.

The clutter maps accounting for radar system parameters such as antenna pattern and maximum detection range are shown for radar positions 1-3 in Figures 6.9(a)-(c),

respectively. These clutter maps demonstrate how clutter intensity changes significantly with radar position, different areas are cluttered for different radars. Therefore the benefit of sensor measurement fusion is that the impact of clutter can be reduced for some areas through joint sensor operation. There is no benefit in fusing the clutter maps for these three radar positions. Instead it is more appropriate to consider fusion of the probability of detection maps as this is the measure of performance for the IRS.

To assess radar performance we must now consider the radar's ability to detect targets. The probability of detection maps for the three radars and the combined probability of detection map are shown in Figure 6.10. The combined probability of detection map illustrates the case of sensor fusion where the maximum probability of detection is selected.

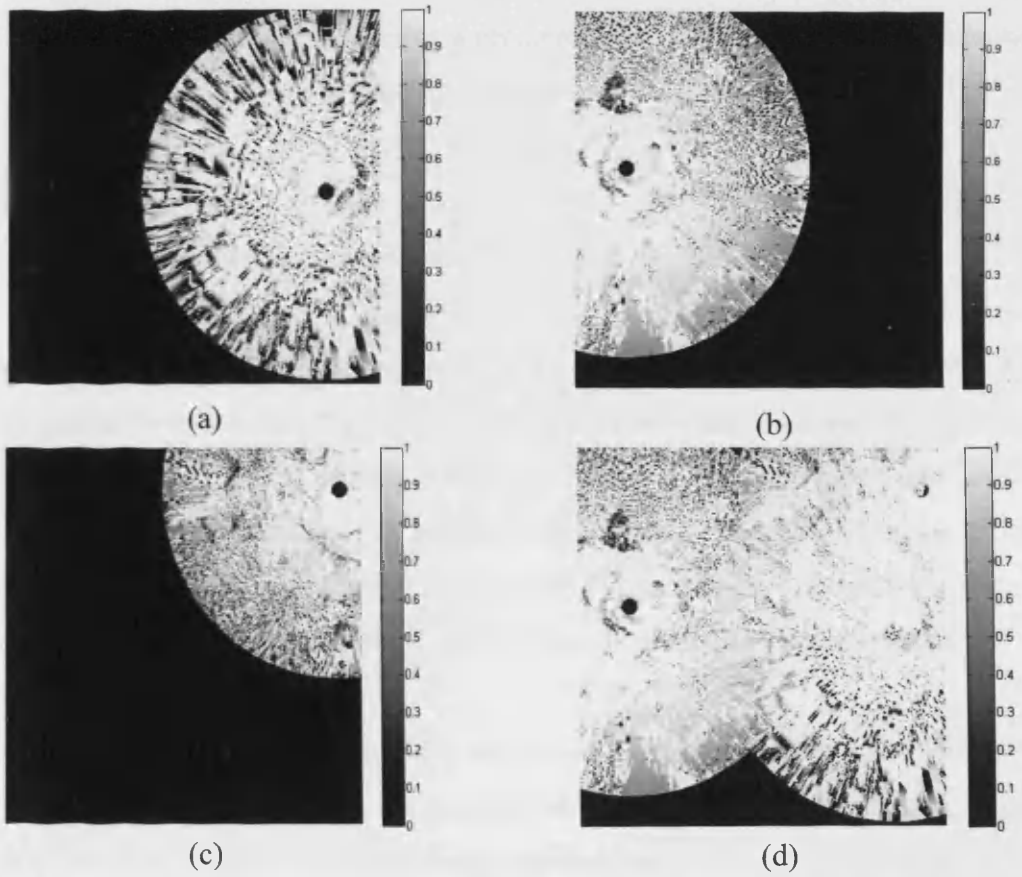

Figure 6.10 Probability of Detection Map:
(a) for radar position 1; (b) for radar position 2; (c) for radar position 3;
(d) for radar sensor network.

The probability of detection maps in Figures 6.10(a)-(c) illustrate the dependence of target detection on radar position, clutter intensity, terrain relief, and multipath propagation effects. For radar position 1, the probability of detection is reduced for many target positions due to multipath propagation effects resulting in the textured image. For radar positions 2 and 3, multipath effects are less prominent but they are still present and result in the speckle-like images. Fusion of the three probability of detection maps for the three radar positions result in the combined probability of detection map shown in Figure 6.10(d). It illustrates the benefits of radar data fusion, application of several radars, and the opportunity to apply the IRS for performance prediction of radar fusion systems.

We have shown how the IRS can be used as a planning tool to assist in deployment and fusion of radar sensor networks by predicting radar performance for all positions in the deployment region in advance. An optimisation task can then be performed to configure the radar network to achieve a predetermined joint probability of detection for the radar coverage region, or any other measure of fusion performance.

6.3.3 Mobile Radar Position and Route Prediction

For mobile radars which have the opportunity to change location, there are two issues which need to be addressed. The first is which location to move to, and the second is which route to take to get there whilst maintaining efficient operation during measurements. For this scenario we assume that we know the start and end positions of the radar. The task is to determine which route to take and how the IRS can help to decide. Figure 6.11 shows the clutter maps for the radar start and end positions.

It has been predetermined that the radar will move from the position indicated by the blue symbol in Figure 6.11(a), to the position indicated by the blue symbol in Figure 6.11(b). The next step is to predict radar performance for any possible route and determine the optimal route between these positions. However, this is an optimisation task and it is beyond the scope of this thesis: only the task of predicting sensor performance for any position of the route is considered. Therefore, we consider the simple radar route shown by the red line in Figures 6.11(a) and (b), to demonstrate

how the IRS approach can be applied. Note that in Figure 6.11(a) the track has been obscured by the base of the radar symbol.

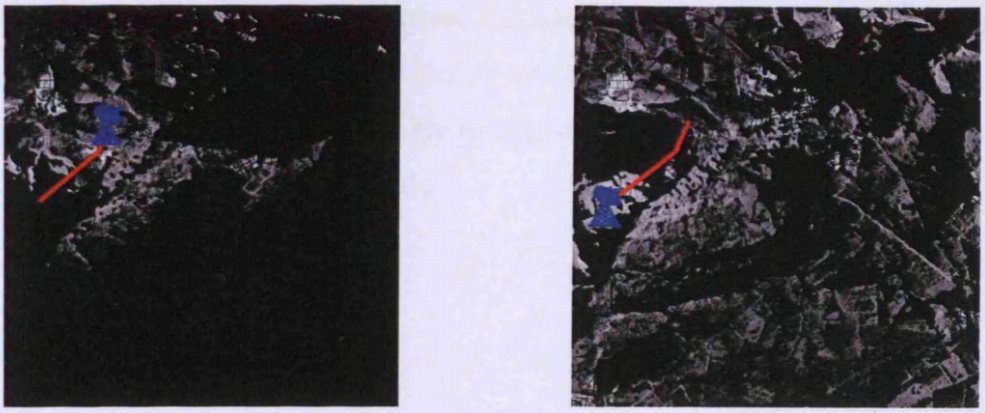

(a) (b)

Figure 6.11 Clutter Map:
(a) for radar start position; (b) for radar end position.

We need to calculate the clutter map variations when the radar is moving. The clutter map is predicted for each position along the radar path. The measure of performance for the IRS is gauged by the probability of detection map. However, for this scenario we will concentrate on the clutter map because it better demonstrates the advantages of the considered approach, and more clearly illustrates terrain shadowing effects which reduce the visibility of the radar for low-angle targets.

An animation has been produced, showing the clutter map for each position as the radar moves between the start and end positions along the red track in Figures 6.11(a) and 6.11(b). This animation is included in Appendix 4 on a DVD (Digital Versatile Disc) in AVI (Audio Video Interleave), MP4 and WMV (Windows Media Video) file format for playback on any standard software which supports AVI, MP4, or WMV video files.

Examination of the radar route animation illustrates how significantly clutter and terrain visibility can vary as the radar position changes. Total shadowed areas for the positions in the radar route range from a minimum of 53.65% to a maximum of 96.07%. Improper selection of radar position could render the radar blind to low-altitude targets which may be shadowed by terrain. This observation highlights the

necessity for intelligent selection of the radar route to maximise radar performance whilst manoeuvring between positions due to significant variation of clutter intensity between time intervals. Therefore, the advantage of the IRS has been demonstrated not only for selection of radar position, but also for improved prediction of radar route, which enables on-the-fly prediction of radar performance for the next time steps. Using this approach, it is feasible to improve the selection of radar positioning and determine an optimised radar route.

6.4 Conclusions

In this chapter three scenarios have been identified for which the IRS approach can be implemented to provide some advantages. The scenario considered in 6.3.1 has demonstrated the necessity for site-specific clutter prediction and shown how the IRS can be used to deploy a radar sensor. The scenario considered in 6.3.2 has shown how the IRS can be used to configure a radar sensor network and demonstrated the advantages of radar data fusion by fusing probability of detection maps for three radar positions. The scenario considered in 6.3.3 has shown how IRS can be used to plan a route for a mobile radar sensor.

These three scenarios illustrate the problematic nature of radar deployment and placement. The difficulty in optimal positioning of radar sensors is compounded by the fact that it is not only probability of detection that needs to be maximised, but also consideration must be given to other factors such as terrain shadowing, minimum target detection height, and minimum detectable target RCS (due to clutter intensity and multipath effects). This observation indicates the complexity of the optimisation task which requires optimisation of several cost functions each involving many variables.

All three scenarios identified the following effect on radar performance. Terrain shadowing reduces clutter impact, meaning that higher altitude targets (targets not shadowed by terrain) are easier to detect. However, low-altitude targets may be shadowed by terrain and would be harder to detect. Therefore, these factors must be considered when assessing radar performance.

There is still a considerable amount of work left to be done until fully autonomous sensors that can react to dynamic environments in an intelligent manner can be realised. The IRS approach adopted in this thesis has shown how modelling techniques can be applied to predict radar sensor performance. However, for truly intelligent systems optimisation is an essential ingredient to enable autonomous sensor operation. The problems associated with optimisation for the scenarios considered have been identified and are a topic for future research. Some suggestions for future work are now discussed in the next chapter.

Chapter 7

Conclusions and Future Work

This thesis advances the field of intelligent radar sensor design by using a new modelling approach to predict radar sensor performance. Through unification of established modelling techniques for radar sensor modelling and multipath propagation modelling, combined with the development of a new technique for modelling land clutter, a new approach for predicting radar sensor performance has been developed which has advanced knowledge in the intelligent radar sensor domain. Particular attention has been paid to applications that can achieve some advantages from this intelligent sensor approach. Original contributions have been made in the proposal of the intelligent radar sensor architecture, and development of a new method for predicting land clutter based on fusion of remote sensing data and application of empirical land backscattering models. Additionally, methods have been proposed for mitigating impairments in remote sensing data. A new multiresolution method based on the Discrete Cosine Transform (DCT) and Laplacian pyramid transform has been proposed for simultaneously reducing speckle noise and fusing Synthetic Aperture Radar (SAR) and Side Looking Aperture Radar (SLAR) images. Robustness studies have also been conducted for several non-linear algorithms which have been proposed as alternatives to the standard linear algorithm used for SAR image synthesis, to remove impulse noise caused by data transmission errors.

We will now summarise the contributions and observations made in each chapter in Section 7.1. This will be followed by a discussion which identifies topics for future work in Section 7.2.

7.1 Summary and Conclusions

In Chapter 1, we discussed the motivating factors for developing an intelligent radar sensor, identifying the various impairments for surface-sited low-grazing angle radar

and discussing the importance of mitigating these impairments. One of the motivating factors concerned the development of sensor communication and data sharing frameworks such as the Global Information Grid (GIG) and Network Enabled Capability (NEC) which enable real-time on-demand sharing and communication between heterogeneous sensors. This is an important issue because the availability and acquisition of up-to-date remote sensing data is a vital component of the intelligent radar sensor approach presented in this thesis, which permits adaptation to changes in the environment. In the background section we discussed various impairments of surface-sited radar, paying particular attention to effects of land clutter and radiowave propagation on radar performance. This discussion was then followed by a literature survey which concentrated on the development of intelligent radar systems, concentrating particularly on Space-Time Adaptive Processing (STAP) applications and how *a priori* information about the environment is incorporated to predict various sources of impairments and then remove them by modifying the signal processing chain in order to improve radar sensor performance. The reason for concentrating on these STAP applications is the fact that the radar research community has primarily focused on utilising terrain information in this area. Two approaches have been discussed; Knowledge-Based (KB) systems and Knowledge-Aided (KA) systems. Although both use terrain information to improve radar sensor performance, they differ in their architectures. This review highlighted a number of opportunities for researching problems which can be solved using a data fusion approach. We then indicated how data fusion and modelling approaches might be utilised to solve these problems. The novel contributions developed in this thesis can be summarised as follows:

- A new Intelligent Radar Sensor architecture
- A new method for modelling land clutter for surface-sited radar
- Impairment mitigation and fusion of SAR/SLAR data
- A new multiresolution method based on DCT and Laplacian pyramid transform for denoising and fusion of SAR/SLAR data

The Intelligent Radar Sensor architecture was presented in Chapter 2, while the other three novel contributions were considered in Chapter 5.

Chapter 2 proposed the new architecture for the Intelligent Radar Sensor which uses *a priori* knowledge and a modelling approach to predict radar performance. A brief discussion concerning what constitutes intelligence with respect to intelligent sensor systems preceded the discussion on the intelligent radar sensor architecture. Initially, a new architecture for the Intelligent Radar Sensor was proposed which included elements of learning, optimisation, and a KB. This architecture was then simplified to concentrate on the specific components relevant for the scenarios considered in this thesis. The main components are the radar model, the terrain model, the clutter model, and the multipath propagation model. The terrain model utilises information provided by other sensors and sources which is required for predicting radar performance. The radar model is necessary to model all aspects of the radar sensor and predict radar performance. The clutter model and multipath propagation model are required for modelling and predicting site-specific factors which degrade radar sensor performance. Implementation of these model components was discussed in sufficient detail to enable assessment of radar performance.

Chapter 3 addressed the issue of modelling the radar sensor and the operation of the radar model within the intelligent radar sensor to predict the radar's own performance. The impact of multipath propagation and land clutter factors on radar performance were discussed. These effect the detection of targets and cause deterioration of radar performance. Measures of performance were discussed and it was decided that the probability of detecting targets was the most appropriate measure for the intelligent radar sensor proposed in this thesis because the objective was to predict the performance of the radar in detecting targets. The components of the radar model were identified and elaborated in detail including the radar configuration, radar equation (which describes the relationship between radar characteristics, the target, and the received signal), radar antenna model, and the detection model. The chapter concluded with a demonstration of how the radar model and clutter model can be combined to predict radar performance. At this point multipath effects were ignored for simplification purposes. Using measured data the probability of detection map was then produced.

In Chapter 4, the impact of multipath propagation of radiowaves on radar performance and target detection was considered. Multipath propagation is one of the

most important non-free-space effects for low-grazing angle radar. The problem with multipath propagation is that it leads to constructive and destructive interference at the radar receiver. This has the effect of either increasing or decreasing the vector sum signal, respectively. This has both advantages and disadvantages. For the case where the vector sum of the signal is increased, this leads to an increase in the probability of detection and also an increase in the maximum detection range. However, when the vector sum of the signal is decreased, the probability of detection is reduced. Multipath effects depend strongly on terrain characteristics such as the electrical properties of the surface (dielectric constant and conductivity of the reflecting surface), surface roughness, terrain type, and the geometry. These observations highlight the necessity for modelling multipath effects when predicting radar performance.

Chapter 5 contains three novel contributions: site-specific land clutter prediction for low-grazing radar; modelling, fusion and mitigation of SAR remote sensing data; and a new method for fusing and denoising of SAR/SLAR remote sensing data. This chapter primarily focuses on modelling land clutter through fusion of remote sensing data and application of an empirical land backscattering model. Standard methods for modelling land clutter which adopt a statistical or experimental approach were reviewed. The advantages and limitations of each method were discussed. Additionally, attention was paid to how site-specific prior knowledge can be incorporated into these methods to improve the accuracy of predicting land clutter. The new method for predicting land clutter proposed in this chapter employs remote sensing data to estimate land surface parameters such as local grazing angle, and land surface type. The major contribution lies, however, in the application of radar remote sensing data to provide direct Radar Cross Section (RCS) measurements of the land surface - but for grazing angles very different from those associated with the surface-sited radar. The remote sensing radar data is used to estimate the intensity of land clutter while the backscattering model is applied to correct only for angular and frequency dependencies.

The new method for predicting land clutter can be considered as a three stage approach. The first stage involves pre-processing of the remote sensing data to remove impairments, correct for geometric distortions, and geometrically register all

data to a common coordinate system. Additionally, for the radar remote sensing data, calibration was required to convert the measurements to absolute values of the direct backscattering coefficient σ^0 and remove radar sensor dependencies from the measurements. The second stage involves estimation and extraction of terrain characteristics from the remote sensing data including local grazing angle, land surface type, and terrain shadowing effects. Finally, the third stage is fusion of the terrain data provided by the remote sensing system, and then application of the empirical land backscattering model to predict land clutter intensity.

Measured data was used to illustrate this new approach for predicting land clutter. The results obtained were then compared to those obtained when using only the land backscattering model (without application of the radar remote sensing data). The comparison indicated that the new method predicts higher intensity for some regions, and also that fluctuations are present for bare soil and urban regions, that are not observed when the backscattering model is applied on its own. Therefore, it has been shown that lack of information about the environment can produce underestimation of land clutter intensity in some cases. The advantage of this new approach is that application of remote sensing data can provide up-to-date information about the environment and improve clutter prediction accuracy by accounting for variations and changes in the environment. Remote sensing data may contain impairments which destroy valuable information and if they are not removed they will reduce the accuracy of clutter prediction. Therefore, it is important to mitigate any impairments in the data prior to use for clutter modelling. This is true for all data sources including DEM, topographic map, and optical data. However, the datasets used for these sources of information were considered to not contain significant errors. Radar remote sensing data is a major source of information for clutter modelling as it provides measurements of the direct backscattering coefficient σ^0. Mitigation of impairments in radar remote sensing data was considered in this chapter, concentrating on SAR and SLAR.

The second novel contribution in Chapter 5 is the evaluation of techniques for mitigating impulse noise impairments from SAR data and assessing the impact on fusion results. The impulse noise present in the SAR data is a result of data

transmission errors, and was removed at the stage of image synthesis. The non-linear α-trimmed estimate was considered as an alternative to the standard linear algorithm (which is optimal for the case of additive Gaussian noise but not for non-Gaussian impulse noise). This part of the work has shown how fusion results can be improved by mitigating impairments at the first stage, then applying *standard* fusion algorithms. This approach has the advantage of not having to modify or complicate fusion algorithms. Robustness studies have shown that improvements of up to 8dB in the SNR can be obtained using the α-trimmed method for removal of impulse noise impairments in SAR data.

The third novel contribution in Chapter 5 is a new DCT-based multiresolution method for simultaneously reducing speckle noise and fusing of SAR/SLAR data. Standard filtering techniques based on the local statistics of noise for speckle noise reduction were briefly discussed. The discussion identified techniques which performed well for noise suppression and texture preservation, but not so well for homogenous regions. Combining the Laplacian pyramid transform and a sliding window DCT results in a multiresolution technique that has good signal localisation properties in both the spatial and frequency domain. This technique is then suitable for both fusion and denoising. Comparisons were made to the Discrete Wavelet Transform (DWT) and the Dual-Tree Complex Wavelet (DTCWT), and the new technique has been shown to outperform both methods for textured regions in particular. It was also observed that for fusion better results were obtained when using smaller DCT window sizes, but for denoising better results were obtained for larger DCT windows. Thus, this technique offers the opportunity for optimising the window size for the particular situation; but this aspect of the work was not pursued.

In conclusion, Chapter 5 demonstrated how remote sensing data can provide information about the terrain to allow improved prediction of land clutter intensity for site-specific clutter modelling. Additionally, the importance of removing impairments in remote sensing data, in particular, radar data, was also discussed and demonstrated using measured data.

Chapter 6 developed the intelligent radar sensor architecture proposed in Chapter 2 for three scenarios. The three scenarios considered were deployment of a single radar

sensor, deployment of a network of radar sensors, and a single mobile radar sensor. After a discussion on how the intelligent radar sensor can be applied to solve the problems encountered in each individual scenario, measured data was used to explore the performance of the intelligent radar sensor for these three scenarios. The scenarios identified problems associated with various aspects of predicting radar performance. For the task of radar sensor deployment it was noted that the difference between a 'good' and 'bad' radar position not only depends on the probability of detecting targets, but also on additional factors such as target visibility due to terrain shadowing effects. For the radar sensor network scenario we have shown how the intelligent radar sensor can be applied to predict radar performance, and consequently, how this information could be used to position networks of radar sensors for optimal radar coverage of the region and fusion of radar measurements. The third scenario addressed the problem of route planning for mobile radar applications. For this scenario we concentrated on the clutter map which illustrated how clutter intensity and terrain visibility varied significantly with changing radar position. This observation reinforced the advantages of applying the intelligent radar sensor approach to improve selection of radar positioning and determining optimal radar routes.

7.2 Lessons Learned

In this section we will briefly review the lessons that have been learned about intelligent radar sensor modelling.

This thesis has proposed an architecture for an intelligent radar and has concentrated on the cognitive aspects of such a system. The cognitive functions of the intelligent radar sensor are very important and underpin the foundations of an intelligent system. The author now acknowledges that the difficulty of the cognitive aspects of the Intelligent Radar Sensor was initially severely underestimated. Therefore, the next logical step is to extend and enhance cognition by considering environmental effects in greater depth, such as, atmospheric ducting and volume clutter both of which have been ignored in this thesis for the sake of tractability.

Radiowave propagation modelling proved to be extremely computationally expensive even when using only a simplified two-path model for multipath. This issue could affect the real-time application of the Intelligent Radar Sensor which would be further compounded by the tasks of optimisation and learning. We could have compromised on the fidelity of the model but this would have reduced the accuracy of the model. However, even though this may be undesirable, it may be justified to utilise lower fidelity models to ensure real-time application if some benefits are still attainable.

Optimisation was not considered in this thesis due to the complexity of this task and time limitations. However, a fairly straightforward optimisation task could be considered such as the scenario in Chapter 6 Section 6.3.2. Here three radar positions were manually selected; however, an optimisation task could be to automatically determine the three radar positions by optimising terrain visibility and the average clutter intensity for those visible regions. It is the authors' view that this is probably the next logical step in the progression of the Intelligent Radar Sensor.

The Intelligent Radar Sensor system may not be realisable using current hardware due to the computational complexity of just the cognitive aspects of such a system. However, the cognitive radar may be attainable, and therefore, maybe cognition should be aimed for in the first respect as this underpins the intelligent system. The author would like to point out, however, that the truly intelligent radar requires the capability of self-optimisation and the ability to learn from previous experiences.

7.3 Future Work

In this final section a few suggestions for future work are given. There are many minor possibilities for future work but they do not warrant attention. Instead, we will concentrate on the more interesting topics that are either new directions for the research conducted in this thesis, or areas of the research which time did not permit to be explored.

Let us first consider topics of future work for the intelligent radar sensor as a whole.

Throughout this thesis we have been concerned with predicting radar performance based on the probability of detection. The scenarios we considered focused on positioning of radar sensors either for deployment of single sensors, networks or radar sensors, or for moving radar applications. Either way, the goal has been to employ the intelligent radar sensor approach to determine the most appropriate position to position the radar.

Another approach is to optimise radar parameters such as radar height, selection of radar waveform, frequency or transmitter power, to name just a few possibilities. For the case when a radar sensor has the ability to change these parameters, the intelligent radar sensor approach can be applied to predict radar performance for each mode of operation, in order to optimise radar system parameters. Additionally, this approach could be combined with the tasks considered in this thesis, to optimise both radar position and configuration. Therefore, future work could consider the task of applying the intelligent radar sensor approach for total configuration of all applicable radar parameters to achieve optimal radar performance. This would provide a valuable tool for planning, deployment, and configuring radar sensors.

Two important components of the intelligent radar sensor have not been addressed in this thesis. These are optimisation and learning. As discussed in the earlier chapters, these concepts are essential ingredients for truly intelligent sensors. Each of these tasks requires considerable attention and each task has significant problems to be solved.

Let us first consider optimisation. In this thesis we have shown how the intelligent radar sensor approach can be applied to predict radar sensor performance for any position within the radar deployment region. Now that we can achieve this, the next problem is how to select the optimal solution from the set of all possible solutions. This task is problematic in that we have two issues which need to be addressed. Firstly, we need to define measures to describe what constitutes the optimal solution. We have used the probability of detection in this thesis, but the discussion in Chapter 6 has highlighted various problems associated with radar performance assessment; such as terrain shadowing effects, which if not considered could render the radar blind to low-altitude terrain-following targets. Therefore, research must be conducted to

determine the additional measures which must be considered when attempting to assess radar performance. These measures could well be very specific to the mission that the radar is being deployed to support. The second issue is how we can develop optimisation algorithms based on these measures of performance to determine the optimal solution from all possible solutions. This is likely to involve large computational resources and it is important not to underestimate the complexity of this task.

The learning component of the intelligent radar is another opportunity for future work. To illustrate the importance of this task, let us consider the mobile radar scenario discussed in Chapter 6. Learning could enhance the prediction of radar performance in the following way. The intelligent radar sensor would predict the clutter map accounting for radar characteristics for the next radar position. Then when the radar moves to this position, it would take direct measurements. The measured clutter map could then be compared to the predicted clutter map to assess errors and differences between the predicted results and the measured results. The intelligent radar can then use this acquired knowledge to learn and improve future predictions. Using this approach could allow the radar to improve the prediction of clutter maps over time. Additionally, the clutter map acquired in this way could be used to assist in prediction of clutter maps for near positions (positions spatially close to the current radar position). It is not immediately clear how to implement learning for this purpose and this is where the research problem lies.

Another aspect that this thesis has ignored is the assessment of model errors due to impairments or inaccuracies in the remote sensing data used for the intelligent sensor. These errors obviously impact on the results of modelling. For example, errors in the DEM data lead to inaccurate grazing angle estimation; errors in the optical/multispectral data used for terrain classification lead to misclassification errors; remote sensing radar data errors or impairments lead to errors in the estimation of RCS, and also we have errors in the land backscattering model. It is important to consider the impairments in each of these sources and the effects they have on the estimation of vital parameters. Additionally, these errors are propagated through to the clutter model, multipath model, and radar model, which are used to assess radar performance. Therefore, the impact of these errors must be considered here also. If we

can model, measure, and predict these errors then we can mitigate and correct them, to improve the prediction of radar performance.

Another important unanswered question is how viable is it to implement the intelligent radar sensor approach in hardware, software, or a combination of both, given the current limitations imposed by hardware speed, memory capacity, and storage capacity? Two opportunities naturally arise from this. The first opportunity exists in implementation of the intelligent radar sensor using Digital Signal Processor (DSP) [112] or Field Programmable Gate Array (FPGA) devices [113], for real-time or near real-time operation. The problem becomes: can the intelligent radar sensor be implemented on either of these platforms given state-of-the-art memory and storage restrictions, and also can it work in real-time?

The second opportunity which warrants investigation is how we can take advantage of high powered graphics processing units (GPU) [114] which have been extensively developed in terms of both speed and memory, for high-end gaming applications. These GPU architectures benefit from dedicated hardware for 3D manipulation of data, which could support geometric calculations for the intelligent radar sensor and greatly reduce the complexity of implementation.

Clearly, these two avenues need to be explored to assess hardware implementation of an intelligent radar sensor using current technology, and to evaluate how far away we actually are from hardware realisation of intelligent sensor systems.

The clutter model is an essential component of the intelligent radar sensor, and opportunities exist here also. Let us now consider possible directions for future work in this domain.

The accuracy of clutter map prediction in this thesis depends on the accuracy of the remote sensing data and the land backscattering model. The most important source of information for predicting the clutter map in this thesis is the remote sensing radar which provides an estimate of the RCS of the land surface clutter (the backscattering model and other remote sensing data are only used to correct for angular and frequency dependencies). Certain scatterers within the environment exhibit an

anisotropic nature. Examples are rows of planted crops, bare soil furrows, and irregular buildings. Therefore, the opportunity exists to improve estimation of RCS for non-isotropic scatterers by fusion of remote sensing radar data – but to do this multiple sensor trajectories are required.

Another task which needs to be addressed is assessment of clutter map accuracy by comparison against actual radar measurements. This can only be achieved by obtaining ground truth data measured across various sites to validate this approach. This issue has not been addressed in this thesis as it requires access to actual radar facilities which are not available to our research group. It also depends on obtaining remote sensing data for each deployment site.

In this thesis we have also considered fusion and mitigation of impairments for SAR/SLAR data. Based on the results of the Multiresolution Discrete Cosine Transform (MRDCT) experiments, we have another possibility for future research; however, it is less significant than the previous suggestions. An observation was made during the development of the MRDCT which revealed that for fusion only (fusion without denoising) better results were obtained using smaller sized DCT sliding windows, but for denoising better results were obtained for larger sized DCT windows. This naturally gives rise to the opportunity for further optimisation of this MRDCT technique by using a variable DCT window size. This then presents the problem of how to determine the optimal window size. Future work could involve analysis of the data to determine which window sizes are most appropriate for various data types such as textured and homogenous regions, and to examine the influence of impairments of varying intensity.

References

[1] http://difdtc.gdstorm.org.uk, last accessed on 29th September 2008.

[2] T. Westra, K.C. Mertens and R.R. De Wulf, "Wavelet-based fusion of SPOT/VEGETATION and ENVISAT/ASAR Wide Swath data for wetland mapping", International SPOT/VEGETATION Users Conference, Antwerp, Belgium, March 2004, pp. 24-26.

[3] T. Toutin, A. Redmond, E. Hoeppner, D. Hoja, C. King, "RADARSAT and DEM Data Fusion for 3D Visualisation Over the Reunion Island for Geoscientific Applications", Symposium Fusion of Earth Data: merging point measurements, raster map and remotely sensed images, Antipolis, France, January 28-30, 1998, pp. 75-84.

[4] A. N. Steinberg, C. L. Bowman and F. E. White, "Revisions to the JDL Data Fusion Model", Proceedings of SPIE AeroSense (Sensor Fusion: Architectures, Algorithms and Applications III), Orlando, Florida, USA, 1999, pp. 430-441.

[5] "Guidance for Implementing Net-Centric Data Sharing", Department of Defense (DoD), Directive number 8320.2-G, April 12, 2006.

[6] "Global Information Grid - Overarching Policy", Department of Defense (DoD), Directive number 8100.01, September 2002.

[7] "Department of Defense (DoD) Global Information Grid (GIG) Computing", memo: http://www.dtic.mil/whs/directives/corres/pdf/dsd010406gig.pdf, last accessed on 29th September 2008.

[8] D.J. Russell, J. Xu, "Service-Oriented Architectures for Network Enabled Capability", University of Leeds: www.comp.leeds.ac.uk/NEC/doc/Service-orientedArchitecturesforNEC.pdf, last accessed on 29th September 2008.

[9] http://www.army.mod.uk/equipment/equipment.aspx, last accessed on 29th September 2008.

[10] D.J. Russell, N. Looker, J. Xu, "SOA-Dependability Measures and Metrics for Network Enabled Capability", Forum on Capability Engineering - At Home and Abroad, 7 November 2006, Savoy Place, London, UK.

[11] E.V. Tarnavsky, G.P. Kulemin, "Modeling of radar land clutter map for small grazing angles", Proceedings of SPIE The International Society For Optical Engineering, USA, 2004, Volume 5484, pp. 702-706.

[12] K.H. Craig, M.F. Levy, "Parabolic equation modelling of the effects of multipath and ducting on radar systems", IEE Proceedings of Radar and Signal Processing, Volume 138, Issue 2, April 1991, pp. 153-162.

[13] C.C. Lin, J.P. Reilly, "A Site-Specific Model of Radar Terrain Backscatter and Shadowing", Johns Hopkins APL Technical Digest, Volume 18, Issue 3, 1997, pp. 432-447.

[14] M. Denny, "Refracted propagation effects for airborne radar", The Record of the IEEE 2000 International Radar Conference, Alexandria, VA, USA, May 2000, pp. 554-559.

[15] V.C. Vannicola, "Expert system for sensor resource allocation", Proceedings of the 33rd Midwest Symposium on Circuits and Systems, Volume 2, 12-14 August 1990, pp. 1005-1008.

[16] V.C. Vannicola, J.A. Mineo, "Applications of knowledge based systems to surveillance", Proceedings of the 1988 IEEE National Radar Conference, 20-21 April 1988, pp. 157-164.

[17] S. Haykin, "Radar vision", Second International Specialist Seminar on the Design and Application of Parallel Digital Processors, 15-19 April 1991, pp. 75-78.

[18] W. Baldygo, M. Wicks, R. Brown, P. Antonik, G. Capraro, and L. Hennington, "Artificial intelligence applications to constant false alarm rate (CFAR) processing", Proceedings of IEEE 1993 National Radar Conference, Boston, MA, April 1993, pp. 275-280.

[19] M.C. Wicks, W.J. Baldygo, and R.D. Brown, "Expert system constant false alarm rate (CFAR) processor", U.S. Patent 5 499 030, 12 March 1996.

[20] W. Melvin, M. Wicks, P. Antonik, Y. Salama, Li Ping, H. Schuman, "Knowledge-based space-time adaptive processing for airborne early warning radar", IEEE Aerospace and Electronic Systems Magazine, Volume 13, Issue 4, April 1998, pp. 37-42.

[21] C.T. Capraro, G.T. Capraro, D.D. Weiner, and M. Wicks, "Knowledge based map space time adaptive processing (KBMapSTAP)", in Proceedings of 2001International Conference on Imaging Science, Systems, and Technology, Las Vegas, Nevada, June 2001, pp. 533-538.

[22] "Knowledge base applications to adaptive space-time processing", AFRL-SN-TR-2001 Final Technical Report, volume I, July 2001.

[23] G. Capraro, W. Baldygo, R. Day, J. Perretta, and M. Wicks, "Autonomous intelligent radar system (AIRS) for multi-sensor radars", 2005 1st IEEE International Workshop on Computational Advances in Multi-Sensor Adaptive Processing, 13-15 December 2005, pp. 16-19.

[24] J.R. Guerci, "Knowledge-Aided Sensor Signal Processing and Expert Reasoning", in Proceedings 2002 Knowledge-Aided Sensor Signal Processing and Expert Reasoning (KASSPER) Workshop, Washington DC, 3 April 2002,

[25] G.E. Schrader, "The knowledge aided sensor signal processing and expert reasoning (KASSPER) real-time signal processing architecture", Proceedings of the IEEE Radar Conference, 26-29 April 2004, pp. 394-397.

[26] W.L. Melvin, G.A. Showman, J.R. Guerci, "A knowledge-aided GMTI detection architecture", Proceedings of the IEEE Radar Conference, 26-29 April 2004, pp. 301-306.

[27] C. Capraro, G. Capraro, D. Weiner, M. Wicks, and W. Baldygo, "Improved STAP performance using knowledge-aided secondary data selection", Proceedings of 2004 IEEE Radar Conference, Philadelphia, PA, April 2004, pp. 361-365.

[28] E. Conte, A. De Maio, A. Farina, G. Foglia, "Design and analysis of a knowledge-based radar detector", 2005 IEEE International Radar Conference, 9-12 May 2005, pp. 387-392.

[29] A. De Maio, A. Farina, and M. Wicks, "KB-GLRT: exploiting knowledge of the clutter ridge in airborne radar", IEE Proceedings of Radar, Sonar and Navigation, Volume 152, Issue 6, 9 December 2005, pp. 421-428.

[30] S. Haykin, "Cognitive radar: a way of the future", IEEE Signal Processing Magazine, January 2006, Volume 23, Issue 1, pp. 30-40.

[31] A. Farina, H. Griffiths, G. Capraro, and M. Wicks, "Knowledge-based radar signal and data processing", NATO RTO Lecture Series, SET-063, August 2005.

[32] G.T. Capraro, A. Farina, H. Griffiths, and M.C. Wicks, "Knowledge-Based Radar Signal and Data Processing – A tutorial overview", IEEE Signal Processing Magazine, January 2006, Volume 23, Issue 1, pp. 18-29.

[33] J.R. Guerci, E.J. Baranoski, "Knowledge-aided adaptive radar at DARPA: an overview", IEEE Signal Processing Magazine, Volume 23, Issue 1, January 2006, pp. 41-50.

[34] M.C. Wicks, M. Rangaswamy, R. Adve, T.B. Hale, "Space-time adaptive processing: a knowledge-based perspective for airborne radar", IEEE Signal Processing Magazine, Volume 23, Issue 1, January 2006, pp. 51-65.

[35] W.L. Melvin, J.R. Guerci, "Knowledge-aided signal processing: a new paradigm for radar and other advanced sensors", IEEE Transactions on Aerospace and Electronic Systems, Volume 42, Issue 3, July 2006, pp. 983-996.

[36] J.R. Guerci, "Next Generation Intelligent Radar", IEEE Radar Conference, 17-20 April 2007, pp. 7-10.

[37] G.P. Kulemin, E.A. Goroshko, E.V. Tarnavsky, "Land Backscattering Model for Millimeter Wave Radar", TCSET'2004 Int. Conf. on Modern Problems of Radio Engineering, Telecommunications and Computer Science, Lviv-Slavsko, Ukraine, February 2004, pp. 138-141.

[38] A. Kurekin, D. Radford, G. Kulemin, K. Lever, D. Marshall, "Site-Specific Land Clutter Modelling by Fusion of Radar Remote Sensing and Terrain Data", Submitted to Journal on Information Fusion, Elsevier, (responding to referees comments).

[39] S.G. Mallat, "A theory for multi-resolution signal decomposition: the wavelet representation", IEEE Transactions on Pattern Analysis and Machine Intelligence, Volume 11, Issue 7, 1989, pp. 674-693.

[40] N.G. Kingsbury, "Image processing with complex wavelets", Philosophical Transactions: Mathematical, Physical and Engineering Sciences, Volume 357, Issue 1760, 1999, pp. 2543-2560.

[41] A. Kurekin, D. Marshall, D. Radford, K. Lever, and V. Lukin, "Robust Processing of SAR Hologram Data to Mitigate Impulse Noise Impairments", ISIF and IEEE Information Fusion 2005 Conference, Philadelphia, USA, July 2005.

[42] D. Radford, A. Kurekin, D. Marshall, K. Lever, "A New DCT-based Multiresolution Method for Simultaneous Denoising and Fusion of SAR Images", ISIF and IEEE Information Fusion 2006 Conference, Florence, Italy, July, 2006.

[43] P.J. Burt, E.H. Adelson, "The Laplacian pyramid as a compact image code", IEEE Transactions on Communications, 1983, 31, pp. 532-540.

[44] Department of Defense, *Joint Publication 1-02, Department of Defense Dictionary of Military and Associated Terms*, 12 April 2001, (as amended through 26 August 2008), pp. 270.

[45] A. Kurekin, A. Dolia, D. Marshall, V. Lukin, K. Lever, "Mitigation of Image Impairments for Multichannel Remote Sensing Data Fusion", SPIE Defense and Security Symposium, Orlando, Florida, USA, March, 2005, pp. 145-156.

[46] R. Bürgmann, P.A. Rosen, E.J. Fielding, "Synthetic Aperture Radar Interferometry to Measure Earth's Surface Topography and Its Deformation", Annual Review of Earth and Planetary Sciences, May 2000, Volume 28, Pages 169-209.

[47] K.R. Carver, C. Elachi, F.T. Ulaby, "Microwave remote sensing from space," Proceedings of IEEE, Volume 73, Issue 6, 1985, pp. 970-996.

[48] M.I. Skolnik, *Introduction to Radar Systems*, 3rd Edition, McGraw Hill, New York, NY, 2001.

[49] J. Marcum, "A statistical theory of target detection by pulsed radar", Information Theory, IEEE Transactions on, April 1960, Volume 6, Issue 2, pp. 59- 267.

[50] D.K. Barton, *Radar System Analysis and Modeling*, Boston, Artech House, 2005.

[51] B.R. Mahafza, A. Elsherbeni, *MATLAB Simulations for Radar Systems Design*, Chapman & Hall/CRC, December 17, 2003.

[52] D.A. Shnidman, "The calculation of the probability of detection and the generalized Marcum Q-function", Information Theory, IEEE Transactions on Volume 35, Issue 2, March 1989, pp. 389-400

[53] S. Parl, "A New Method of Calculating the Generalized Q Function", IEEE Transactions on Information Theory, 26, pp. 121-124, January 1980.

[54] D.O. North, "An Analysis of the factors which determine signal/noise discrimination in pulsed-carrier systems", Proceedings of the IEEE, July 1963, Volume 51, Issue 7, pp. 1016- 1027.

[55] P.E. Dennison, D.A. Roberts, E. Reith, J.C. Regelbrugge, and S.L. Ustin, "Integrating Polarimetric Synthetic Aperture Radar and Imaging Spectrometry for Wildland Fuel Mapping in Southern California", Proceedings of the Joint Fire Science Conference and Workshop, Boise, Idaho, June 15-17, 1999, Volume 1, pp. 37-42.

[56] L.M. See, S Fritz, "A Method to Compare and Improve Land Cover Datasets: Application to the GLC-2000 and MODIS Land Cover Products", IEEE Transactions on Geoscience and Remote Sensing, Volume 44, Issue 7, 2006, pp. 1740-1746.

[57] G. Ogden, S. Matzner, L. Zurk, D. Blejer, "Multipath Return for Radar Targets over a Rough Surface", IEEE Antennas and Propagation International Symposium, 2007, pp. 4825-4828.

[58] I.S. Grant, W.R. Phillips, *Electromagnetism*, The Manchester Physics Series, 2nd Edition, John Wiley and Son, 1990.

[59] M.A.Leontovich, V.A. Fock, "Solution of the problem of propagation of electromagnetic waves along the earth's surface by the method of parabolic equation", J. Phys. of the USSR, 1946, Volume 10, pp. 13-24.

[60] F.D. Tappert, "The parabolic approximation method", Wave Propagation and Underwater Acoustics, Lecture Notes in Physics, J.B. Keller and J.S. Papadakis (Eds.), vol. 70. Springer, New York. 1977, pp. 224-287.

[61] G.D. Dockery, "Modeling electromagnetic wave propagation in the troposphere using the parabolic equation", IEEE Transactions. 1988, pp. 1464-1470.

[62] M.F. Levy, "Parabolic equation modeling of propagation over irregular terrain", IEEE Electronics Letters, Volume 26, No. 14, 1990, pp. 1153-1155.

[63] M.F. Levy, "Parabolic equation modelling of propagation over irregular terrain," Seventh International Conference on Antennas and Propagation (ICAP 91), U.K., April 15-18, 1991.

[64] H.V. Hitney, "Hybrid ray optics and parabolic equation methods for radar propagation modelling", IEE International Conference RADAR 92, 12-13 Oct 1992, pp. 58-61.

[65] G.P. Kulemin, *Millimeter wave radar targets and clutter*, Artech House, Dedham, MA, 2003.

[66] M.I. Skolnik, *Radar Handbook*, 2nd ed., McGraw-Hill, New York, 1990.

[67] M. Dawood, R.M. Narayanan, "Multipath and Ground Clutter Analysis for a UWB Noise Radar", IEEE Transactions on Aerospace and Electronic Systems, Volume 38, Issue 3, July 2002, pp. 838-853.

[68] ITU Recommendation ITU-R P.682-2, "Propagation data required for the design of Earth-space aeronautical mobile telecommunication systems", (Question ITU-R 207/3), International Telecommunications Union, Geneva, Switzerland, 2007.

[69] G.P. Kulemin, V.B. Razskazovskiy, "Scattering Millimeter Radiowaves by the Earth's surface at small angles", - Nauk. Dumka, Kiev, Ukraine, 1987, pp. 232. (translated from Russian)

[70] The NASA public domain release of Shuttle Radar Topography Mission digital topography data, SRTM3 version 2, data tile at 49 degrees north latitude and 36 degrees east longitude – available from ftp://e0srp01u.ecs.nasa.gov/srtm/version2/SRTM3/Eurasia/N49E036.hgt.zip, or alternately the data can be obtained from http://ftp.ecc.u-tokyo.ac.jp/GIS/e0srp01u.ecs.nasa.gov/srtm/version2/SRTM3/Eurasia/, last accessed on 29th September 2008.

[71] The NASA public domain release of Landsat ETM+ Geocover 2000 Product: tile N-35-45_2000 data, available for download from https://zulu.ssc.nasa.gov/mrsid/, last accessed on 29th September 2008.

[72] S. Feng, J. Chen, "Low-Angle Reflectivity Modeling of Land Clutter", IEEE Geoscience and Remote Sensing Letters, Volume 3, Issue 2, 2006, pp. 254-258.

[73] J.B. Billingsley, *Low Angle Radar Land Clutter: Measurements and Empirical Models*, William Andrew Publishing, New York, 2002.

[74] C.A. Darrah, D.W. Luke, "Site-Specific Clutter Modelling Using DMA Digital Terrain Elevation Data (DTED), Digital Feature Analysis Data (DFAD), and Lincoln Laboratory Five Frequency Clutter Amplitude Data", IEEE National Radar Conference, Ann Arbor, Michigan, May 1996, pp. 178-183.

[75] J. Jylha, R. Kerminen, J. Vihonen, T. Ala-Kleemola, A. "Visa, New Aspects to Knowledge-Aided Clutter Analysis", IEEE Conference on Radar, Verona, NY, April 2006, pp. 318-324.

[76] A. Kurekin, D. Marshall, D. Radford, K. Lever, G. Kulemin, "Assessment of Soil Parameter Estimation Errors for Fusion of Multichannel Radar Measurements", ISIF and IEEE Information Fusion 2006 Conference, Florence, Italy, July, 2006.

[77] V.V. Lukin, N.N. Ponomarenko, A.A. Kurekin, A.A. Zelensky, J.T. Astola, P. Koivisto, K.P. Saarinen, "Nonlinear Algorithms for Isogram Extraction from Topographic Maps", Proc. Of IS&T/SPIE Symposium on Electronic Imaging: Science and Technology, San Jose, CA, USA, January 1998, SPIE Volume 3304, pp. 47-58.

[78] A. Farina, F.C. Morabito, S. Serpico, G. Simone, "Fusion of Radar Images: State of Art and Perspective", CIE International Conference on Radar, Beijing, China, 2001, pp. 9-15.

[79] A. Kurekin, D. Marshall, D. Radford, K. Lever, A. Dolia, "Mitigation of Sensor and Communication System Impairments for Multichannel Image Fusion and Classification", ISIF and IEEE Information Fusion 2005 Conference, Philadelphia, USA, July, 2005.

[80] F.T. Ulaby, R.K. Moore, A.K. Fung, *Microwave Remote Sensing: Active and Passive, From Theory to Applications*, Volumes 2 and 3, Artech House, Dedham, MA, 1986.

[81] T. Westra, K.C. Mertens and R.R. De Wulf, "Wavelet-based fusion of SPOT/VEGETATION and ENVISAT/ASAR Wide Swath data for wetland mapping", International SPOT/VEGETATION Users Conference, Antwerp, Belgium, March 2004, pp. 24-26.

[82] Z. Korona and M. M. Kokar, "Multiresolution Multisensor Target Identification", J. D. Irwin (Ed.), *The Industrial Electronics Handbook*, CRC Press and IEEE Press, 1997, pp. 1627-1632.

[83] Z. Zhang and R. S. Blum, "A region-based image fusion scheme for concealed weapon detection", Proceedings of the 31st Annual Conference on Information Sciences and Systems, March 1997, pp. 168-173.

[84] H. Li, B. S. Manjunath, S. K. Mitra, "Multisensor Image Fusion using the Wavelet Transform", Graphical Models and Image Processing, Volume 57, pp. 235-245, 1995.

[85] W. Wang, P. Shui, G. Song, "Multifocus image fusion in wavelet domain", 2003 International Conference on Machine Learning and Cybernetics, Volume 5, 2-5 November 2003, pp. 2887-2890.

[86] S. Sanjeevi, K. Vani, K. Lakshmi, "Comparison Of Conventional And Wavelet Transform Techniques For Fusion Of IRS-1C LISS-III And Pan Images", Proceedings of ACRS 2001 - 22nd Asian Conference on Remote Sensing, Singapore. Volume 1, 5-9 November 2001, pp. 140-145.

[87] F. Sadjadi, "Comparative Image Fusion Analysais", IEEE Computer Society Conference on Computer Vision and Pattern Recognition 2005, Volume 3, 20-26 June 2005.

[88] M. Dai, C. Peng, A. K. Chan, and D. Loguinov, "Bayesian wavelet Shrinkage With Edge Detection for SAR Image Despeckling", IEEE Transactions On Geoscience And Remote Sensing, Volume 42, Issue 8, August 2004, pp. 1642-1648.

[89] T. Mei, Q. Huang, H. Zhou, H. Zhao, H. Feng, "Improved multiscale image enhancement via Laplacian pyramid", Proceedings of Second International Conference on Image and Graphics, SPIE, Volume 4875, July 2002, pp. 402-407.

[90] D. Capstick, R. Harris, "The effects of speckle reduction on classification of ERS SAR data", International Journal of Remote Sensing, Volume 22, Issue 18, 15 December 2001, pp. 3627-3641.

[91] Z. Chen, Y. Zheng, B.R. Abidi, D.L. Page, and M.A. Abidi, "A Combinational Approach to the Fusion, De-noising and Enhancement of Dual-Energy X-Ray Luggage Image", Proceedings of IEEE Conference on Computer Vision and Pattern Recognition, Workshop CDROM, San Diego, CA, USA, June 2005.

[92] N. G. Kingsbury, "Complex wavelets for shift invariant analysis and filtering of signals", Journal of Applied and Computational Harmonic Analysis, Volume 11, Issue 3 May 2001, pp. 234-253.

[93] John C. Curlander and Robert N. McDonough, *Synthetic Aperture Radar: Systems and Signal Processing*, New York: John Wiley & Sons, 1991.

[94] P. Hill, N. Canagarajah, D. Bull, "Image Fusion Using Complex Wavelets", Proceedings of the 13th British Machine Vision Conference 2002, pp.487-496.

[95] H. Xie, L. Pierce, and F.T. Ulaby, "Statistical properties of logarithmically transformed speckle", IEEE Transactions on Geoscience and Remote Sensing, Volume 40, Issue 3, 2002, pp. 721-727.

[96] J.S. Lee, "Digital Image Enhancement and Noise Filtering by Use of Local Statistics", IEEE Transactions on Pattern Analysis and Machine Intelligence, Vol. PAMI-2, 1980, pp. 165-168.

[97] D.T. Kuan, A.A. Sawchuk, T.C. Strand, P. Chavel, "Adaptive Noise Smoothing Filter for Images with Signal-Dependent Noise", IEEE Transactions on Pattern Analysis and Machine Intelligence, Volume PAMI-7, 1985, pp. 165-177.

[98] V.S. Frost, J.A. Stiles, K.S. Shanmugan, J.C. Holtzman, "A Model for Radar Images and Its Application to Adaptive Digital Filtering of Multiplicative Noise", IEEE Transactions on Pattern Analysis and Machine Intelligence, Volume PAMI-4, 1982, pp. 157-166.

[99] R. Oktem, L. Yaroslavsky, K. Egiazarian, "Signal and image denoising in transform domain and wavelet shrinkage: A comparative study", Eusipco'98, Signal Processing IX, Theories and Applications, Island of Rhodes, Greece, Volume 4, 8-11 September 1998, pp. 2269-2272.

[100] L. P. Yaroslavsky, "Local Adaptive Image Restoration and Enhancement with the Use of DFT and DCT in a Running Window", Wavelet Applications in Signal and Image Processing IV, SPIE, Volume_2825, 1996, pp. 2-11.

[101] D.L. Donoho, "De-Noising by Soft-Thresholding", IEEE Transactions on Information Theory, Volume 41, Issue 3, 1995, pp. 613-627.

[102] G.H. Qu, D.L. Zhang, and P.F. Yan, "Information measure for performance of image fusion", Electronic Letters, 2002, Volume 38, Issue 7, pp. 313-315.

[103] G. Piella, "New Quality Measures for Image Fusion", Proceedings of the Seventh International Conference on Information Fusion, Stockholm, Sweden, 28 June - 1 July 2004, pp. 542-546.

[104] D.M. Bychkov, O.S. Gavrilenko, E.M. Ganapolsky, et al., "Combined Calibration of Air-and Spaceborne SLAR/SAR Systems for Remote Sensing Applications", Progress of Modern Radio Electronics, 6, (2005), pp. 31-41, in Russian (English translation: Telecommunication and Radioengineering, Begell House, NY).

[105] V.N. Tsymbal, A.S. Gavrilenko, A.A. Negoda at al., "Exploitation background of the airborne four - frequency radar complex "MARS" for sea surface, sea ice and land monitoring and the project of designing an airborne multiprofile complex for remote sensing of environment in Ukraine", Proceedings of the Third International Airborne Remote Sensing Conference and Exhibition, Copenhagen, Denmark, July 1997, Volume II, pp. 188-195.

[106] J.A. Richards, X. Jia, *Remote Sensing Digital Image Analysis: An Introduction*, 4th edition, Springer-Verlag, Berlin, 2006.

[107] P. Beckmann, A. Spizzichino, *The Scattering of Electromagnetic Waves from Rough Surfaces*, Artech House, Norwood, MA, 1987.

[108] A. Ishimaru, *Wave propagation and scattering in Random Media*, Academic Press, New York, 1978.

[109] A.K. Fung, Z. Li, K.S. Chen, "Backscattering from a randomly rough dielectric surface", IEEE Transactions on Geoscience and Remote Sensing, Volume 30, Issue 2, 1992, pp. 356-369.

[110] G.P. Kulemin, E.V. Tarnavsky, "Land clutter map development for millimeter-wave radar", Proceedings of the IEEE Radar Conference Radar03, May 2003, pp. 399-404.

[111] S.E. Fahlman, C. Lebiere, "The cascade-correlation learning architecture," Advances in Neural Information Processing 2, D. S. Touretzky, Ed. Morgan Kaufmann, 1990, pp. 524-532.

[112] C. Simon-Klar, L. Friebe, H. Kloos, H. Lieske, W. Hinrichs, P. Pirsch, "A multi DSP board for real time SAR processing using the HiPAR-DSP 16", IEEE International Geoscience and Remote Sensing Symposium IGARSS, 2002, Volume 5, pp. 2750-2752.

[113] R. Andraka, A. Berkun, "FPGAs Make a Radar Signal Processor on a Chip a Reality", IEEE Conference Record of the Thirty-Third Asilomar Conference on Signals, Systems, and Computers, Pacific Grove, CA, 1999, pp. 559-563.

[114] D Göddeke, R. Strzodka, and S. Turek, "Accelerating double precision FEM simulations with GPUs", In Proceedings of ASIM 2005 - 18th Symposium on Simulation Technique, September 2005, pp. 139-144.

[115] I. Daubechies, *Ten Lectures on Wavelets*. Society for Industrial & Applied Mathematics (SIAM), Philadelphia, 1992.

[116] N.G. Kingsbury, "Image processing with complex wavelets", Philosophical Transactions: Mathematical, Physical and Engineering Sciences, Volume 357, Issue 1760, September 1999, pp. 2543-2560.

[117] P.J. Burt and R.J. Kolczynski, "Enhanced Image Capture Through Fusion", Proceedings of the 4th International Conference on Computer Vision, 1993, pp. 173-182.

[118] H. Li, B.S. Manjunath, S.K. Mitra, "Multisensor Image Fusion using the Wavelet Transform", Graphical Models and Image Processing, Volume 57, 1995, pp. 235-245.

[119] Z. Wang, A.C. Bovik, "A universal image quality index", IEEE Signal Processing Letters, Volume 9, Issue 3, March 2002, pp. 81-84.

APPENDIX 1

Quantitative Analysis of Impulse Noise Mitigation and Fusion Results

This appendix investigates the impact of data transmission errors with respect to fusion of Synthetic Aperture Radar (SAR) remote sensing data. The motivation behind this approach is based on the assumption that mitigation of impairments prior to fusion should improve the quality of data for the fusion process, therefore, improving the results of fusion. Simulations are conducted comprising of various intensities of data transmission errors to ascertain the robustness of the α-trimmed estimate as discussed in Section 5.2.2 in Chapter 5 and published in [41]. A method for automatic selection of the α tuning parameter which determines the robustness of the α-trimmed estimate is also proposed.

A1.1 Simulation Models for Robust Impulse Noise Mitigation and Fusion

The results presented in this chapter follow directly from Section 5.2.2, therefore, it is recommended that Section 5.2.2 be read prior to this appendix. The α-trimmed estimate and noise model used for experimental purposes are described in detail in Section 5.2.2 and [41].

The simulations are conducted as follows:

- Assessment of the method for automatic selection of α parameter (Section A1.2.1)
- Assessment of multiresolution fusion (Section A1.5)

A1.1.1 Data Transmission Error Models

For transmission of the complex SAR hologram data the assumption is made that a digital RF communication system is employed, where the data are corrupted by impulse noise caused by bit errors and coding/decoding errors. To demonstrate the robustness of the α-trimmed estimate for mitigation of impulse noise when no *a priori* knowledge of the communication channel is known, then the worst case scenario should be considered, for which the i.i.d. uniform impulse noise model can be implemented, as discussed in Section 5.2.2 in Chapter 5. Simulations were conducted by simulating impulse noise according to the noise model and then mitigated using α-trimmed estimate. Firstly, the performance of the automatic method for selection of the α parameter is assessed to determine its suitability for this purpose in Section A1.2. The fusion schemes are discussed in Section A1.3. Finally, SAR image fusion quality is assessed by estimating how much important information is transferred to the fused image from the input images in Section A1.4.

A1.2 A Method for Automatic Selection of α Parameter for the α-trimmed Estimate

For automatic selection of the α parameter for the α-trimmed estimate a method may be employed based on estimation of α by minimising the estimated residual error for various values of α. To determine the most suitable value for the α parameter, the α value which produces the minimum mean squared value of I is selected, as shown in (A1.1).

$$\min \{ M_s(\alpha), 0 \le \alpha \le 1 \}$$

where

$$M_s(\alpha) = \sum_{r,c} I(r,c)^2 \approx M_s + M_{imp} + M_{dist} \qquad \text{(A1.1)}$$

where M_s is the component of the signal without noise, M_{imp} is the component for impulse noise, and M_{dist} is the component for distortions due to the nonlinearity of the

α-trimmed estimate. The transform with different α that produces the minimal $\sum_{r,c} I(r,c)^2$ is close to the transform which results in the minimal mean squared error (MSE).

A1.2.1 Assessment of Method for Automatic Selection of α Parameter for α-trimmed Estimate

The method given in Equation (A1.1) in Section A1.2 automatically determines the α parameter. Simulations were conducted by manually selecting values for α to determine the optimal value of α for $0.1 \leq P_{imp} \leq 0.5$. These are then compared with the results for automatic selection of α to ascertain the effectiveness of this method in selecting appropriate values for α parameter. The graph presented in Figure A1.1 demonstrate the ability of the proposed method to select near-optimal α parameter for all intensities of noise.

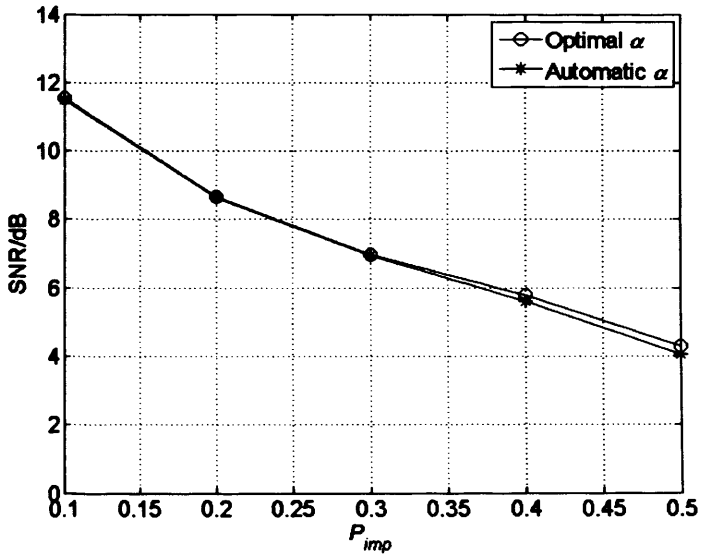

Figure A1.1 SNR for automatic α selection

The ability of Equation (A1.1) to select the α parameter close to the optimum value is further confirmed through MSE as shown in Figure A1.2 for the considered noise model.

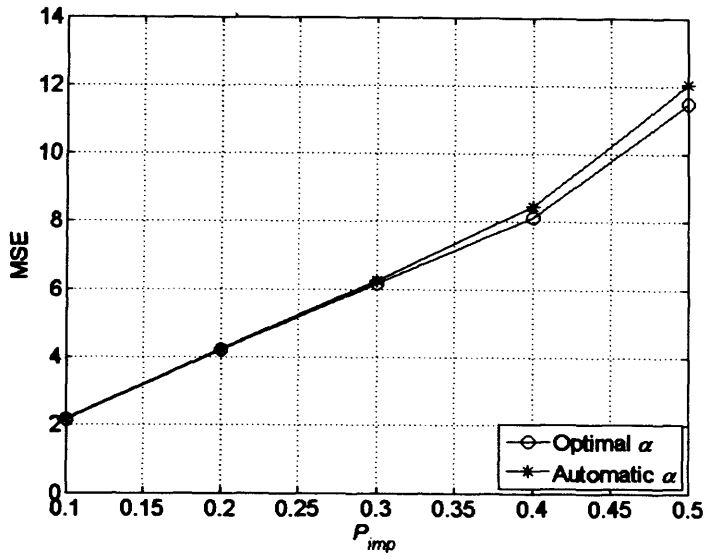

Figure A1.2 MSE for automatic α selection

A1.3 Multiresolution Fusion Schemes

The objective is to examine the effect of performing impairment mitigation techniques on the SAR data prior to fusion, with the aim of improving fusion results. To provide multiresolution analysis of the data both the Discrete Wavelet Transform (DWT) and the state-of-the-art shift-invariant Dual-Tree Complex Wavelet Transform (DT-CWT) are implemented. Combination and selection of the coefficients is achieved through application of three standard fusion rules. Coefficients with large values usually represent the salient features so a simple but a sensible fusion rule would be to choose the maximum of the absolute values. This is known as maximum selection (MS). However, more sophisticated approaches have been developed based the importance of pixels within a neighbourhood, such as weighted average (WA) and window-based verification (WBV) [94], as discussed in Section A5.2 in Appendix 5. The weighted average measure estimates the evidence of a pattern within a neighbourhood and the importance of the coefficient under consideration in that pattern. Window-based verification, on the other hand, selects the maximum of the absolute values of the coefficients and then performs a consistency check within a neighbourhood to determine how many of the neighbouring coefficients in the fused result come from the same input image as the coefficient under consideration. If the majority of neighbours come from the other image then the coefficient under

consideration is re-selected from that image. Combining these multiresolution analysis techniques and fusion rules the six fusion schemes shown in Table A1.1 are obtained.

Table A1.1 Fusion schemes.

Scheme	Description
DWT-MS	Discrete Wavelet Transform with maximum selection fusion rule
DWT-WA	Discrete Wavelet Transform with weighted average fusion rule
DWT-WBV	Discrete Wavelet Transform with window based verification fusion rule
CWT-MS	(Dual Tree) Complex Wavelet Transform with maximum selection fusion rule
CWT-WA	(Dual Tree) Complex Wavelet Transform with weighted average fusion rule
CWT-WBV	(Dual Tree) Complex Wavelet Transform with window based verification fusion rule

Analysis of the results of these fusion schemes in the presence and absence of the mitigation process will determine the validity of this approach and will be used to evaluate the effectiveness of this methodology. To assess the performance of the fusion algorithms both quantitative and qualitative measures are applied.

A1.4 Assessment of Multiresolution Fusion Results

To assess the impact of impulse noise mitigation on the fusion process, the fusion schemes detailed in Table A1.1 comprising of the Discrete Wavelet Transform and Dual-Tree Complex Wavelet Transform to provide multiresolution analysis and the maximum selection, weighted average and window-based verification fusion rules for selection of the multiresolution coefficients were implemented. The SAR images obtained from two polarisations HH and VV are shown in Figure A1.3. Simulated impulse noise was added to the images. Finally, the images were fused without performing mitigation of impulse noise, and also fused after attempting to mitigate the impulse noise. The images presented in Figures A1.3 and A1.4 are repeated (Figures 5.7 and 5.8) from Section 5.2.2 on page 75, this is for the convenience of the reader.

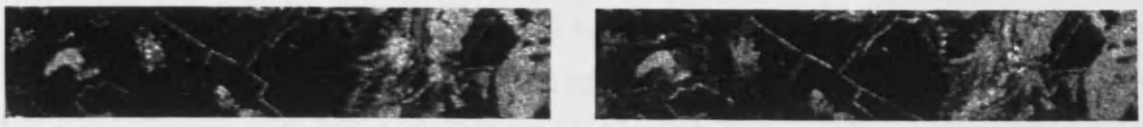

(a) (b)

Figure A1.3 SAR images: (a) HH polarisation; (b) VV polarization.

Figure A1.4 shows the results for fusion of SAR images using the DWT-MS and CWT-MS fusion schemes with simulated impulse noise P_{imp} ={0, 0.1, 0.3}, with and without mitigation of impairments.

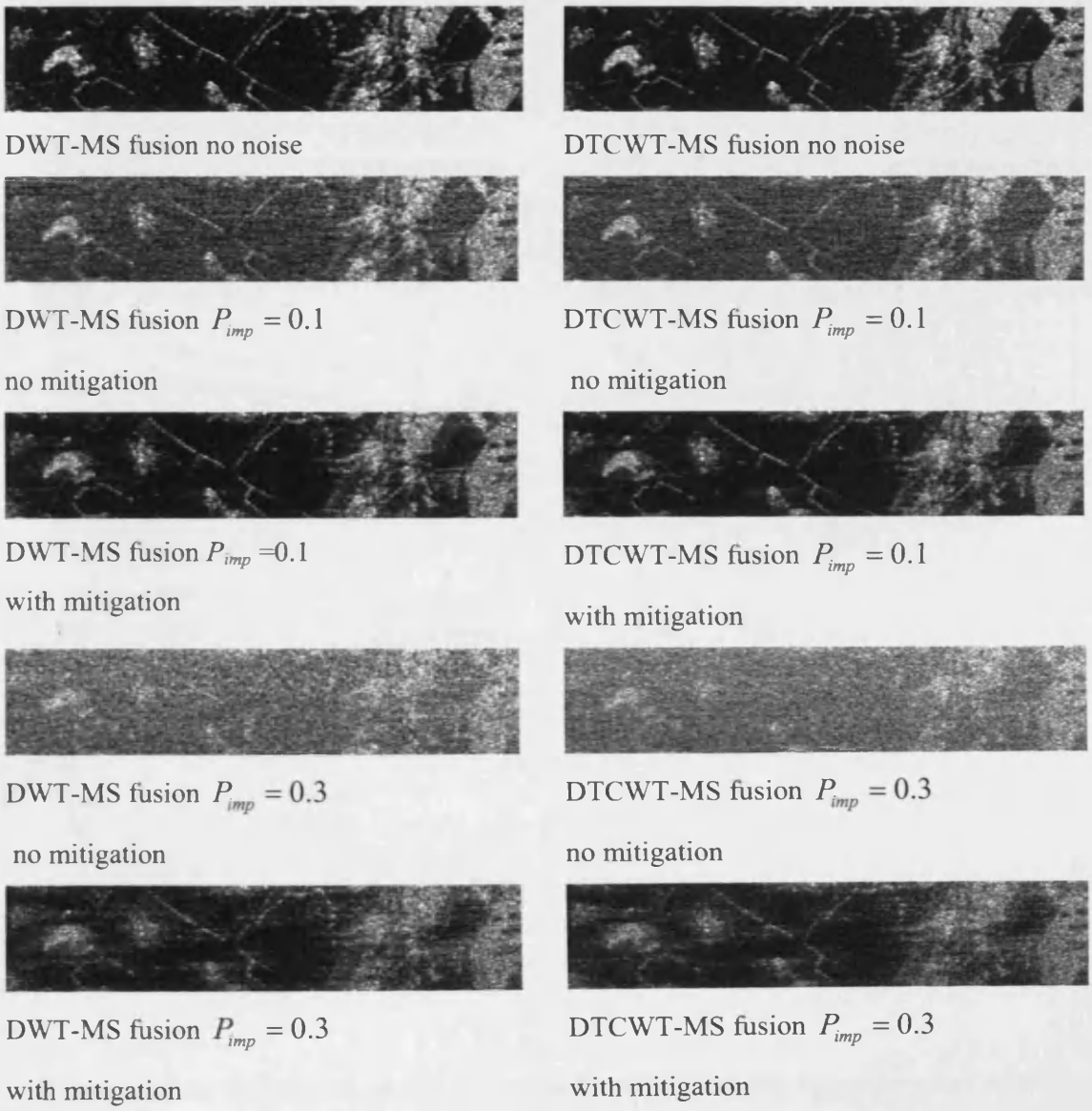

DWT-MS fusion no noise

DTCWT-MS fusion no noise

DWT-MS fusion $P_{imp} = 0.1$ no mitigation

DTCWT-MS fusion $P_{imp} = 0.1$ no mitigation

DWT-MS fusion P_{imp} =0.1 with mitigation

DTCWT-MS fusion $P_{imp} = 0.1$ with mitigation

DWT-MS fusion $P_{imp} = 0.3$ no mitigation

DTCWT-MS fusion $P_{imp} = 0.3$ no mitigation

DWT-MS fusion $P_{imp} = 0.3$ with mitigation

DTCWT-MS fusion $P_{imp} = 0.3$ with mitigation

Figure A1.4 Fusion results with and without mitigation

Fusion results are improved for all intensities of impulse noise. Generally Q_{abf} and Q_w tend to agree showing CWT-MS to offer superior performance. However, MI identifies CWT-WA as the best overall. Both the Discrete Wavelet Transform and Dual-Tree Complex Wavelet Transform exhibit similar visual results for fusion, showing an improvement over the fused results for SAR images without impulse noise mitigation as confirmed by the images in Figure A1.4. Impulse noise has been substantially diminished in the images whilst maintaining edges and bright point objects within an acceptable level for $P_{imp} \leq 0.1$. Fusion quality results with varying P_{imp} are presented in Figure A1.5 for the Dual-Tree Complex Wavelet Transform using the window-based verification fusion rule CWT-WBV, with and without mitigation of impairments.

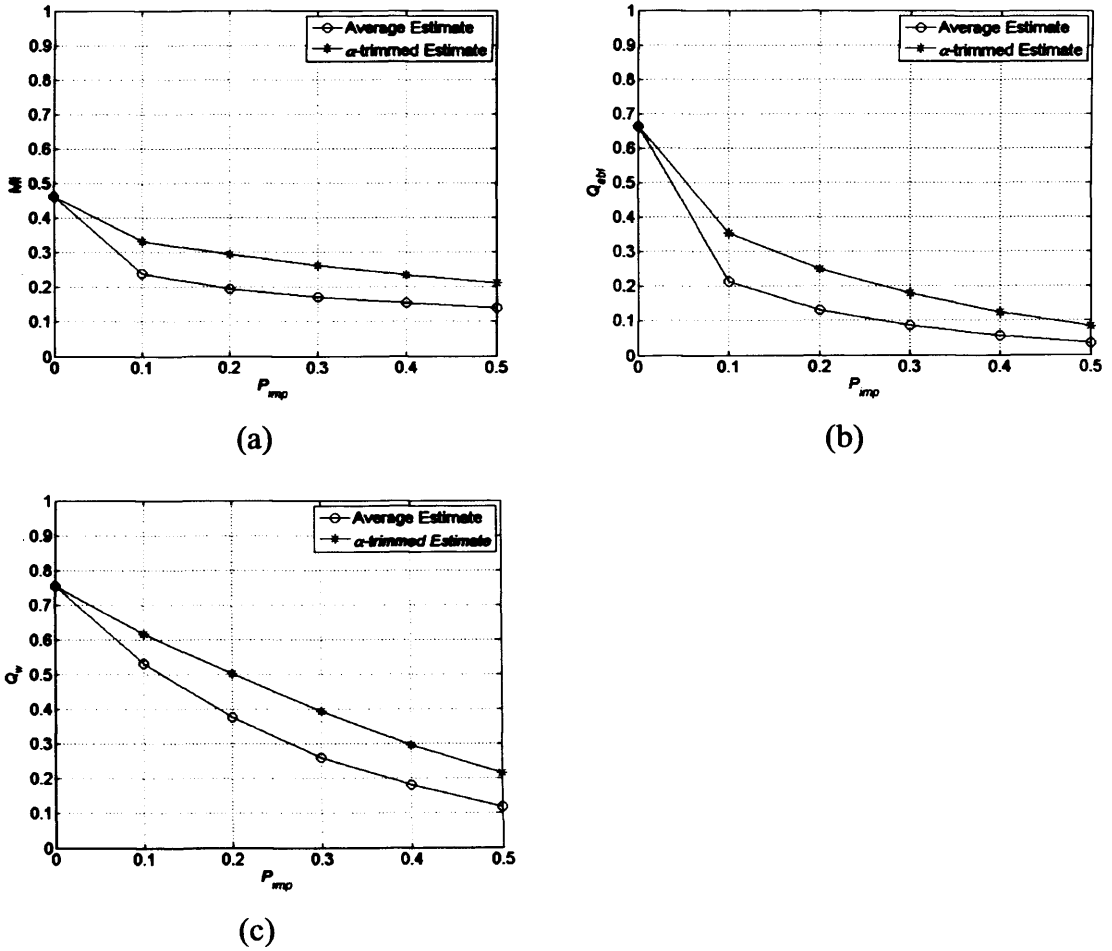

Figure A1.5. Quality measures for CWT-WBV: (a) MI impulse noise model; (b) Q_{abf} impulse noise model; (c) Q_w impulse noise model.

Clearly, fusion results are considerably improved when mitigation of impulse noise impairments for SAR images is performed prior to the fusion process. All three quality estimates demonstrate consistent improvement in image quality for varying intensities of impulse noise. Trends displayed in Figures A1.5(a)-(c) are observed for all fusion schemes considered, confirming the validity of mitigating impulse noise impairments for SAR images to improve fusion results.

A1.5 Conclusion

A new method for automatic selection of the α parameter for the α-trimmed estimate has been presented and has been shown to select near-optimal values of α for the considered intensities of impulse noise. Additionally, the α-trimmed estimate has demonstrated efficient mitigation of impulse noise impairments in SAR images.

More importantly, it has been shown that SAR fusion results can be improved by using a two stage approach; mitigating impairments at the first stage, followed by image fusion at the second stage. An additional advantage of this two stage approach is that fusion algorithms do not have to be modified in order to cope with impairments present in the source data.

APPENDIX 2

Quantitative Analysis of the Multiresolution DCT for Simultaneous Denoising and Fusion

In this appendix, a quantitative analysis is presented for the Multiresolution DCT method discussed in Section 5.2.3 and published in [42]. Results are presented for test data. The results presented in this appendix follow directly from Section 5.2.2 in Chapter 5, therefore, it is recommended to read this prior to the current appendix.

A2.1 A Discussion on Test Data and Fusion Schemes

To assess the ability of the proposed Multiresolution DCT (MR-DCT) technique for noise suppression and fusion, simulations are conducted on test images. The results of the Multiresolution DCT are compared and contrasted with the Discrete Wavelet Transform (DWT) and Dual Tree Complex Wavelet Transform (DTCWT) for the tasks of denoising and fusion. Firstly, the considered fusion schemes are applied for the selected test images. The test images are required so that ground-truth data is available to quantitatively assess the denoising and fusion results. The two test images selected are shown in Figure A2.1. The image in Figure A2.1 has been repeated (Figure 5.10(a) on page 82) from Section 5.2.3 for the convenience of the reader.

(a) (b)

Figure A2.1 Original test images; (a) Barbara; (b) Lena.

The Barbara test image, Figure A2.1(a), was specifically selected because it contains a substantial amount of texture information as well as some homogenous regions. This type of information content is representative of real SAR data image content. The Lena test image, Figure A2.1(b), was selected in contrast to the Barbara image, as it contains substantial homogenous regions and only a small amount of texture information. The motivation behind selecting two distinctly different test images is to allow the performance of each fusion scheme to be evaluated for different types of source data. Using this approach will provide the opportunity to identify the strengths and weaknesses of each fusion scheme. The fusion and denoising schemes considered are shown in Table A2.1.

Table A2.1 Fusion/denoising schemes

Scheme	**Description**
DWT-MS	DWT with *maximum selection*
DWT-WA	DWT with *weighted average*
DWT-WBV	DWT with *window based verification*
CWT-MS	DT-CWT with *maximum selection*
CWT-WA	DT-CWT with *weighted average*
CWT-WBV	DT-CWT with *window based verification*
MRDCT-MS	MR-DCT with *maximum selection*
MRDCT-WA	MR-DCT with *weighted average*
MRDCT-WBV	MR-DCT with *window based verification*

SNR and MSE are used to assess the quality of image fusion and denoising for the test images.

The simulations are conducted as follows:

- Fusion only of test images (Barbara and Lena). (Section A2.2)
- Fusion only of noisy test images (Barbara and Lena). (Section A2.3)
- Fusion and denoising of test images (Lena). (Section A2.4)
- Fusion and denoising of real SAR data. (Section A2.5)

A2.2 Fusion of Blurred Test Images

Fusion is applied for test images to assess the fusion characteristics of each fusion scheme. The Barbara test images are shown in Figure A2.2. (note that Figures A2.2(a-c) have been repeated from Figures 5.10(a-c) in Section 5.2.3 on page 82)

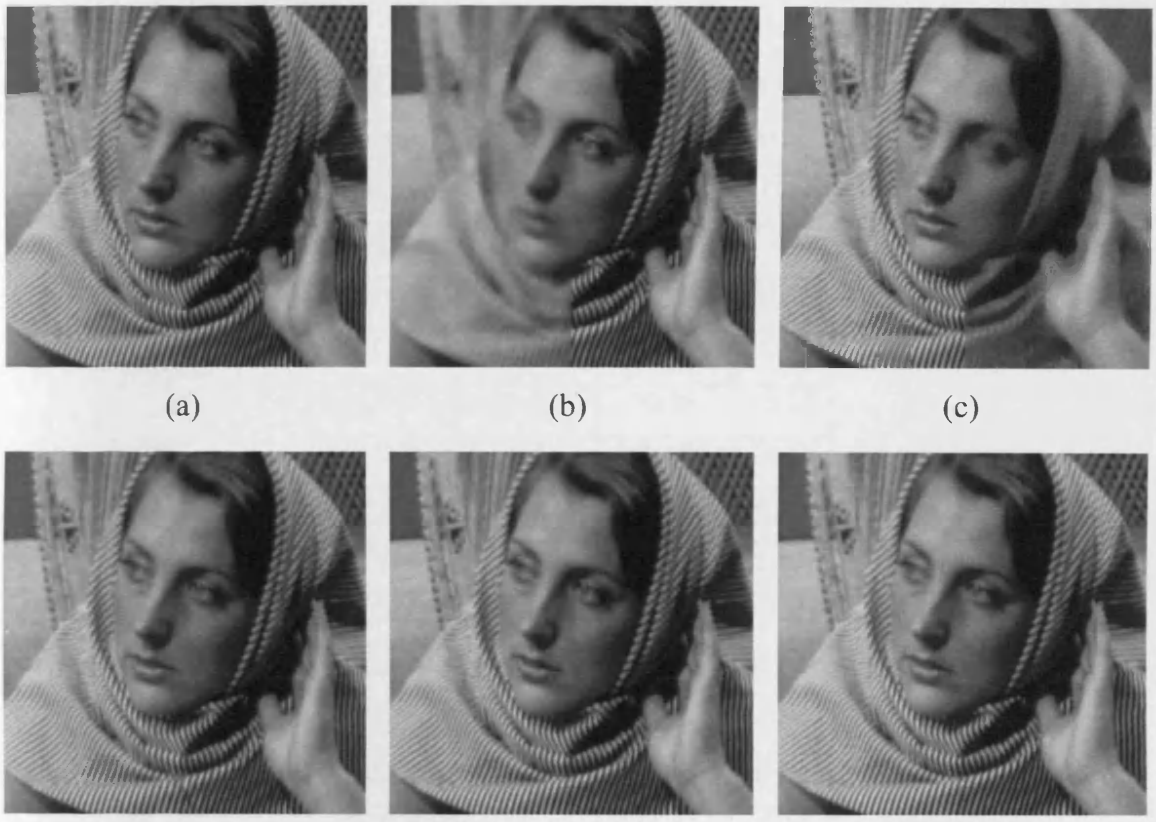

(a) (b) (c)

(d) (e) (f)

Figure A2.2 Fusion images:
(a) original test image Barbara; (b) test image 1 blurred on left;
(c) test image 2 blurred on right; (d) DWT-WA;
(e) CWT-MS; (f) MRDCT-WBV (3×3).

The original Barbara test image shown in Figure A2.2(a) is used as ground-truth data to assess the fusion results. Two images of Barbara are used for fusion source images; one image is median filtered with 7×7 window on the left side of the image as shown in Figure A2.2(b), and the other image is median filtered with 7×7 window on the right side of the image as shown in Figure A2.2(c). Creating two test images in this manner we obtain two completely different images where each image has important detail information in only 50% of the image. This will illustrate how effective each

fusion scheme is in selecting the important information. The best fusion results obtained for the Discrete Wavelet Transform, Dual Tree Complex Wavelet Transform and Multiresolution DCT are shown in Figures A2.2(d)-(f) respectively. Visually, it is difficult to discriminate between the fused images and identify any differences; however, quantitative quality measures shown in Table A2.2 clearly indicate that there are differences.

Table A2.2 Fusion results for Barbara test image

Scheme	SNR dB	MSE
DWT-MS	32.37	10.8
CWT-MS	37.51	3.3
MRDCT-MS (3x3)	34.51	6.59
MRDCT-MS (5x5)	34.07	7.3
MRDCT-MS (7x7)	30.88	15.22
MRDCT-MS (9x9)	30.6	16.22
DWT-WA	34.69	6.33
CWT-WA	35.7	5.01
MRDCT-WA (3x3)	36.9	3.8
MRDCT-WA (5x5)	36.22	4.38
MRDCT-WA (7x7)	34.88	6.05
MRDCT-WA (9x9)	34.55	6.53
DWT-WBV	34.31	6.91
CWT-WBV	36.96	3.75
MRDCT-WBV (3x3)	38.02	2.93
MRDCT-WBV (5x5)	37.07	3.65
MRDCT-WBV (7x7)	36.05	4.63
MRDCT-WBV (9x9)	35.58	5.15

Lower values for SNR and higher values of MSE indicate improper selection of the detail components by the fusion scheme. It can be seen that MRDCT-WBV with a 3×3 DCT window offers the best results for fusion of the Barbara test image. The Dual Tree Complex Wavelet Transform offers comparable results to the Multiresolution DCT while the Discrete Wavelet Transform performs substantially worse than both methods. This procedure is then applied for the Lena test image as shown in Figure A2.3.

(a) (b) (c)

(d) (e) (f)

Figure A2.3 Fusion images:
(a) original test image Lena; (b) test image 1 blurred on left;
(c) test image 2 blurred on right; (d) DWT-WA;
(e) CWT-WBV; (f) MRDCT-WA (3×3).

The original Lena test image shown in Figure A2.3(a) is used for ground-truth data. Two test images are used for fusion source images; one image is median filtered with 7×7 window on the left side of the image as shown in Figure A2.3(b), and the other image is median filtered with 7×7 window on the right side of the image as shown in Figure A2.3(c). The best fusion results obtained for the Discrete Wavelet Transform, Dual Tree Complex Wavelet Transform and Multiresolution DCT are shown in Figures A4.6(d)-(f) respectively. Close examination of the fused images reveal very subtle differences which are hardly noticeable to the naked eye. However, the quality estimates provided by SNR and MSE as shown in Table A2.3, indicate that differences are present.

Table A2.3 Fusion results for Lena test image

Scheme	SNR dB	MSE
DWT-MS	30.32	16.415
CWT-MS	34.88	5.75
MRDCT-MS (3x3)	32.34	10.31
MRDCT-MS (5x5)	31.59	12.26
MRDCT-MS (7x7)	26.75	37.35
MRDCT-MS (9x9)	29.19	21.27
DWT-WA	33.98	7.07
CWT-WA	34.19	6.73
MRDCT-WA (3x3)	36.11	4.32
MRDCT-WA (5x5)	35.16	5.39
MRDCT-WA (7x7)	32.87	9.12
MRDCT-WA (9x9)	33.94	7.13
DWT-WBV	33.94	7.12
CWT-WBV	36.65	3.82
MRDCT-WBV (3x3)	36.1	4.34
MRDCT-WBV (5x5)	36.11	4.33
MRDCT-WBV (7x7)	34.91	5.7
MRDCT-WBV (9x9)	33.91	7.19

For fusion of the Lena test image, different fusion schemes provide the best quality estimates in comparison with the Barbara test image. For the Lena test image fusion the CWT-WBV fusion scheme provides the best overall result, however, the MRDCT-WA with a 3×3 DCT window offers comparable results, with both schemes achieving SNR estimates 2dB greater than the best result provided by any Discrete Wavelet Transform scheme. Considering the results from both test images, it seems that different fusion schemes provide better results for fusion depending on the image content of the source data. Generally, the Multiresolution DCT and Dual Tree Complex Wavelet Transform offer similar performance for fusion, efficiently selecting the detail components whilst rejecting non-detail components. The lower quality estimates achieved by the Discrete Wavelet Transform schemes suggest that the Discrete Wavelet Transform is not as efficient in rejecting non-detail components

while fusing. For the Multiresolution DCT it has been demonstrated that the size of the DCT window affects the fusion results, with the best performance obtained for smaller window sizes.

A2.3 Fusion of Noisy Test Images

The previous section addressed fusion of test images containing different information. Now fusion of noisy source data is considered. The Barbara test images are shown in Figure A2.4.

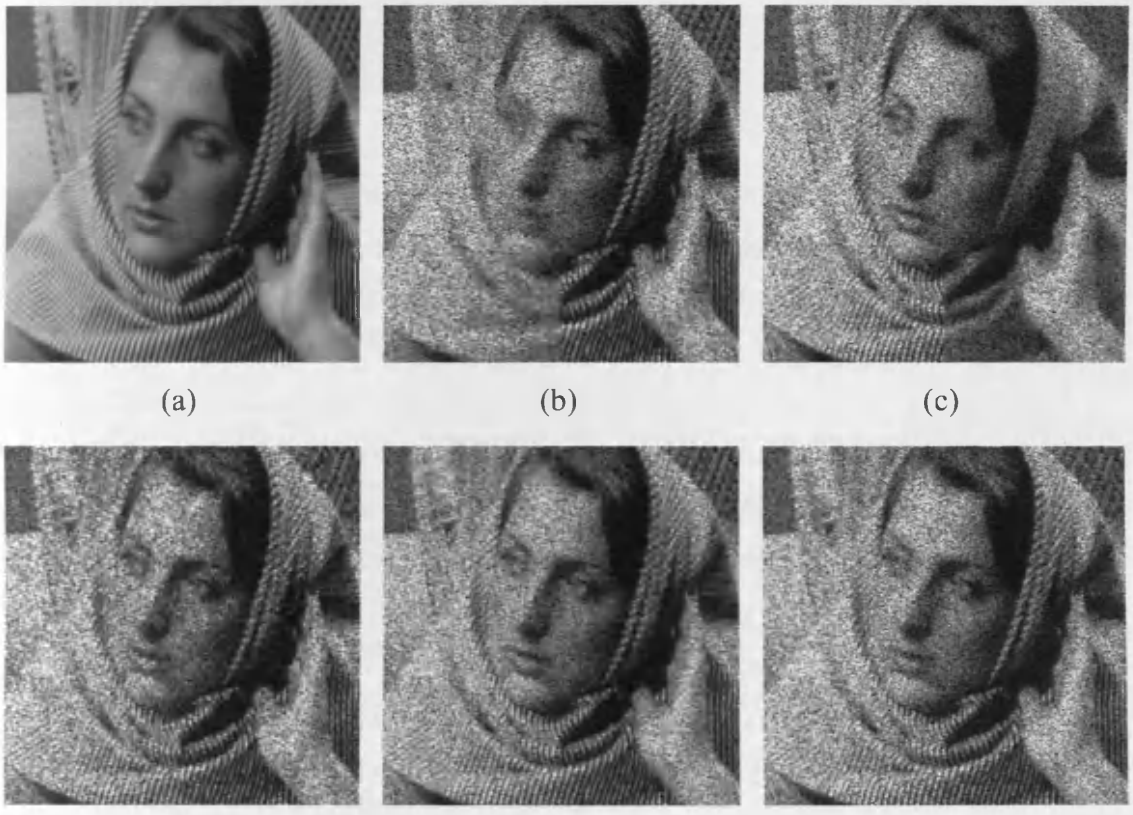

(a) (b) (c)

(d) (e) (f)

Figure A2.4 Noisy image fusion: (a) noisy test image Barbara; (b) test image 1 blurred on left and simulated noise; (c) test image 2 blurred on right and simulated noise; ; (d) DWT-WBV; (e) CWT-WA; (f) MRDCT-WA (3×3).

The original test image of Barbara as shown in Figure A2.4(a) is used as ground-truth data for image quality estimation. Simulated multiplicative Gaussian noise with coefficient of noise variation $\sigma_n^2 = 0.05$ was added to the blurred Barbara test images

shown in Figures A2.4(b)-(c) to obtain the noisy blurred Barbara test images shown in Figures A2.4(b)-(c). The noisy test images are then fused using the fusion schemes, but no attempt is made to remove the noise. This approach is adopted to assess the characteristics of each fusion scheme for image fusion in a noisy environment. The best fusion results obtained for the Discrete Wavelet Transform, Dual Tree Complex Wavelet Transform and Multiresolution DCT are shown in Figures A2.4(d)-(f) respectively. Discrete Wavelet Transform schemes tend to be most susceptible to the influence of noise, with the Multiresolution DCT offering slightly better performance particularly for some textured regions of the headscarf, but the Dual Tree Complex Wavelet Transform appears less noisy than both the Discrete Wavelet Transform and Multiresolution DCT. The quality estimates for noisy test image fusion without denoising are shown in Table A2.4.

Table A2.4 Fusion results for noisy Barbara test image

Scheme	SNR dB	MSE
DWT-MS	10.32	1729.7
CWT-MS	11.94	1193.5
MRDCT-MS (3x3)	10.66	1599.6
MRDCT-MS (5x5)	10.54	1644.4
MRDCT-MS (7x7)	10.5	1662.7
MRDCT-MS (9x9)	10.52	1654.8
DWT-WA	11.53	1311.3
CWT-WA	13.46	839.48
MRDCT-WA (3x3)	12.22	1118.5
MRDCT-WA (5x5)	11.98	1180.9
MRDCT-WA (7x7)	11.91	1201.2
MRDCT-WA (9x9)	11.81	1228
DWT-WBV	11.58	1294.5
CWT-WBV	13.06	921.1
MRDCT-WBV (3x3)	11.83	1222.3
MRDCT-WBV (5x5)	11.72	1255
MRDCT-WBV (7x7)	11.74	1248.5
MRDCT-WBV (9x9)	11.74	1247.6

These results tend to agree with the observations made above, showing that the DTCWT-WA clearly outperforms all other schemes achieving gains in SNR estimate of at least 1dB in comparison with the Discrete Wavelet Transform and Multiresolution DCT schemes. Here, the Multiresolution DCT and Discrete Wavelet Transform offer comparable performance in the presence of noise. The same procedure for noisy image fusion is followed for the Lena test image as shown in Figure A2.5.

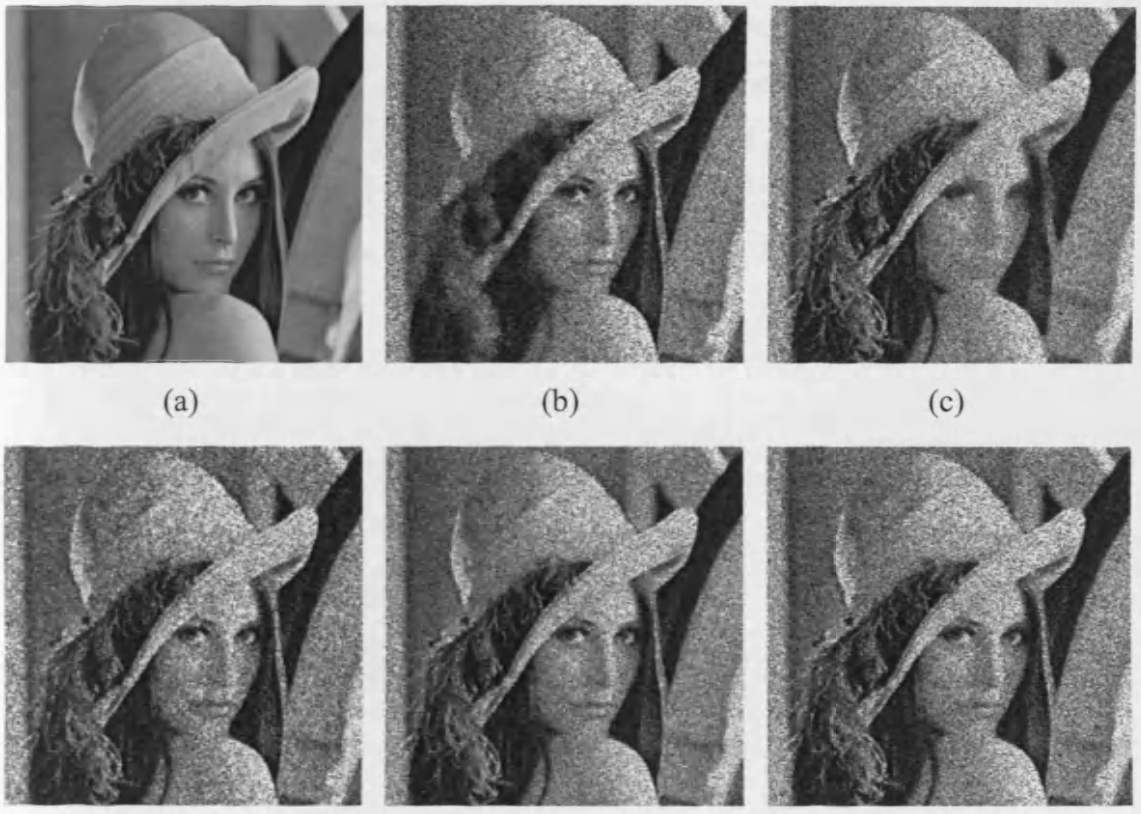

(a) (b) (c)

(d) (e) (f)

Figure A2.5 Noisy image fusion:
(a) noisy test image Lena; (b) test image 1 blurred on left and simulated noise; (c) test image 2 blurred on right and simulated noise; (d) DWT-WBV; (e) CWT-WA; (f) MRDCT-WA (3×3).

The original test image of Lena as shown in Figure A2.5(a) is used as ground-truth data for image quality estimation. Simulated multiplicative Gaussian noise with coefficient of noise variation $\sigma_n^2 = 0.05$ was added to the blurred Lena test images shown in Figures A2.5(b)-(c) to obtain the noisy blurred Lena test images shown in Figures A2.5(b)-(c). The best fusion results obtained for the Discrete Wavelet

Transform, Dual Tree Complex Wavelet Transform and Multiresolution DCT are shown in Figures A2.5(d)-(f) respectively. Visual analysis confirms similar results as the Barbara test images in Figure A2.4, again the Multiresolution DCT and Discrete Wavelet Transform appear slightly more noisy than the Dual Tree Complex Wavelet Transform suggesting that the Dual Tree Complex Wavelet Transform is more robust in a noisy environment. The quality estimates shown in Table A2.5 support this observation.

Table A2.5 Fusion results for noisy Lena test image

Scheme	SNR dB	MSE
DWT-MS	10.33	1639.6
CWT-MS	11.94	1130.8
MRDCT-MS (3x3)	10.64	1526.1
MRDCT-MS (5x5)	10.53	1563
MRDCT-MS (7x7)	10.44	1599
MRDCT-MS (9x9)	10.51	1573.2
DWT-WA	11.56	1233.5
CWT-WA	13.44	799.77
MRDCT-WA (3x3)	12.28	1046.8
MRDCT-WA (5x5)	12.01	1112.5
MRDCT-WA (7x7)	11.87	1149.1
MRDCT-WA (9x9)	11.85	1155.5
DWT-WBV	11.57	1232.3
CWT-WBV	13.03	880.04
MRDCT-WBV (3x3)	11.86	1150.8
MRDCT-WBV (5x5)	11.75	1182.1
MRDCT-WBV (7x7)	11.74	1184.9
MRDCT-WBV (9x9)	11.70	1194.3

Again, the Discrete Wavelet Transform and Multiresolution DCT achieve comparable quality estimates but are clearly outperformed by the Dual Tree Complex Wavelet Transform. The best results for the Multiresolution DCT are obtained for smaller DCT window sizes. In general, the Dual Tree Complex Wavelet Transform clearly performs best for fusion of noisy data, while the Discrete Wavelet Transform and

Multiresolution DCT offer worse but comparable results to each other. Smaller DCT window sizes provide the best results for noisy data fusion using the Multiresolution DCT. Overall the results indicate that the Dual Tree Complex Wavelet Transform is more robust for fusion of noisy data. Also, different fusion schemes are identified as producing the best quality results for different test images.

A2.4 Simultaneous Fusion and Denoising of Test Images

Now simultaneous denoising and fusion is considered for noisy test images. The original Lena test image as shown in Figure A2.6(a) is used for the ground-truth data. The noisy Lena test images in Figures A2.6(b)-(c) are the exact same noisy test images as Figures A2.5(b)-(c). The best fusion and denoising results obtained for the Discrete Wavelet Transform, Dual Tree Complex Wavelet Transform and Multiresolution DCT are shown in Figures A2.6(d)-(f), respectively.

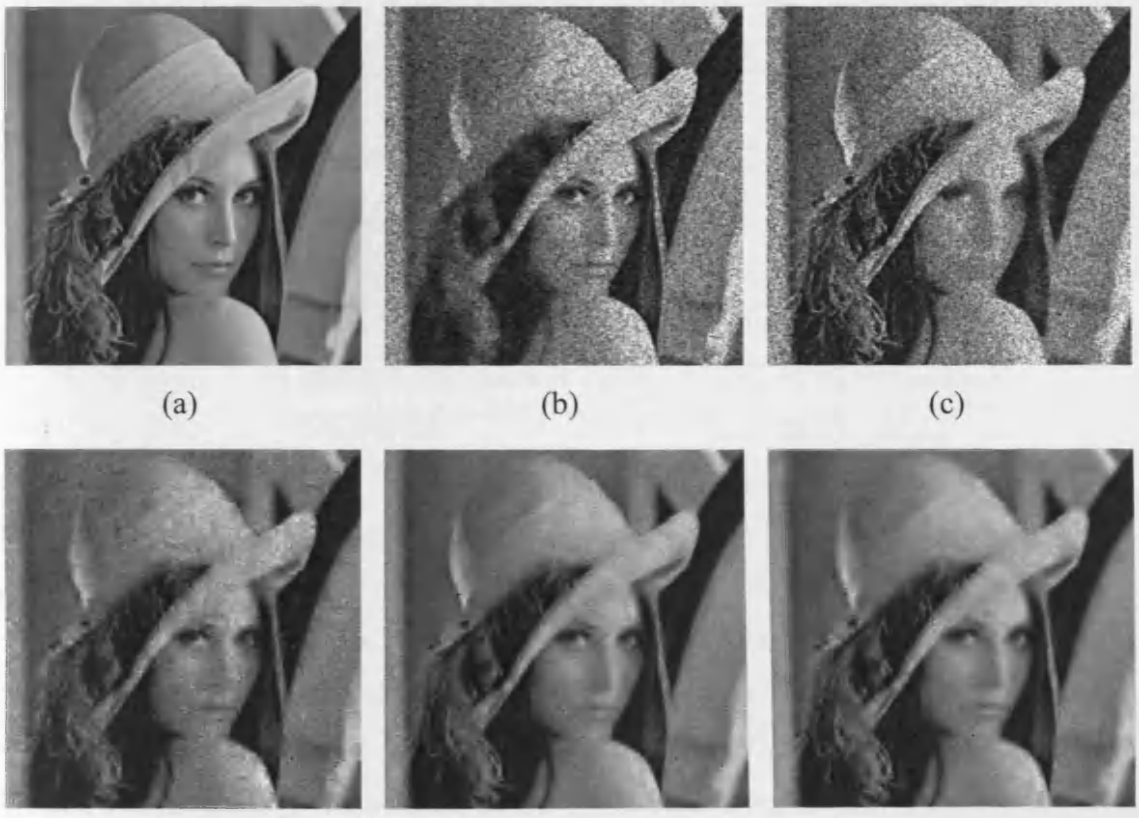

(a) (b) (c)

(d) (e) (f)

Figure A2.6 Denoising and fusion images:(a) original test image Lena; (b) test image 1 blurred on left and simulated noise; (c) test image 2 blurred on right and simulated noise; (d) DWT-MS; (e) CWT-MS; (f) MRDCT-WA (9×9).

Poorest noise suppression is exhibited by DWT-MS. MRDCT-WA suppresses noise marginally better than CWT-MS, but this is at the expense of introducing greater artefacts into the image. CWT-MS seems to have slightly better definition in the facial region with the exception of the mouth area which is better defined in the MRDCT-WA. Comparison of these results suggest that the Multiresolution DCT provides better noise suppression than the Dual Tree Complex Wavelet Transform but achieves lower quality estimates due to the artefacts introduced into homogenous regions. The quality estimates for all fusion schemes are shown in Table A2.6.

Table A2.6 Denoising and Fusion Results for Lena test image

Scheme	SNR dB	MSE
DWT-MS	17.8	293.67
CWT-MS	19.95	178.93
MRDCT-MS (3x3)	18.45	252.69
MRDCT-MS (5x5)	19.33	206.39
MRDCT-MS (7x7)	19.13	215.83
MRDCT-MS (9x9)	19.63	192.29
DWT-WA	17.45	318.16
CWT-WA	19.63	192.36
MRDCT-WA (3x3)	18.47	251.37
MRDCT-WA (5x5)	19.34	205.68
MRDCT-WA (7x7)	19.49	198.61
MRDCT-WA (9x9)	19.64	192.04
DWT-WBV	17.49	315.33
CWT-WBV	19.79	185.38
MRDCT-WBV (3x3)	18.54	247.61
MRDCTWBV (5x5)	19.28	208.46
MRDCT-WBV (7x7)	19.58	194.69
MRDCT-WBV (9x9)	19.60	193.76

It can be seen that CWT-MS achieves the highest quality estimates. Additionally, the best results for the Multiresolution DCT are achieved with larger window sizes, again suggesting that large window sizes are required for efficient noise suppression in the DCT domain.

The test images are perfectly registered; therefore, the shift-invariance properties of the Multiresolution DCT and Dual Tree Complex Wavelet Transform have no real advantage here. For the Dual Tree Complex Wavelet Transform fusion and denoising the phase information is not considered by the fusion rules. This would imply that the results achieved for the Dual Tree Complex Wavelet Transform are due to its increased directional sensitivity, having six directional subbands, whereas the Multiresolution DCT and Discrete Wavelet Transform only have three directional subbands. The results obtained by the Multiresolution DCT must therefore be attributed to its good signal localisation in both the spatial and frequency domains, permitting suitable selection of coefficients for both fusion and denoising.

A2.5 Conclusion

Common techniques and state-of-the-art methods have been implemented for simultaneous denoising and fusion of test images, and compared to the new technique described in Section 5.2.3 and [42]. The denoising and fusion results were assessed using quantitative metrics to determine the effectiveness of each technique. A qualitative visual analysis was also performed to confirm the validity and plausibility of the quantitative measures. Simulations have shown that the Multiresolution DCT-based approach can outperform the Dual Tree Complex Wavelet Transform (DT-CWT) for simultaneous denoising and fusion, demonstrating superior results for textured regions of the test images which were specifically selected to most resemble the textured characteristics of SAR images.

The difficulty of estimating image quality has been shown, where it is not sufficient to rely only on quality estimates to gauge image quality. Instead, attention needs to be paid to image content and ultimately image quality depends on the most important criteria for the application to which the data will be applied. The Multiresolution DCT has proven to be a suitable method for efficiently fusing and denoising.

APPENDIX 3

Software Model Description

The models for simulation of the Intelligent Radar Sensor (IRS) are implemented in MATLAB software code. All software is available in Appendix V on the DVD within the 'SOFTWARE' folder. The software tools are organised in five separate packages which implement the following methods and algorithms proposed in this thesis:

1. The Intelligent Radar Sensor model is implemented in MATLAB;
2. The algorithm for prediction of land surface multipath effects is implemented in MATLAB;
3. The algorithm for prediction of ground clutter for surface-sited low-grazing radar using remote sensing data is implemented in MATLAB;
4. SAR data processing algorithms for hologram impairment mitigation, multi-look and single-look image synthesis, impulse noise and bit-error noise impairment simulation are implemented in MATLAB code. SAR image fusion and fusion quality estimation algorithms are written in MATLAB. The DTCWT propriety library written in MATLAB has been partly used for implementation of SAR images fusion algorithm based on dual tree complex wavelet transform;
5. The algorithm for Multiresolution DCT-based technique for fusion and denoising simulation is implemented in MATLAB code. SAR image fusion, denoising and quality estimation algorithms are written in MATLAB. The DTCWT propriety library written in MATLAB has been partly used for implementation of SAR image fusion and denoising algorithm based on dual tree complex wavelet transform.

A description of these software components are shown in Table A3.1.

Table A3.1 Software Description for the Intelligent Radar Sensor Model

Propriety Software	**Uses**	**Description**
DTCWT		Dual Tree Complex Wavelet Transform software package
RBF_CLASS		RBF classification of satellite images
Deliverable Software		
IRS_MOD		Intelligent Radar Sensor package
	IRS_test.m	Implementation of Intelligent Radar Sensor model
	calc_shadow_target.m	Calculate shadow regions for target line of sight from radar position
	snr.m	Calculate signal-to-noise ratio
	cnr.m	Calculate clutter-to-noise ratio
	calc_gain_tgt.m	Calculate antenna gain for target position
	calc_gain_corr.m	Calculate antenna gain for land surface clutter position
	fusion_scenario.m	Implementation of radar fusion (scenario 3 – Chapter 6)
MULTIPATH_MOD		Multipath modelling package

	multipath_test.m	Implementation of Multipath model
	voltage_pattern.m	Antenna voltage pattern
	calc_angle_target.m	Calculate grazing angle for target
	specular_reflections_test.m	Calculate specular reflections
	find_specular_reflec.m	Find specular reflection positions on land surface
	spec_shadow.m	Calculate which specular reflections are invalid due to line of sight restrictions
	plot_spec.m	Plot specular reflection positions
CLUTTER_MOD		Clutter modelling for surface-sited low-grazing radar package
	add_shadow.m	Superimpose shadow map on clutter map
	calc_angle.m	Calculate grazing angles for surface-sited radar
	calc_flight_path.m	Calculate flight path for airbourne SAR
	calc_grazing.m	Calculate grazing angles for airbourne SAR
	calc_shadow.m	Calculate shadow regions for surface-sited radar
	clutter_test.m	Example of clutter map simulation

	filter_speckle.m	Filter speckle noise from SAR data
	find_line.m	Calculate direct path from surface-sited radar to any point on map
	geom_corr.m	Perform geometric correction for SAR data
	RBNN_test.m	Classify image into specified class types
	image2class.m	Extract classes from classified image
SAR_MTG		SAR impairment mitigation and image fusion package
	add_bit_noise_cgilbert.m	Simulate Gilbert noise
	add_imp_noise	Simulate i.i.d impulse noise
	alpha_est.m	Estimate intensity of noise for selection of α parameter
	hologram_test.m	Example of mitigation.
	image_err_estimate.m	Calculate quality parameters
	synt_hol_multilook_mod_var.m	Synthesise SAR image using multi-look synthesis.
	synt_hol_singlelook_var.m	Synthesise SAR image using single-look synthesis

	err_estimate.m	Calculate quality parameters
	fusion_test.m	Example of fusion
	lap_pyramid_compose.m	Compose image from Laplacian pyramid decomposition
	lap_pyramid_decompose.m	Decompose image into Laplacian pyramid multiresolution representation
	med_pyramid_compose.m	Compose image from Median pyramid decomposition
	med_pyramid_decompose.m	Decompose image into Median pyramid multiresolution representation
	selb.m	Fusion rules for selection of approximate image coefficients
	selc.m	Fusion rules for selection of detail image coefficients
	wavelet_compose.m	Compose image from Wavelet decomposition
	wavelet_decompose.m	Decompose image using discrete wavelet transform

MRDCT		Multiresolution DCT technique for SAR speckle mitigation and image fusion package
	DTCWT_anal.m	Dual-tree complex wavelet analysis of an image
	err_estimate.m	Calculate quality parameters
	estimate_thr.m	Estimate threshold for image denoising
	filter_dct_mlnoise.m	Filter DCT coefficients for multiplicative noise
	filter_mlnoise.m	Filter multiresolution coefficients for multiplicative noise
	fuse.m	Fuse multiresolution images
	Fuse_denoise_SIM.m	Example of denoisnig and fusion
	image_err_estimate.m	Calculate quality parameters
	MRDCT_anal.m	Multiresolution analysis of an image using Laplacian pyramid and sliding window DCT
	selb.m	Fusion rules for selection of approximate image coefficients
	selc.m	Fusion rules for selection of detail image coefficients

The diagram in Figure A3.1 describes the software structure of the Intelligent Radar Sensor model illustrating how the software components described above fit together to form a complete system.

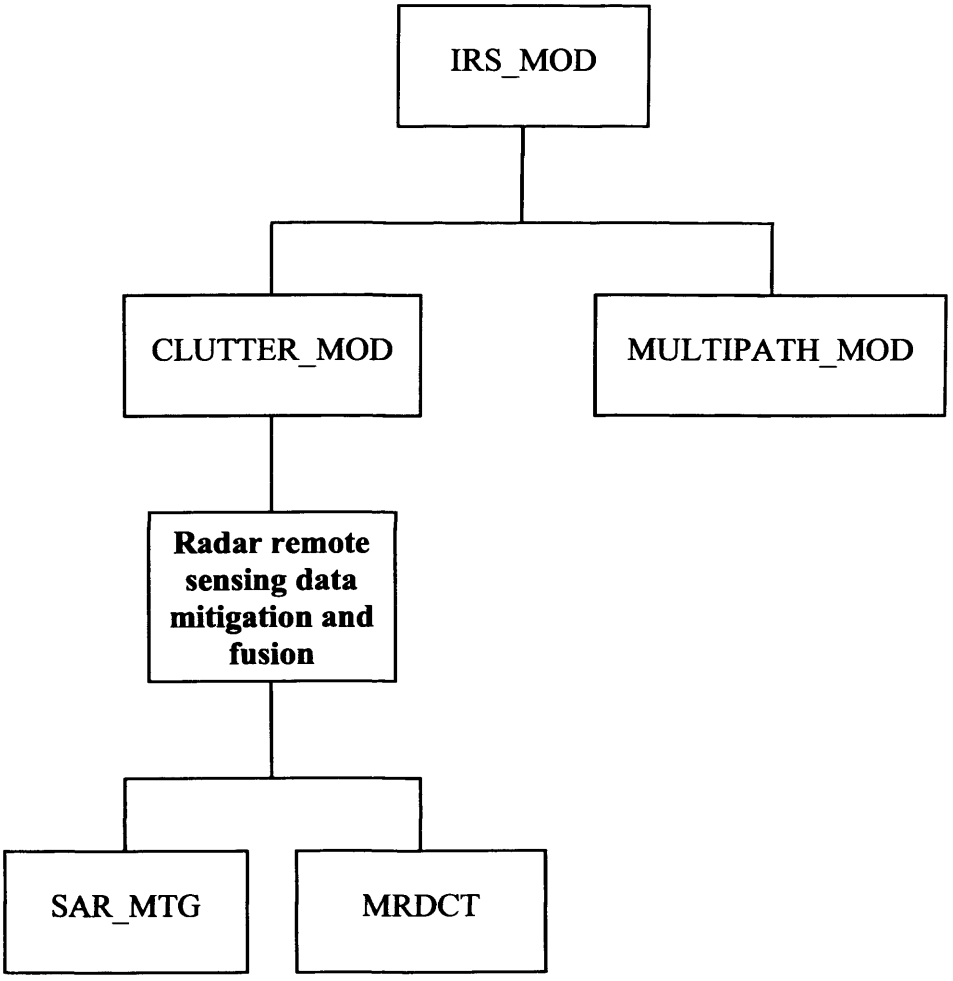

Figure A3.1 Structure of the Intelligent Radar Sensor Software Model

APPENDIX 4

DVD Containing Software Models and Animation Files

(see attached DVD)

APPENDIX 5

A Discussion on Multiresolution Methods and Quality Assessment Metrics

The following appendix addresses methods for multiresolution image fusion and considers quantitative metrics for evaluation of fusion and impairment mitigation techniques. Multiresolution analysis of 2D signals is discussed in Section A5.1, Multiresolution fusion techniques and combination rules are discussed in Section A5.2, and Section A5.3 concludes with a discussion on quantitative analysis measures for mitigation of impairments and image fusion. The material in this appendix discusses in greater detail topics which were mentioned in earlier chapters, but at that time it was not the appropriate place to these topics; therefore, they are being discussed here.

A5.1 Multiresolution Analysis of 2D signals

For successful image fusion it is important that images depicting the same scene be co-registered so that corresponding pixels in each image relate to the same location. For simplicity it is assumed that the images are co-registered prior to fusion. For image fusion a multiresolution approach may be adopted, which decomposes the signal into several components, each representing information at a given scale. This approach lends itself well to real world applications as many real world objects consist of structures at different scales. Multiresolution analysis allows for more convenient analysis of the signal, although it is important that the multiresolution technique allows for perfect reconstruction of the original signal so that no important information is lost during the process. The two MR fusion approaches considered are the Discrete Wavelet Transform (DWT) and Dual-Tree Complex Wavelet Transform (DT-CWT).

The Discrete Wavelet Transform is a signal analysis which results in a non-redundant image representation. The Discrete Wavelet Transform can be thought of as a bandpass representation which can be constructed from highpass and lowpass filters, where the highpass coefficients represent the details and the lowpass coefficients represent the image at lower resolution levels. The 2-D Discrete Wavelet Transform shown in Figure A5.1 is computed by the recursive application of lowpass and highpass filters in each direction of the input image followed by the downsampling operation, downsampling by a factor of 2.

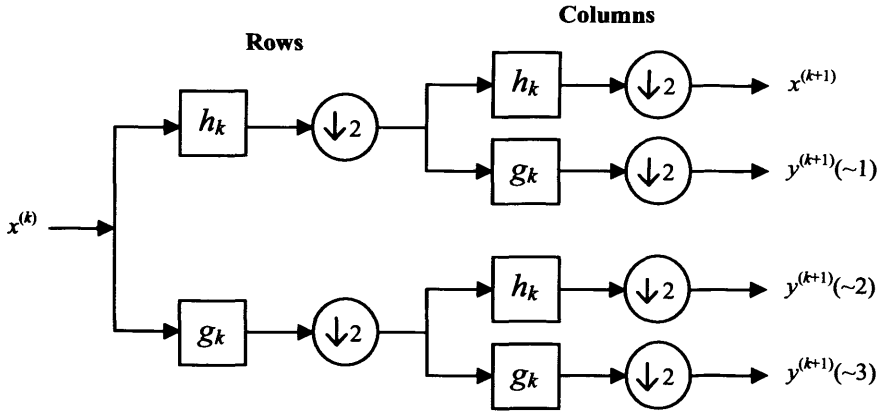

Figure A5.1 The 2D Discrete Wavelet Transform (DWT).

For each level k, the input $x^{(k)}$ is decomposed into a coarse approximation $x^{(k+1)}$ and three signals $y^{(k+1)}=\{y^{(k+1)}(\sim 1), y^{(k+1)}(\sim 2), y^{(k+1)}(\sim 3)\}$, corresponding to the horizontal, vertical and diagonal directions. The lowpass h_k and highpass g_k filters are based on the biorthogonal Daubechies wavelet family (DBSS 2,2) [115]. Reconstruction is achieved through application of the inverse of Figure A5.1, known as the composition tree. One major drawback of the Discrete Wavelet Transform when applied to image fusion is its shift and rotation dependancy, resulting in deterioration of performance if the images are not perfectly registered or when there is slight object movement or rotation. This shift-variance is due to the downsampling operation required for the necessary decimation. A solution to this is to use undecimated filter banks. However, this method leads to a redundant multiresolution representation. A more convenient

alternative from the point of view of both computational complexity and reduced redundancy is the Dual-Tree Complex Wavelet Transform, as shown in Figure A5.2.

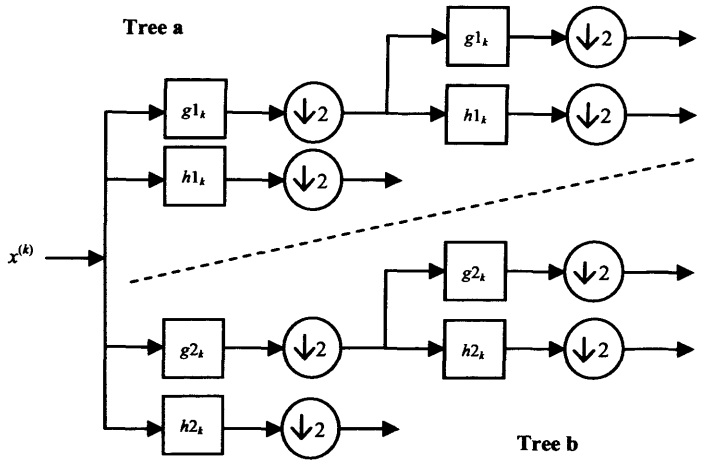

Figure A5.2 The Dual-Tree Complex Wavelet Transform (DT-CWT).

The Dual-Tree Complex Wavelet Transform uses two separate Discrete Wavelet Transform decompositions (Tree *a* and Tree *b*) to calculate the complex transform of a signal. If appropriate filters are selected for each tree it is possible for one Discrete Wavelet Transform to produce the real coefficients and the other the imaginary coefficients. Using two Discrete Wavelet Transforms results in a redundancy of two, but this provides extra information for analysis and the input signal can be reconstructed exactly from either tree. By averaging both of the tree outputs approximate shift-invariance can be obtained. The property of shift-invariance is desirable as it ensures robust subband fusion by permitting effective comparison between the magnitudes of the coefficients. The standard Discrete Wavelet Transform produces three bandpass signals at each level while the 2D Dual-Tree Complex Wavelet Transform produces six bandpass subimages with complex coefficients at each level. These bandpass subimages are strongly oriented at angles of ±15°, ±45°, ±75°. This directional sensitivity results from the complex filters ability to distinguish negative and positive frequencies both horizontally and vertically. A more complete explanation of Discrete Wavelet Transform can be found in [39, 115]. Reference [116] discusses the Dual-Tree Complex Wavelet Transform and the filters which are suitable for use with Dual-Tree Complex Wavelet Transform. The software provided by Professor Kingsbury through the DIF DTC contains a large number of filter types.

But it falls to the user to optimise the choice of filter. For experimental purposes we selected the Antonini 9,7 tap filters and Quarter Sample Shift Orthogonal (Q-Shift) 10,10 tap filters [92], which were determined by the author through simulations to produce the best results for the particular applications.

A5.2 Multiresolution Fusion Techniques and Combination Rules

Coefficients in the detail images having large absolute values are considered to represent the salient features in the image such as lines, edges and region boundaries. Based on this assumption fusion strategies can be applied. However, the coefficients in the approximate image at the lowest level may not represent details as they are coarse approximations of the original image; therefore, a different fusion strategy is required. For fusion of the approximate coefficients averaging can be implemented based on the assumption that the approximate coefficients contain additive Gaussian noise, thus averaging reduces the variance whilst maintaining an appropriate mean value. For fusion of detail coefficients the salient features in the image should be identified and fused.

How important a feature is can be measured by its "salience". High values of salience represent patterns that play a role in representing important information within a scene, while low values are assigned to unimportant or corrupt information. The measure of salience can be governed by the application, i.e. for image analysis applications prominent features are represented by high amplitude coefficients. Saliency can also be regarded as energy; therefore, variance within a neighbourhood can also be used as the criterion for judging saliency. The human visual system is sensitive to local contrast changes, so a sensible fusion rule would be to select the maximum of the absolute values as these should represent the edges and changes in contrast. This approach is known as *choose-max* or the *maximum selection* (MS) rule [94]. However, this method assumes that important features are only contained in one image at each pixel location. It would be more desirable to include information from both sources based on a weighted average according to the importance of each

coefficient within the considered scene. Burt et al. [117] propose such a *weighted average* (WA) scheme also known as the *Match and Selection* rule, which uses an activity measure and the similarity between each coefficient as the criteria for fusion. The selection process ensures that all important information is retained whilst artifacts due to opposite contrast are reduced, whereas averaging the coefficients when the source images contain similar information reduces noise. The match process determines the measure of similarity between corresponding transform coefficients and can be achieved through a correlation measure. The combination rule can be implemented by a weighted average where the weights depend on the match and selection measures. Firstly, if the corresponding transform coefficients are distinctly different then the most salient feature is selected (selection), otherwise, the coefficients should be averaged. The match operation decides whether to use selection or averaging, via a weighted average. The local variance is used for the local activity measure. The match computes the similarity between transform coefficients, which can be defined as the normalised correlation averaged over a neighbourhood of samples.

Spatially close samples are likely to be related to the same feature in the image, and therefore they should be treated in the same manner. A method proposed by Li et al. [118] is a *window based verification* (WBV) scheme also known as *consistency checking*. First a binary decision map is created containing the decision of the selection process based on the local activity indicator. In this case the maximum selection rule is implemented as the measure for local activity indicator. Then the window based verification is performed where the verification process is achieved through a majority filter, with window sizes typically 3×3 or 5×5. Window based verification involves considering a window around the sample in the decision map, and if the central sample in the window is selected from image *a* but the majority of surrounding coefficients are selected from image *b*, then the decision is changed so that the central coefficient is now selected from image *b* to be consistent with its neighbouring samples.

These fusion rules can be directly applied to the Discrete Wavelet Transform coefficients. For the Dual-Tree Complex Wavelet Transform fusion when using the maximum selection rule a combined coefficient map (containing the indexes of the selected coefficients) should be created which is then used to select the appropriate coefficients, followed by application of the inverse Dual-Tree Complex Wavelet Transform to produce the fused image. The weighted average and window based verification rules should be applied directly to the magnitude of the complex values also creating a combined coefficient map which should then be used to select the appropriate coefficients, followed by the inverse Dual-Tree Complex Wavelet Transform to produce the fused image.

A5.3 Quantitative Analysis Measures for Assessment of Impairment Mitigation and Fusion Algorithms

The performance of impairment mitigation and fusion algorithms can be estimated by comparing the ground truth data with the results of image fusion for the mitigated images. Image quality assessment is a very difficult task and it is not currently possible for any single measure to definitely determine the best quality image. Instead, several measures are required each of which is applicable for estimating quality with respect to specific features or characteristics of the image. Estimation of fused images pose an additional problem, where the difficulty lies in the fact that generally ideally fused images are not available for use as ground truth data, except for cases where contrived experimental data are used. Additionally, the ideally fused image is often dependent on the application that will use the data, for example, the data most suitable for object detection may not necessarily be appropriate for estimation of soil moisture content of a region. Therefore, several measures have been proposed which attempt to identify important information in the source images and determine how much of this is transferred into the fused image.

With this in mind it is the author's point of view that the only way to absolutely determine image quality whether fused or not fused, is by applying the data to a

specific task, therefore, giving an indication of best image quality with respect to that task. It is acknowledged that this approach is task specific and for cases where this is not possible general quality estimates are an acceptable alternative, providing appropriate attention is given to the specifics of the quality estimate and the limitations of the estimate are understood.

Quality estimates for evaluating the effectiveness of impairment mitigation techniques are discussed in Section A5.3.1. Methods for quantitative analysis of fusion techniques in transferring only relevant information to the fused image are discussed in Section A5.3.2.

A5.3.1 Quality Measures for Assessment of Data Transmission Errors Impairment Mitigation

The improvement in image quality can be evaluated using the signal-to-noise ratio (SNR) and the mean squared error (MSE) to assess the effectiveness of mitigation of impairments. SNR can be defined as

$$SNR = 10\log_{10}(\sum_{r,c} I(r,c)^2 / \sum_{r,c}[I(r,c) - \hat{I}(r,c)]^2) \qquad \text{(A5.1)}$$

where $I(r,c)$ are the original image samples when impairments are absent, $\hat{I}(r,c)$ is the image at the output of the mitigation algorithm, and (r,c) are the row and column coordinates, respectively.

The MSE is the mean of the square of error, defined as

$$MSE = \frac{1}{N}\sum_{r,c}(I(r,c) - \hat{I}(r,c))^2 \qquad \text{(A5.2)}$$

Here N is the number of image samples, $I(r,c)$ are the original image samples when impulse noise is absent and $\hat{I}(r,c)$ is the image at the output of the mitigation algorithm.

A5.3.2 Quality Measures for Estimating Image Fusion Performance

For assessing the quality of fused images three evaluation criteria are selected: mutual information (*MI*) [102] between the two source images and the fused image, and the qualitative measures Q_{abf} and Q_w [103]. MI for the fused image can be obtained by taking the sum of the *MI* between the composite and each source image, then to normalise the measure in the range [0, 1] this is divided by the sum of the entropy of each source image. This can be defined as

$$MI(a,b,f) = \frac{MI(a,f) + MI(b,f)}{H(a) + H(b)} \qquad \text{(A5.3)}$$

where $MI(a,f)$ is the MI between source image a and fused image f, and $H(a)$ is the entropy of source image a; and similarly for $MI(b,f)$ and $H(b)$. However, this measure does not take into account whether the important details in the source images are contained in the fused image. Wang and Bovik propose an image quality index Q_o [119] to quantify the structural distortions between two images which can be defined as

$$Q_0 = \frac{4\sigma_{ab}^2 \bar{a}\bar{b}}{(\bar{a}^2 + \bar{b}^2)(\sigma_a^2 + \sigma_b^2)} \qquad \text{(A5.4)}$$

where $\bar{a}$ denotes the mean of a, $\bar{b}$ denotes the mean of b, σ_a^2 the variance of a, σ_b^2 the variance of b, and σ_{ab}^2 the covariance of a and b. Q_o is a measure of similarity

between image a and image b producing values between -1 and 1, with the maximum of 1 given when the two images are identical. To account for the non-stationary characteristic of the image signal, local regions should be independently analysed using Q_o and then combined to produce a single measure. Wang and Bovik therefore propose a sliding window approach

$$Q_0(a,b) = \frac{1}{|W|}\sum_{w\in W} Q_0(a,b \mid w) \qquad \text{(A5.5)}$$

where W is the set of all windows and $|W|$ is the cardinality of W. For each window w the local quality index $Q_0(a,b|w)$ is computed for all pixels within window w. To produce the quality estimate for the whole image all local quality indexes are averaged. In [103] Piella proposes the quality measure Q_{abf} for image fusion to show the quality of the composite image given the input images a and b. This measure can be defined as

$$Q_{abf} = \frac{1}{|W|}\sum_{w\in W}\left(\lambda_a(w)Q_0(a,f \mid w) + \lambda_b(w)Q_0(b,f \mid w)\right) \qquad \text{(A5.6)}$$

where $Q(a,f \mid w)$ is the local quality measure between image a and the fused image f within window w a; and similarly for $Q(b,f \mid w)$. $\lambda_a(w)$ and $\lambda_b(w)$ are the local weights calculated on the local saliency within window w of image a and b respectively. These weights can be defined as

$$\lambda_a(w) = \frac{s(a \mid w)}{s(a \mid w) + s(b \mid w)} \qquad \text{(A5.7)}$$

where $s(a|w)$ is the local saliency of image a in window w, and $s(b|w)$ is the local saliency of image b in window w . Saliency can be selected to be based on contrast,

variance or entropy. The higher the value of $\lambda_a(w)$ the more important image a is with respect to image b. For this case λ_b can be calculated as $\lambda_b(w) = 1-\lambda_a(w)$. For simulation purposes the local variance is selected as the criterion for $s(a|w)$.

The measure Q_{abf} weights all windows equally, which may not be appropriate because some features may be more important than others. Piella proposes a weighted quality measure Q_w [103], based on the assumption that some areas of the image are more important than others due to the human visual system placing more importance on salient regions within an image. Therefore, Q_w allocates higher weights to windows which have a higher saliency, as these areas should correspond to perceptually important regions within the image. Q_w is defined as

$$Q_w = \frac{1}{|W|}\sum_{w\in W} c(w)\left(\lambda_a(w)Q_0(a,f \mid w) + \lambda_b(w)Q_0(b,f \mid w)\right) \qquad \text{(A5.8)}$$

where $c(w) = C(w)/(\sum_{w'\in W} C(w'))$ and $C(w) = \max(s(a \mid w), s(b \mid w))$ denotes the overall saliency within a window w.